Development of the Micro Pixel Chamber with resistive electrodes

Fumiya Yamane
Kobe University Department of Physics

January 12$^{\mathrm{th}}$, 2018

Abstract

The Micro Pixel Chamber (μ-PIC) with resistive electrodes has been developed as the charged particles tracking detector for future high-rate applications such as the HL-LHC. It is a two-dimensional gaseous imaging detector made by PCB technique. Cathode electrodes are made of resistive material in order to suppress the sparks current. However, there remained problems in the detector design and the resistive material. In order to overcome those problems, a novel design of the resistive μ-PIC has been proposed. The resistive material was replaced to DLC (Diamond Like Carbon) thin film. The resistivity can be controlled flexibly at high uniformity in a large detection area. The fabrication-process was greatly improved and the μ-PIC can be operated at $10\times10\text{cm}^2$. Resistors for HV bias and capacitors for AC coupling were completely removed by applying PCB and carbon sputtering techniques, then the μ-PIC became a very compact detector. The gas gain of more than 10^4 was achieved. The uniformity of the gas gains was within 30% in whole detection area. The high-rate capability was more than 10^7cps/cm^2. Two-dimensional X-ray images were taken, and fine structures of $\sim$1mm could be seen visually. Performances for charged particles have been measured using 150GeV/c muons beam at SPS/H4 test beam in CERN. The detection efficiencies were more than 98%. The time resolution was 13-16ns. The position resolution was 60-90μm. The fast neutrons irradiation test has been performed at the tandem electrostatic accelerator facility in Kobe University Faculty of Maritime Science. The spark rate was 10^{2-5} times lower than that of the non-resistive μ-PIC. The μ-PIC could be operated at the gas gain of 5000 under the fast neutrons flux up to $1-4\text{MHz/cm}^2$ without no gain drop, in which the cathode resistivity was $\sim$180kΩ/sq.

Contents

Chapter 1

Introduction

In high energy physics experiments, high statistics are needed for precise measurements, and the particle rate has been increased in recent years. Therefore detectors are requested to withstand the high-rate radiation environment. For example, the luminosity of the LHC will be increased from $2\times10^{34}\mathrm{cm}^{-2}\mathrm{s}^{-1}$ to 5-7$\times10^{34}\mathrm{cm}^{-2}\mathrm{s}^{-1}$ in 2025 [1]. Conventionally, wire chambers, such as MWPC and drift chambers, have been used for the particle tracking with a large area coverage. However, they cannot withstand the high counting rate ($> 10^7$cps/cm^2) in the High-Luminosity LHC (HL-LHC). Therefore they will be replaced by the new type of detectors so called Micro Pattern Gaseous Detectors (MPGDs) [2], in which micro-electrodes are used instead of wires, and a high-rate capability of more than 10^8cps/cm^2 can be achieved. Also, a large detection area can be realized with a reasonable cost. The Micromegas [3] will be used for the endcap muon spectrometer of ATLAS [4], and the GEM [5, 6] will be used for that of CMS [7]. Also, there are plans to extend the acceptance for muons to higher $\mid \eta \mid$ regions up to 4.0 (η: pseudo rapidity) in both experiments. Here, high-rate capability up to 10MHz/cm^2 and high granularity of a few mm^2 are required, and MPGDs are suggested for those detectors. Thus, MPGDs are expected to play a important roll in future high-rate experiments.

The problem with MPGDs is sparks between electrodes. In gaseous detectors, sparks are caused when the avalanche size exceeds $\sim 10^8$ electrons, which is called as the Raether limit [8]. In the case of MPGDs, since electrodes are placed at vary short distance of several tens of micron, the space charge density increases. Then, the Raether limit is reduced to $\sim 10^{6-7}$ [9]. The ATLAS Micromegas and CMS GEM will be operated in the background of fast neutrons which yield heavily ionizing particles in the detector. In this radiation environment, frequent sparks are unavoidable. Fine electrodes are easily damaged by sparks and electrical breakdown is caused between electrodes. As for the GEM, the spark rate can be reduced by using multiple amplification stages. On the other hand, structures for spark-protection are needed for single amplification stage detectors such as the Micromegas. In order to overcome this problem, resistive electrodes have been introduced since 2010 [10]. The sparks current is reduced by resistive electrodes and it was found that the Micromegas with resistive strips could be operated stably under the fast neutrons irradiation [11]. Over the past few years, developments of MPGDs with resistive electrodes have been performed for high-rate applications. As one of them, the Micro Pixel Chamber (μ-PIC) with resistive electrodes have been developed in Kobe university.

The μ-PIC has been developed and used for various applications mainly in Japan [12, 13]. It is a two-dimensional imaging detector fabricated by the PCB (Print Circuit Board) technique. Anode and cathode strips are perpendicularly placed with a pitch of 400μm, which allows a precise position measurement with a good spatial resolution of 100μm at two-dimension. One of the advantage of the μ-PIC is that it does not need any floating structures, such as foils and meshes, for operation. That simplifies the assembly procedure of the large size detector. For the spark protection, the μ-PIC in which cathodes are made of resistive material has been developed since 2011 [14]. In the previous study of the resistive μ-PIC, it was found that sparks were strongly suppressed by the resistive cathode [14]. However, there remained problems in the electrode structure. By adding the resistive layer, the electrode structure and fabrication processes became complicated, and it was difficult to make electrodes with accurate alignment at whole detection area of 10×10 cm^2. Also, the resistive material was not suited for practical use in high-rate applications because the resistivity cannot be well controlled. In high-rate radiation environments, gas multiplications are occurred continuously, and a current always flows on electrodes. If the resistivity is too high for the particles rate, the gas gain drops greatly, then the detection efficiency is dropped. This effect should be considered when there are heavily ionizing particles. The resistivity should be adjusted to the appropriate value and appeared at high uniformity in whole detection area. In order to realize those requirements, a new resistive material was needed.

In this thesis, a new design has been proposed to overcome those problems. The DLC (Diamond Like Carbon) thin film made by carbon sputtering technique [15] was adopted for resistive electrodes. DLC is a novel resistive material developed in Kobe university, which realizes flexible control of the resistivity from 50kΩ/sq. to 3GΩ/sq. and high uniformity at a large detection area. The electrodes alignment was solved by using photolithography instead of laser drilling, then the resistive μ-PIC can be operated at whole detection area of 10×10 cm^2. Moreover, by applying PCB and carbon sputtering techniques, resistors for HV bias and capacitors for AC coupling have been no longer needed for the signals readout. This novel idea made the μ-PIC very compact.

The performances of the new resistive μ-PIC have been measured by various ways. First, the gas gain and high-rate capability were measured, and two-dimensional images were taken using X-rays. Next, the detection efficiency, time resolution and position resolution for charged particles were measured at SPS/H4 test beam at CERN. The spark rate and high-rate capability for heavily ionizing particles were measured at the tandem electrostatic accelerator facility in Kobe University Faculty of Maritime Science.

In this thesis, developments of the novel resistive μ-PIC and results of performance studies are described. In Chapter 2, several MPGDs and their features are introduced. Also, the development of MPGDs with resistive electrodes for overcoming sparks are presented. In Chapter 3, first, the basic property of the μ-PIC is presented. Next, the development of the μ-PIC with resistive electrodes and its previous studies are described. After chapter 4, novel resistive μ-PIC and its first results are described. In Chapter 4, the novel design of the new resistive μ-PIC and its basic performances are described. In Chapter 5, the performance studies using charged particles are described. In Chapter 6, performances under the fast neutrons irradiation are described. In chapter 7, the summary and conclusion of this thesis are described.

Chapter 2

Micro Pattern Gaseous Detectors

2.1 Operation principle of gas detectors

The proportional counter is one of the most basic gaseous detectors.. Figure 2.1 shows the schematic view of the proportional counter. It consists of an anode wire and a cathode tube, and it is filled with a gas. When a charged particle passes through the gas volume, gas atoms are ionized and electron-ion pairs are created along the track of the incident particle. These electrons are called primary electrons. By applying high potential between the anode wire and the cathode tube, primary electrons drift towards the anode wire, and ions drift towards the cathode tube. The electric field *E(r)* at the distance r from the center of the anode wire is equal to

$$E(r) = \frac{1}{r}\frac{V}{\ln\frac{b}{a}} \tag{2.1}$$

where, V is the potential difference between the anode wire and the cathode tube, a and b are the radius of the anode wire and the cathode tube, respectively. The strength of the electric field is proportional to r^{-1}, therefore it increases rapidly near the anode wire. Primary electrons are rapidly accelerated near the anode wire. When their kinetic energy exceeds the ionization energy of gas atoms, secondary ionizations are occurred. Those processes are continued in a chain reaction, and it turns into the avalanche multiplication. Thus, particles are detected by reading the multiplied electrons charge. Details of these physics processes are described in the Appendix.

2.2 Multi Wire Proportional Chamber

One of the most important invention for the particle physics is the Multi Wire Proportional Chamber (MWPC) developed by G. Charpak in 1968 [16]. By the invention of the MWPC, particle tracks can be obtained electrically in real-time. Figure 2.2 shows the schematic view of the MWPC. It consists of anode wires and cathode planes in the gas volume. Gas molecules are ionized by incident particles, and pairs of an electron and a positive ion are generated. Due to the electric field in the gas volume, electrons and ions move toward the anode wires and the cathode planes, respectively. When electrons approach near the anode wires, the number of

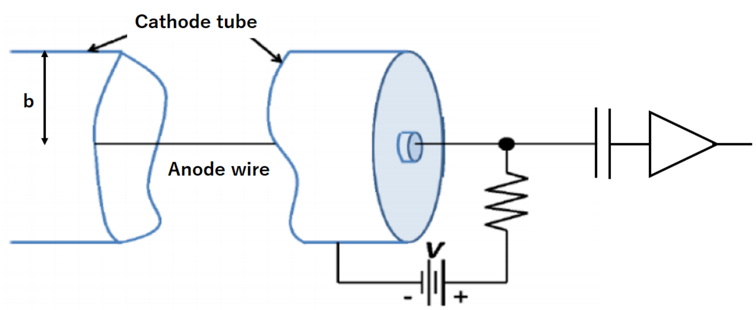

Figure 2.1: Schematic view of the proportional counter.

electrons is multiplied by the avalanche process. In this process, the achievable gas gain is $\sim 10^5$. From the position of obtained signals, the fine track of particles can be estimated.

However, there is inevitable limitations for the MWPC. First, the electrode pitch cannot be narrowed below 1mm due to the electric repulsive force between wires. The spatial resolution of the detector is limited by them. Second, the rate capability is limited below 10^4Hz/mm^2 due to the space charge of positive ions between anode wires and cathode planes.

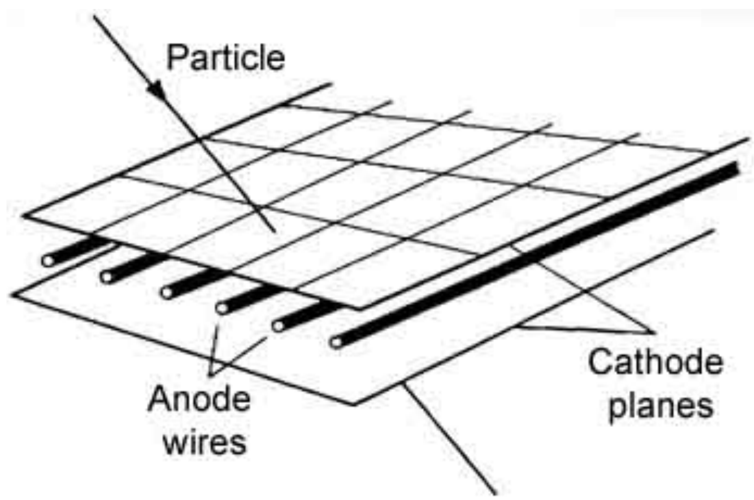

Figure 2.2: Schematic view of the MWPC [17].

2.3 Micro Pattern Gaseous Detector

Micro Pattern Gaseous Detectors (MPGDs) have been developed since the end of the last century in order to overcome the limitations of conventional wire chambers [2]. They are manufactured by micro processing and photolithography technique, in which wires are replaced for printed micro electrodes. This novel scheme realizes a good spatial resolution better than 100μm, high-rate capability ($> 10^6$Hz/mm^2), radiation hardness and large area coverage with reasonable cost. MPGDs offer the solution of the requirement of a large area coverage with fine spatial resolution for the recent high-energy particle physics. In this section, we introduce several MPGDs: the MSGC which was invented as first, and the GEM, Micromegas those are widely used in various applications.

2.3.1 Micro Strip Gas Chamber

The Micro Strip Gas Chamber (MSGC) is the first invention of the MPGD developed by A. Oed in 1988 [18]. Figure 2.3 shows the schematic view of the MSGC with two-dimensional readouts [19]. It consists of the anode and cathode strips alternately placed on the insulating substrate. Anode strips are formed to have a pitch of 200 μm, and cathode strips are placed between anodes. By replacing wires with micro electrodes, a good spatial resolution of 30$\sim$100μm and a rate capability of more than 10^6Hz/mm^2 can be achieved. Also, the manufacturing process is much simpler compared to wire chambers.

The MSGC was expected to replace conventional wire chambers, but it has several problems. One is the accumulation of positive ions on the insulating substrate, those are generated by the avalanche process. This effect leads to variations of the gas gain. Another is discharges between electrodes, which causes dead time of the chamber and destructive damages on the electrodes. The detail of the discharges in MPGDs is discussed in section 2.4. Despite many efforts by researchers, these problems can not be resolved, so other approaches have been tried [20].

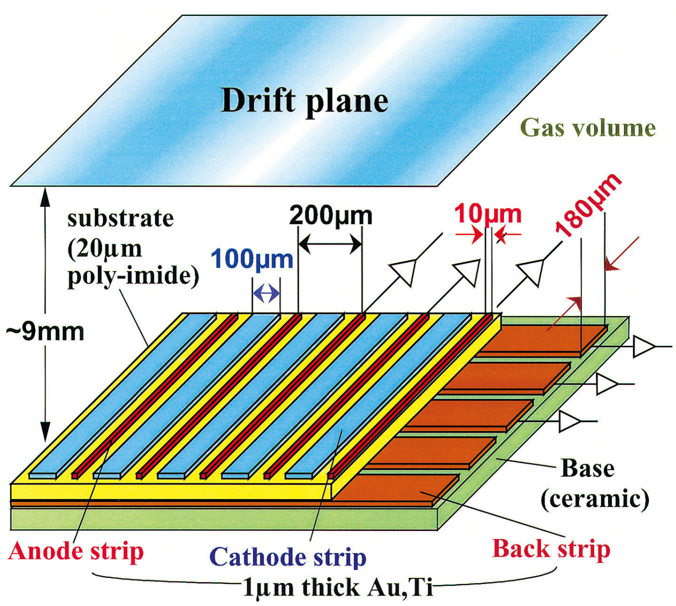

Figure 2.3: Schematic view of the MSGC with two-dimensional readouts [19].

2.3.2 Gas Electron Multiplier

The Gas Electron Multiplier (GEM) has been developed by F. Sauli in 1997 [5, 6]. It consists of highly dense holes made in the thin foil with double-sided electrodes.

Figure 2.4 (left) shows the electron microscopic image of the GEM. In this picture, the thickness of the GEM foil is 50μm, and the diameter and the pitch of holes are 70μm and 140μm, respectively. Applying high tension voltage (300-600V) between the top and the bottom electrode, a high electric field is appeared in holes (see Figure 2.4 (right)). Hence, the avalanche process is occurred inside each hole. Signals are induced on the readout electrode by the collection of electron amplification (see Figure 2.5 (left)). One of the unique features of the GEM is that several GEM foils can be placed with a short distance of 1-2mm to separate the avalanche process into several stages. Figure 2.4 (right) shows the schematic structure of the Triple-GEM. The advantage of this scheme is that the electric field of each GEM foils can be reduced compared to the single stage GEM, so it is possible to avoid the critical discharges. In the high-rate applications, the GEM has been already used such as for example the COMPASS tracker [21], CMS forward muon spectrometer and the ALICE inner tracker toward the luminosity upgrade of the LHC [7].

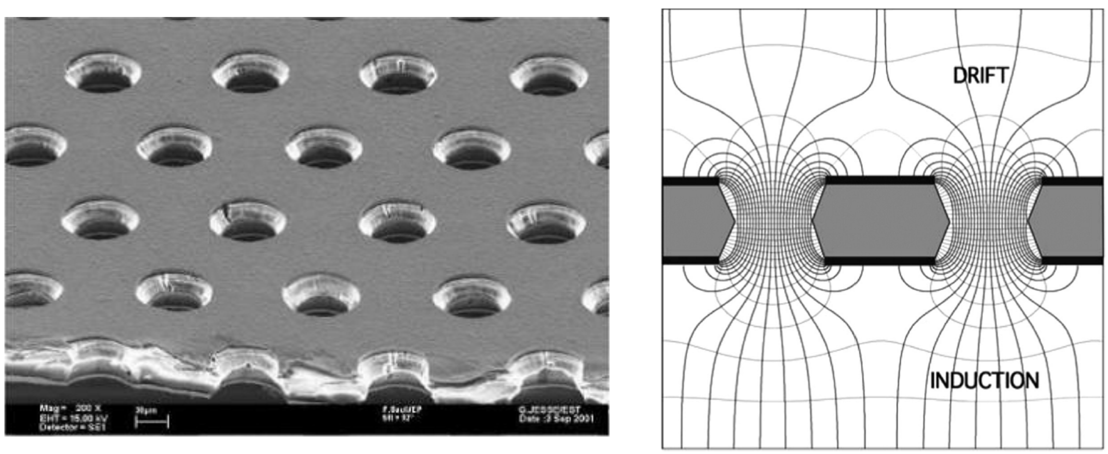

Figure 2.4: Left: electron microscopic image of the GEM. Right: electric field generated in the GEM holes. [6].

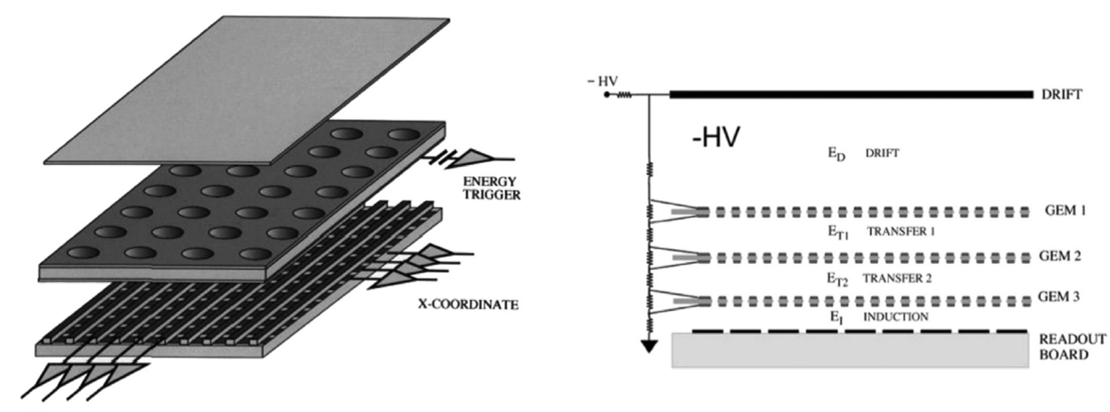

Figure 2.5: Left: schematic view of the GEM with the two-dimensional strip readout. Right: schematic view of the Triple-GEM detector. [6]

2.3.3 Micromegas

The Micro Mesh Gaseous Structure (Micromegas) has been developed by Y. Giomataris in1996 [3]. Figure 2.6 shows the schematic view of the Micromegas. The Micromegas is a parallel-plate avalanche chamber composed of a few mm drift/conversion gap and a thin amplification gap of 50-100μm. The amplification gap consists of a micro-mesh plane and the readout electrode printed on the insulating substrate. The micro-mesh is supported by insulating pillars. The electric field of the drift region is set to low ($\sim$1kV/cm) and that of the amplification region is set to high (50$\sim$100kV/cm). This makes micro-mesh transparent for electrons. The great advantage of the Micromegas is the fast evacuation of the space charge of positive ions (100ns). Hence, a high gas gain ($> 10^4$) and a high-rate capability $> 10^6$Hz/mm^2 can be realized. The Micromegas is used in various applications. As same as the GEM, the Micromegas has been already used for the COMPASS tracker [22]. Also, it is adopted to be used for the ATLAS forward muon spectrometer toward the luminosity upgrade of the LHC [4].

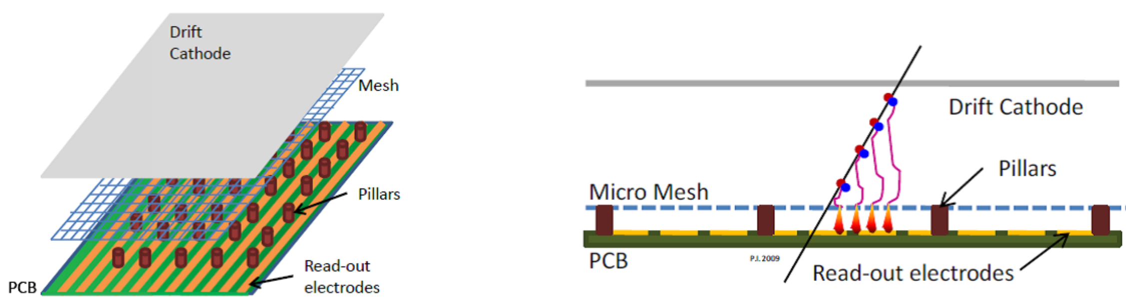

Figure 2.6: Schematic view of the Micromegas [3].

2.4 Gain limitation for MPGDs

The maximum achievable gain of MPGDs is limited by the so called Raether limit [8]. It is the number of electrons generated by the avalanche process, in which the avalanche turns into sparks. The Raether limit is around 10^8 for wire chambers. In the case of MPGDs, electrodes are placed with a short distance of several tens or hundreds of μm, a space charge density becomes higher than that of wire chambers. Therefore, the Raether limit drops to 10^{6-7} [9]. Electrodes of MPGDs are easily damaged by sparks. For example, Figure 2.7 shows a photo of the MSGC, in which electrodes are destructed by sparks between anode and cathode strips [10]. The substrate (black pattern) is carbonized, and breakdowns are caused between anodes and cathodes. Therefore, it is important to know the maximum achievable gain in order to avoid sparks. For example, the maximum gain is $\sim 10^4$ for 5.9keV X-rays from ^{55}Fe source, because the number of primary electrons is $\sim$220 with the Ar based gas in the standard atmospheric pressure. On the other hand, the gas gain for alpha particles is order of 10^2 due to $\sim 10^5$ primary electrons.

However, there are cases in which frequent sparks are unavoidable, such as detecting minimum ionizing particles in the background of heavily ionizing particles. For example, as mentioned in the former section, MPGDs will be used for the forward muon spectrometer in ATLAS and CMS. In that region, there are the background of fast neutrons. They interacts with atomic nuclei of detector materials and gas molecules by the elastic scattering, and those recoiled nuclei are heavily ionizing particles. In order to detect muons, the gas gain of several thousands is needed. However it exceeds the Raether limit for recoiled nuclei.

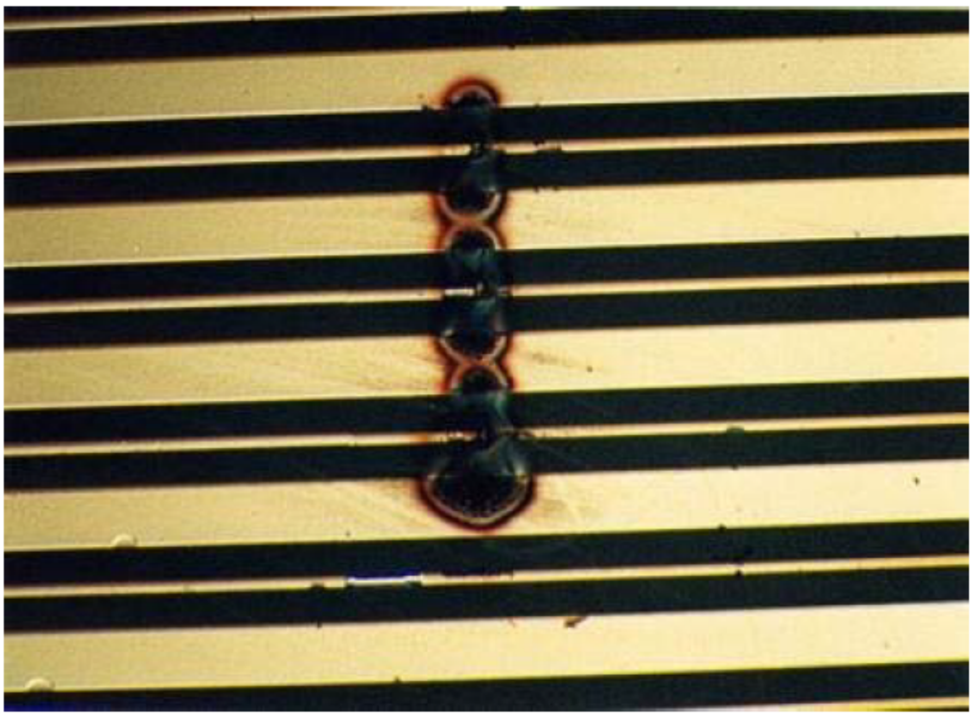

Figure 2.7: Photograph of the MSGC damaged by sparks [10]. Thick gold strips are cathodes and thin gold strips are anodes. The black pattern is the substrate. Sparks are occurred between anode and cathode strips.

2.5 Development of the resistive electrodes

Since 2010, MPGDs with resistive electrodes have been developed [10]. The Raether limit is unavoidable process, but detectors are protected from sparks by suppressing the spark current. This novel structure has been adopted for the ATLAS Micromegas. Figure 2.8 shows the schematic view of the Micromegas with resistive strips. An insulating layer is sandwiched by resistive strips and readout strips. Signals are induced on readout strips. When a spark is occurred in the amplification region, a large current is flowed. The large current cause voltage drop on resistive electrodes. Then the electric field is weakened, and the spark growth stops. Figure 2.9 shows the voltage and current measured under fast neutrons irradiation for the Micromegas without resistive electrodes (left) and the resistive Micromegas (right) investigated by the Greece group [11]. The continuous line is the voltage, and square marks are currents. Large spark currents and frequent voltage breakdowns were seen for the non-resistive Micromegas, whereas no voltage breakdowns were observed for the resistive Micromegas even for gas gains of over 10^4. Thus, sparks are successfully reduced by using resistive electrodes on the detector. This structure can be extended to various types of MPGDs like the GEM, MSGC and so on. Therefore, MPGDs with resistive electrodes are expected to play an important roll in the future high energy physics experiments. In the past few years, various MPGDs with resistive electrodes have been developed and tested [23, 24].

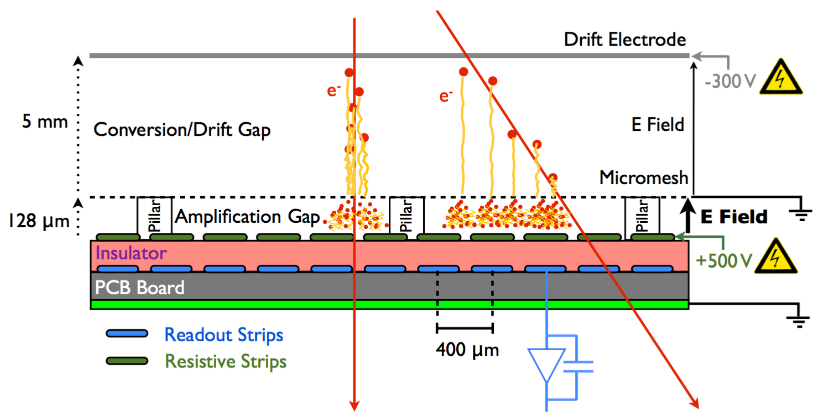

Figure 2.8: Schematic view of the Micromegas with resistive strips [11].

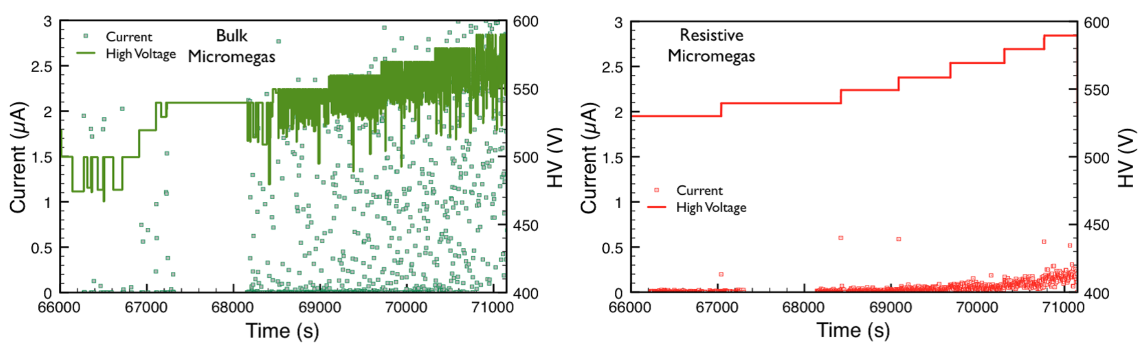

Figure 2.9: Voltage and Current monitor under fast neutrons irradiation for the Micromegas without resistive electrodes (left) and the resistive Micromegas (right). The continuous line is the voltage, and markers are currents. [11]

2.6 Diamond Like Carbon; a novel material for resistive electrodes

Conventionally, carbon-loaded pastes have been used for the resistive electrodes. The resistivity is appeared by connections between particles of carbon black in the paste, and determined by the density and various parameters of carbon particles. Therefore, the resistivity is affected by the conditions of carbon particles and situations of the production. Hence, it is difficult to realize the precise control and high uniformity of the resistivity. However, there were no other materials which have proper resistivity around 1MΩ/sq., which is the ideal resistivity for spark suppression.

In 2012 at Kobe university, a novel resistive material using carbon sputtering technique has been developed for MPGD electrodes [15]. Figure 2.10 (left) shows the schematic view of the carbon sputtering process. A thin ($\sim$100nm) and uniform film is formed on the substrate using a graphite sputtering target. This film consists of amorphous carbon of sp^2 and sp^3 hybrid, and it is called Diamond Like Carbon (DLC). The resistivity of order of 1MΩ/sq. can be realized. Production is performed at Be-Sputter Co., Ltd. using a large sputtering chamber, in which a substrate with 4.5m $\times$ 1m is available at maximum (see Figure 2.10 (right)). The DLC film adheres to the polyimide substrate firmly and possesses great tolerance to chemicals. Combined with photolithography, fine electrodes can be formed with a precision of better than 10μm using the liftoff method. Figure 2.11 shows the large size foil of 85cm $\times$ 45cm with 415μm pitch strips. Fine strips (c) are precisely formed in the entire area (a). The uniformity of the resistivity was estimated to be below 30%. This foil was made for the prototype of the ATLAS Micromegas, and the large chamber was assembled using this foil. This prototype has been operated well and shown the expected performance [25]. The resistivity is easily and widely controlled by varying thickness and doping nitrogen into the DLC film. Figure 2.12 shows the surface resistivity as a function of the thickness of the DLC film. The red line is of pure DLC, and the blue one is of nitrogen doped DLC. The resistivity can be controlled from 50kΩ/sq. to 3GΩ/sq.

A resistive Micromegas with an active area of 10cm $\times$ 10cm, in which resistive strips were made of the DLC film, has been produced and tested. The resistivity was set to 1MΩ/sq. The gas gain was more than 10000, and no damage were observed after the operation under fast neutrons irradiation. As well as the Micromegas, the DLC electrode was applied for the GEM [26], MSGC and they were well operated.

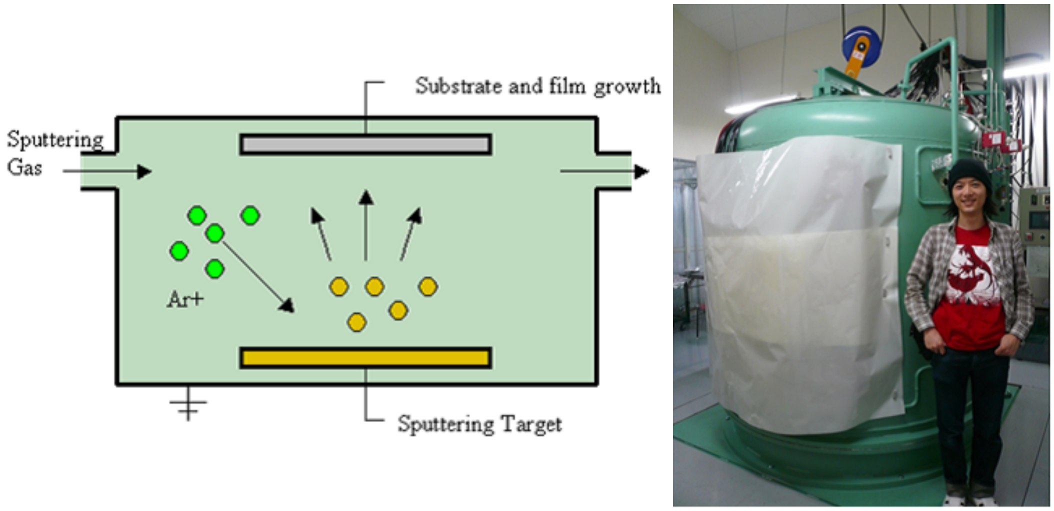

Figure 2.10: Left: Schematic view of the sputtering process. Right: Large industrial spattering chamber in Be-Sputter Co., Ltd.

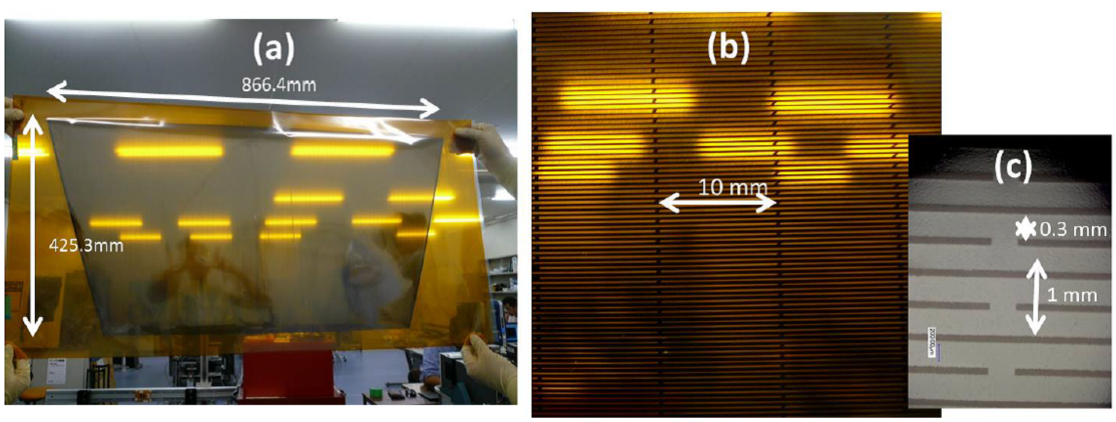

Figure 2.11: (a)Photograph of a few m^2 size foil in which resistive strips are patterned with a pitch of 400μm by carbon sputtering. (b) Zoomed at 10mm scale. (c) Microscopic view. [15]

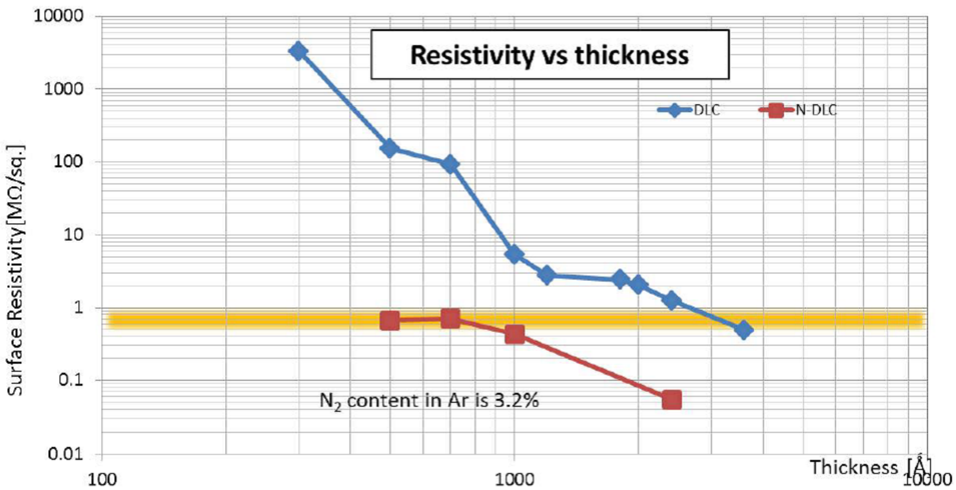

Figure 2.12: Surface resistivity as a function of the thickness of the DLC film [15]. The red line is of pure DLC, and the blue one is of nitrogen doped DLC.

Chapter 3

μ-PIC and that with resistive electrodes

3.1 Electrode structure and the operation principle

The Micro Pixel Chamber (μ-PIC) has been developed by A. Ochi and T. Tanimori in 2001 [12, 13] in order to overcome the limitation of the MSGC. Figure 3.1 shows a schematic view of the μ-PIC. The structure of the μ-PIC is constructed based on double-sided PCB (Printed Circuit Board) manufacture with the 100μm thick polyimide substrate. Cathode strips on the surface of the substrate are formed with a pitch of 400μm. Circles with 250 μm diameter are arranged in the cathode strips with a pitch of 400μm. A small hole of 50μm diameter is drilled at the center of each circle and filled with metal for the anode electrode. Anodes are connected to readout strips on backside of the substrate via the holes. These readout strips are formed with a pitch of 400μm perpendicular to the cathode strips. Thus, fine pixels composed of the anode and the surrounding cathode are arranged on the detector. The gas multiplication is occurred in each pixel. Two-dimensional signals are easily obtained from anodes and cathodes. Assuming digital readouts with 400μm pitch, the position resolution is estimated 115μm RMS for both coordinates.

The electric field near the anode is almost proportional to r^{-2}, while that near the cathode is proportional to r^{-1}. Here, r is the distance from the center of the anode electrode. It means that the electric field near the cathode is quite lower than that near the anodes. Therefore, the electron emission from the cathode can be suppressed and the probability of discharges are reduced compared to the MSGC. The gas gain of 10^4 can be achieved (see Figure 3.2 (left)) and a long term operation with a gas gain of more than 5000 is possible. Those are quite difficult to attain using the MSGC. Also, the μ-PIC can be operated up to 10^7cps/mm^2 without the degradation of the gain (see Figure 3.2 (right)).

One of the most outstanding feature of the μ-PIC is that it has no floating structure; all electrodes are formed rigidly on the substrate. In the case the wire chambers, many wires have to be stretched in the gas volume. When the large area coverage (1m^2) is required, the stretching process of the floating structures makes the construction and assembly procedures complicated. On the other hand, the

μ-PIC can be manufactured by only the PCB technique. It can be operated by just putting the drift plane above the μ-PIC readout board. Also, it can be extended to the large area by arranging multiple μ-PIC substrates with very small dead area.

The μ-PIC has been used for various applications such as the Electron-Tracking Compton Camera (ETCC) [29], directional dark matter search (NEWAGE experiment) [30], neutron imaging [31], space dosimeter (PS-TEPC) [32], and so on. These activities have many important contributions in developments of the μ-PIC.

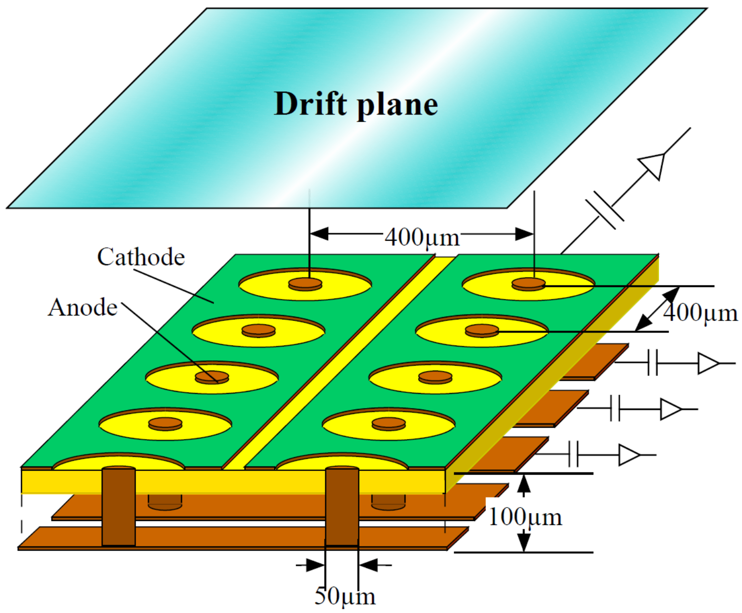

Figure 3.1: Schematic view of the μ-PIC [12].

3.2 Development of the μ-PIC with resistive electrodes

In Kobe university, the μ-PIC has been developed for the charged particles tracking detector in high-rate radiation environment such as HL-LHC. There is a harsh radiation background of heavily ionizing particles more than 10kHz/cm^2. Therefore, the μ-PIC should withstand sparks, and several studies for overcoming sparks have been performed [33].

The most effective solution is usage of resistive electrodes on the μ-PIC [14]. Figure 3.3 shows the schematic view of the resistive μ-PIC. Cathode strips are made of carbon-loaded polyimide paste with resistivity of $10^{5-7}\Omega$/sq. Resistive cathodes and pickup electrodes are separated by an insulating layer. For the cathode readout, induced signals on the pickup electrodes are used instead of resistive cathode electrodes. Figure 3.4 shows the plots of gas gains as a function of the amplification voltage. The gas gain more than 6×10^5 was achieved using Ar/C$_2$H$_6$ (7:3) gas mixture. The operations under the fast neutrons irradiation was also tested. In this test, the drift field was set to 3.3kV/cm with a drift gap of 3mm, and Ar/C$_2$H$_6$

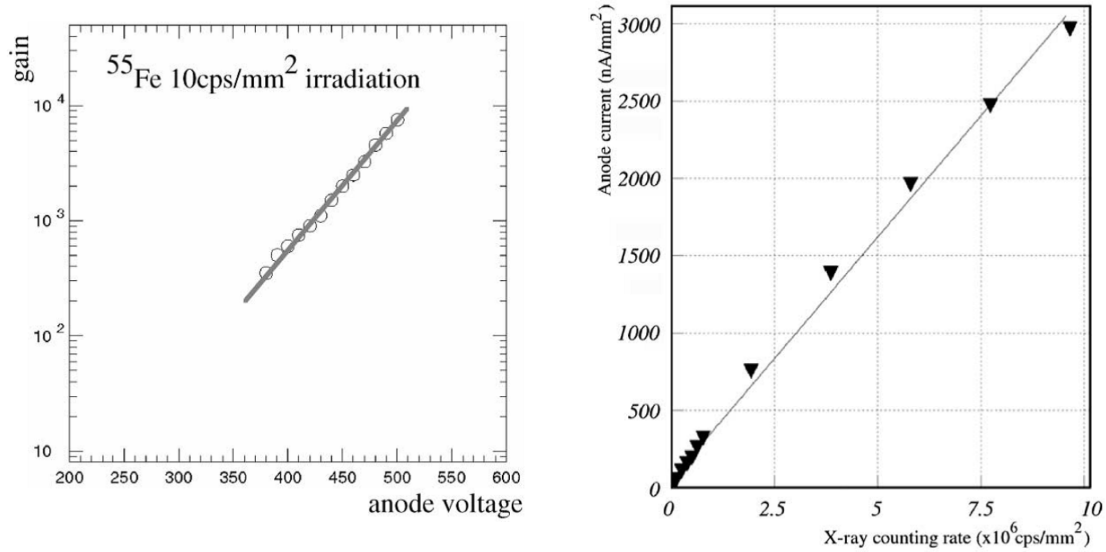

Figure 3.2: Left: Gain variation of the μ-PIC as a function of the anode voltage [12]. Right: Anode current as a function of the intensity of X-rays [13]. Linearity is seen up to the highest counting rate.

(7:3) gas mixture was used. Figure 3.5 shows the monitored anode current for the conventional μ-PIC (left) and the resistive μ-PIC (right) with the same gas gain of $\sim$15000. While large sparks are found with the conventional μ-PIC frequently, all sparks are suppressed below 1μA with the resistive μ-PIC. Figure 3.6 shows the plots of the spark rate. The spark rate of the resistive μ-PIC was 10^{3-5} times lower than that of the conventional μ-PIC. Figure 3.7 shows plots of the spark rate using different threshold for the spark current. The thresholds were set to 0.5μA and 1μA. As for the resistive μ-PICs, the spark rate with a threshold of 0.5μA was about ten times higher than that of 2μA. On the other hand, there were no difference between two thresholds for the conventional μ-PIC. This result means that most large sparks were strongly suppressed by resistive cathodes.

Also, another advantage of this detector design is that resistors and capacitors for the cathode readout are no more needed regardless of the applied cathode voltage. Moreover, because the anode voltage can be set to 0V by applying a negative voltage to the cathode, resistors and capacitors can be removed also for the anode readout. This feature is favorable for the multichannel readout detectors, and the resistive μ-PIC becomes a very compact detector. However, there remains problems. Figure 3.8 (left) shows the electric field around cathode and pickup electrodes simulated using Maxwell 3D, in which the anode voltage is set to 0V and a negative HV is applied to the cathode. There is a high electric field around the edge of the cathode. Figure 3.8 (right) shows the field strength along the line joining edges of cathode and pickup electrodes. The maximum field is about 200 kV/mm around the cathode edge. This high electric field caused occasional shorts between cathode and pickup electrodes. Therefore, improvements were needed for the stable operation.

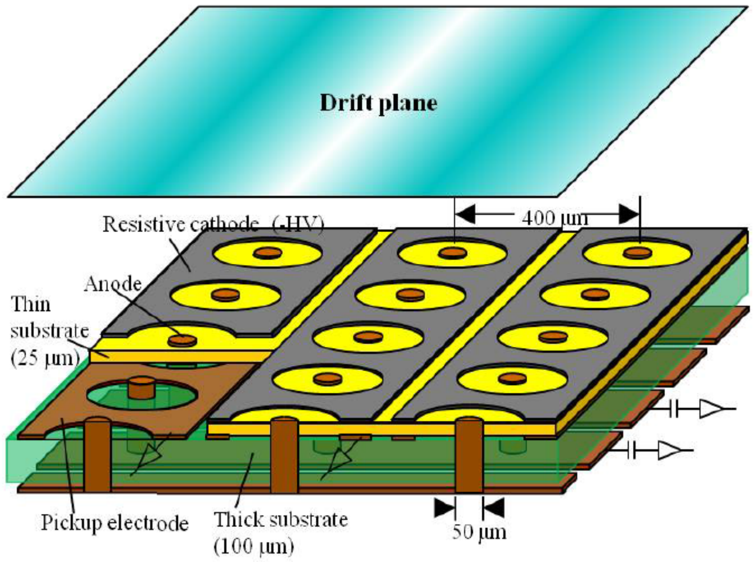

Figure 3.3: Schematic view of the resistive μ-PIC [14]. An insulating layer is sandwiched between the resistive cathode and the pickup electrode.

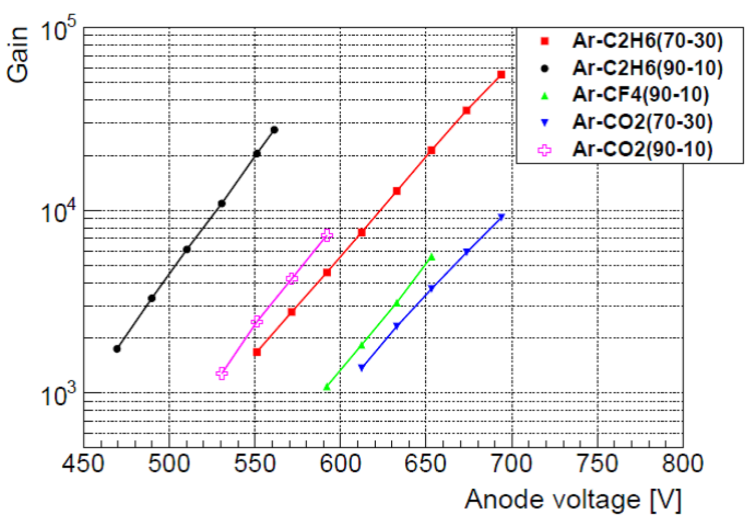

Figure 3.4: Gain variation of the resistive μ-PIC as a function of the amplification voltage. The gas gain more than 6×10^5 was achieved using Ar/C_2H_6 (7:3) gas mixture. [14]

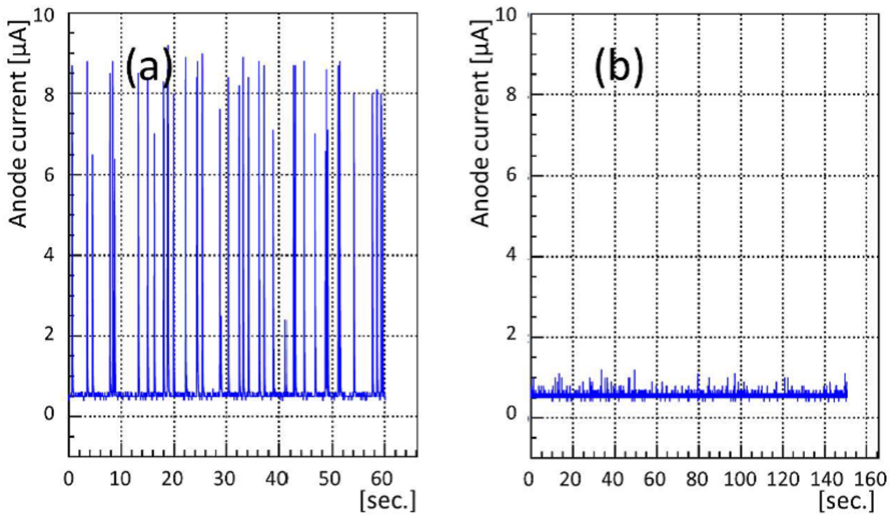

Figure 3.5: Monitored current under fast neutrons irradiation for the conventional μ-PIC (a) and the resistive μ-PIC (b) with the same gas gain. While large sparks are found with the conventional μ-PIC frequently, all sparks are suppressed below 1μA with the resistive μ-PIC. [14]

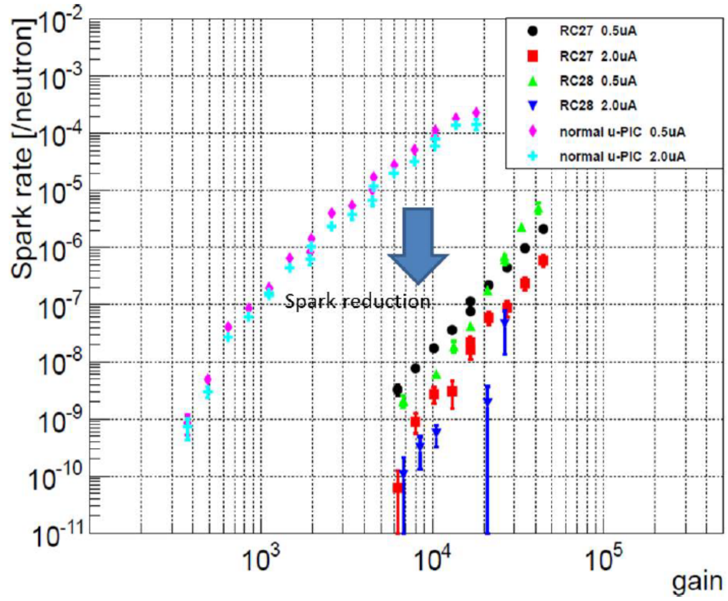

Figure 3.6: Spark rate of the conventional μ-PIC and the resistive μ-PIC as a function of the gas gain. The spark rate of the resistive μ-PIC was 10^{3-5} times lower than that of the conventional μ-PIC. [14]

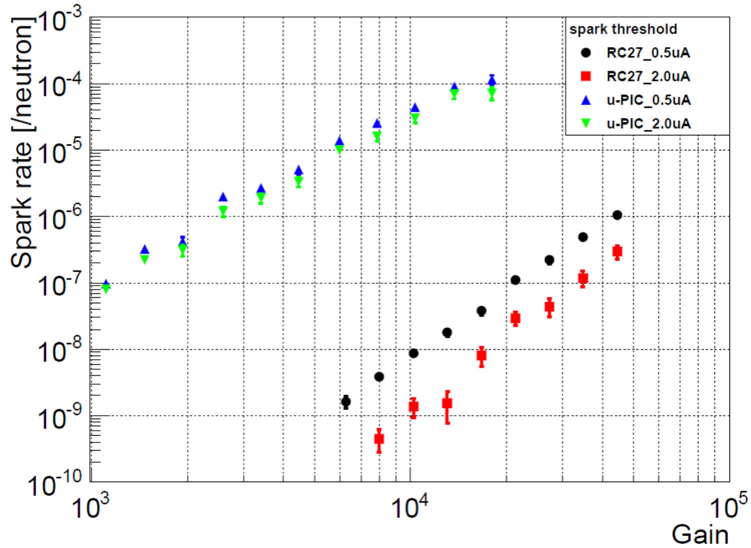

Figure 3.7: Spark rate using different threshold for the spark current. The thresholds were set to 0.5μA and 1μA. As for the resistive μ-PICs, the spark rate with a threshold of 0.5μA was about ten times higher than that of 2μA. On the other hand, there were no difference between two thresholds for the conventional μ-PIC. [14]

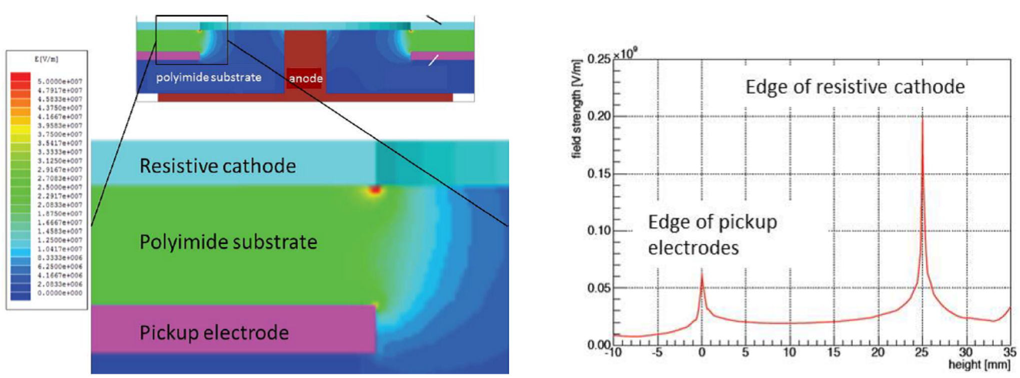

Figure 3.8: Left: Electric field around cathode and pickup electrodes simulated using Maxwell 3D, in which the anode voltage is set to 0V and a negative HV is applied to the cathode. Right: Field strength along the line joining edges of cathode and pickup electrodes. The maximum field is about 200 kV/mm around the cathode edge. [14]

Chapter 4

Design of a novel resistive μ-PIC

4.1 New ideas for the new μ-PIC to overcome problems for the former design

Although the resistive μ-PIC showed great tolerance to large sparks, it could not be applied for practical use due to problems in the design. Therefore, the detector design has been greatly improved. Three approaches have been performed to overcome problems for the former design.

4.1.1 Promising resistive electrodes made of DLC

Generally, higher tolerance against sparks can be obtained with higher resistivity of electrodes. However, higher resistivity makes serious problems in the case of high-rate applications. The average current of anodes and cathodes is grown up in the high-rate irradiation. Therefore, the gas gain will be decreased due to the voltage drop through the resistive electrodes. Hence, the resistivity must be tuned properly depending on requirements of the high-rate capability and of the tolerance to sparks.

As mentioned in chapter 3, a carbon-loaded paste was used for resistive electrodes, and previous studies have shown great tolerance to sparks. However, the resistivity cannot be controlled precisely. Therefore, alternative material was needed. As such a material, the DLC thin film (see section 2.1.6) has been developed as an ideal material for the μ-PIC. Figure 4.1 shows the microscopic images of the pixel of the μ-PIC. The carbon-loaded paste is used in the left picture and the DLC thin film is used in the right picture. The carbon-loaded paste has a thickness of about 10μm. As mentioned in section 2.6, the resistivity is affected by conditions of carbon particles in the paste. The variation in resistivity for former chambers was a factor of five in 10 $\times$ 10cm^2 detection area. On the other hand, the thickness of the DLC thin film is determined by the sputtering time for film growth, and it is order of 10-100nm which is greatly thinner than other components of the detector (10-100μm). The variation in resistivity was within 20% in 10 $\times$ 10cm^2 detection area.

The cathode voltage is supplied from both ends of resistive cathode strips. In high rate radiation environments, it is suspected that the voltage supply can not catch up with the voltage drop at center of strips. Therefore, adjacent resistive strips were connected every 16 pixels. Figure 4.2 shows the schematic view of the pattern of resistive cathode strips and their photographs. The pattern of resistive strips has ladder-like shape. The readout is not affected by this pattern because it is isolated from resistive strips.

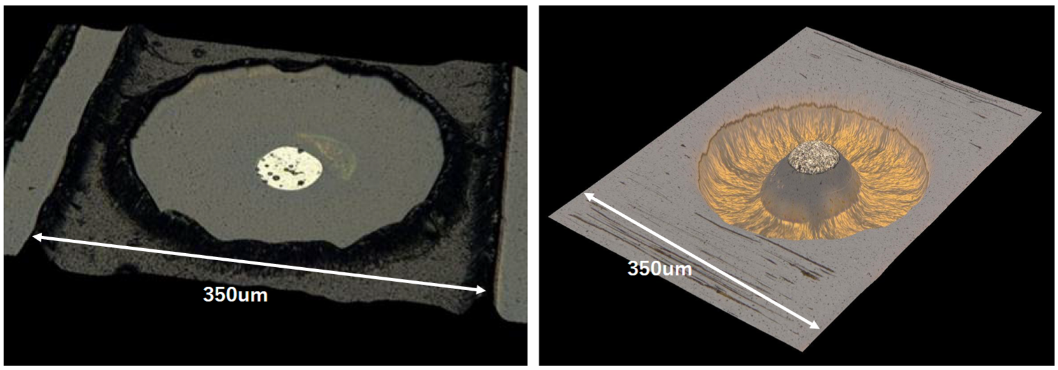

Figure 4.1: Microscopic images of the pixel of the μ-PIC. Left: Carbon-loaded paste, right: DLC film for the resistive cathode.

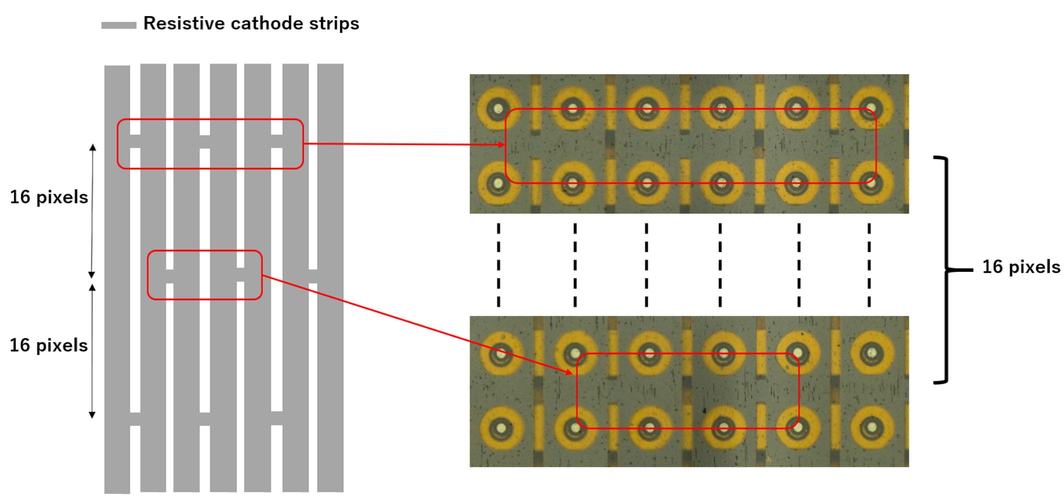

Figure 4.2: Schematic view of the pattern of resistive strips and their photographs. Adjacent resistive cathode strips were connected every 16 pixels. The pattern of resistive strips has ladder-like shape.

4.1.2 Accurate alignment of electrodes

The resistive μ-PIC consists of electrodes on double layers as described in section 3.2. The process of making electrodes is more complicated than that of the conventional μ-PIC. The accurate alignment between two layers as well as between anode and cathode electrodes is important in the fabrication. However, such a technique has not been established. Here, a solution to this problem will be described. Figure 4.3 shows a part of the fabrication process of our former chambers. At first, pickup strips are formed on the backside of the top substrate, and anodes are filled by nickel in the top substrate (1). Next, the bottom substrate is laminated (2). It has a copper layer which will be formed to anode strips later. Holes are made by laser drilling (3). They are filled with metal by the through-hole plating process, then anode strips are connected to top anodes (4). However, some holes were found to be displaced and mis-connected to nearby cathode pickups. It was caused due to difficulties in manual alignment between the top and the bottom substrate. Because holes were drilled from backside without seeing the anode pattern on the front side, it is difficult to match positions correctly. Such a displacement has caused the short circuit between the anode and the pickup. Only a part of the detection area could be operated in our first trial.

To solve this problem, the material of the bottom substrate was replaced to a dry film. Also, hole making processes were changed to photolithography. Figure 4.4 shows the new process. Since the dry film is transparent, top anodes could be seen from backside (2). Holes were correctly aligned by photolithography and top anodes and anode strips were connected properly in each pixel (3-5). Figure 4.5 shows the microscopic images of the former μ-PIC and the new μ-PIC. For the former μ-PIC, top anodes (white patterns) and bottom anodes (yellow patterns) are mis-aligned, whereas they are well aligned for the new μ-PIC. Thanks to this improvement, no failures were found in all pixels in $10 \times 10\text{cm}^2$ detection area.

4.1.3 Novel approaches for making a compact detector

If a high voltage is applied for an electrode, a pair of a resistor and a capacitor is mandatory for signal readout. The resister is needed for the HV bias, and the capacitor is needed for the AC coupling. Figure 4.6 shows the gas package of the former chamber, where resistors for HV bias and capacitors for AC coupling are put. In the former design, 16 strips were combined to 1 channel readout for simplification, then only 16 pairs of RC were needed for the anode. However, a large space was needed for putting those parts. Mounting those parts on a board is a general way for reading signals from all strips individually. On the other hand, there is a possible way in which the μ-PIC becomes a very compact detector. As mentioned in section 3.2, when a negative HV is supplied to the cathode and the anode voltage is set to 0V, those parts can be removed. However, this mode is unstable due to the high electric field near the edge of pickup strips. It is preferable to supply HV to the anode for the stable operation.

The best solution has been provided by DLC and PCB techniques. First, HV bias resistors for the anodes were formed on the surface of the detector by carbon sputtering. The microscopic image of DLC resistors for HV bias is shown in Figure 4.7. Each DLC resistor is connected to the anode strip via through hole (see Figure 4.11). Second, Figure 4.8 shows the cross-section of the μ-PIC. The substrate was glued on the rigid board which has readout strips for anodes. Readout strips are put parallel to anode strips of the μ-PIC. The capacitors are formed by the polyimide gluing sheet and an anode strip and a readout strip, and its capacitance is about

22pF/strip for 300μ width and 10cm log strips. Although this value is lower than that we want, it is enough for practical use. Thus, additional RC circuits have been no more needed for our μ-PIC. Figure 4.9 shows the μ-PIC substrate and that glued on the rigid board. Signals can be obtained directly from on-board connectors.

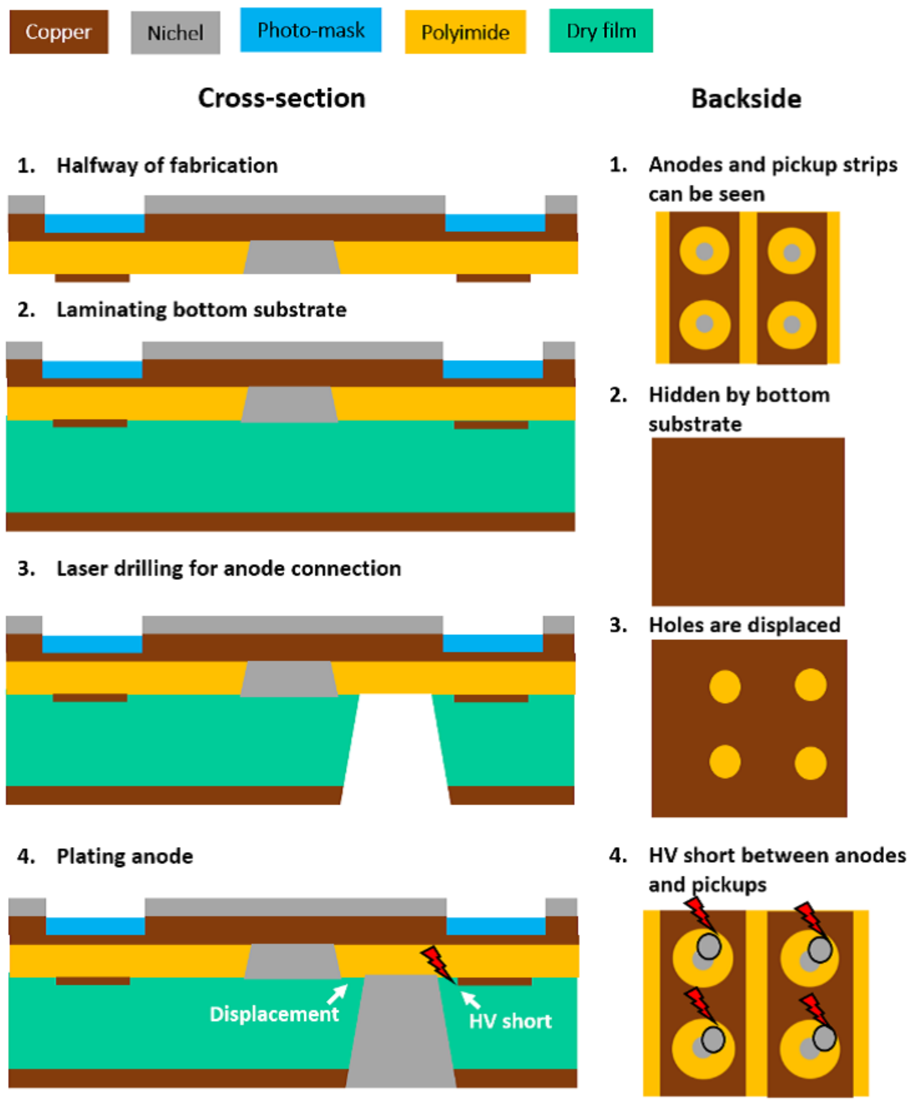

Figure 4.3: Former fabrication-process which caused the mis-alignment in anodes. The looks from backside are also shown as well as from the cross section. In the laser drilling process (2, 3), top anodes were hidden by the bottom substrate. Therefore, some anodes were displaced nearby the pickups. Such a displacement has caused voltage short between the anode and the pickup.

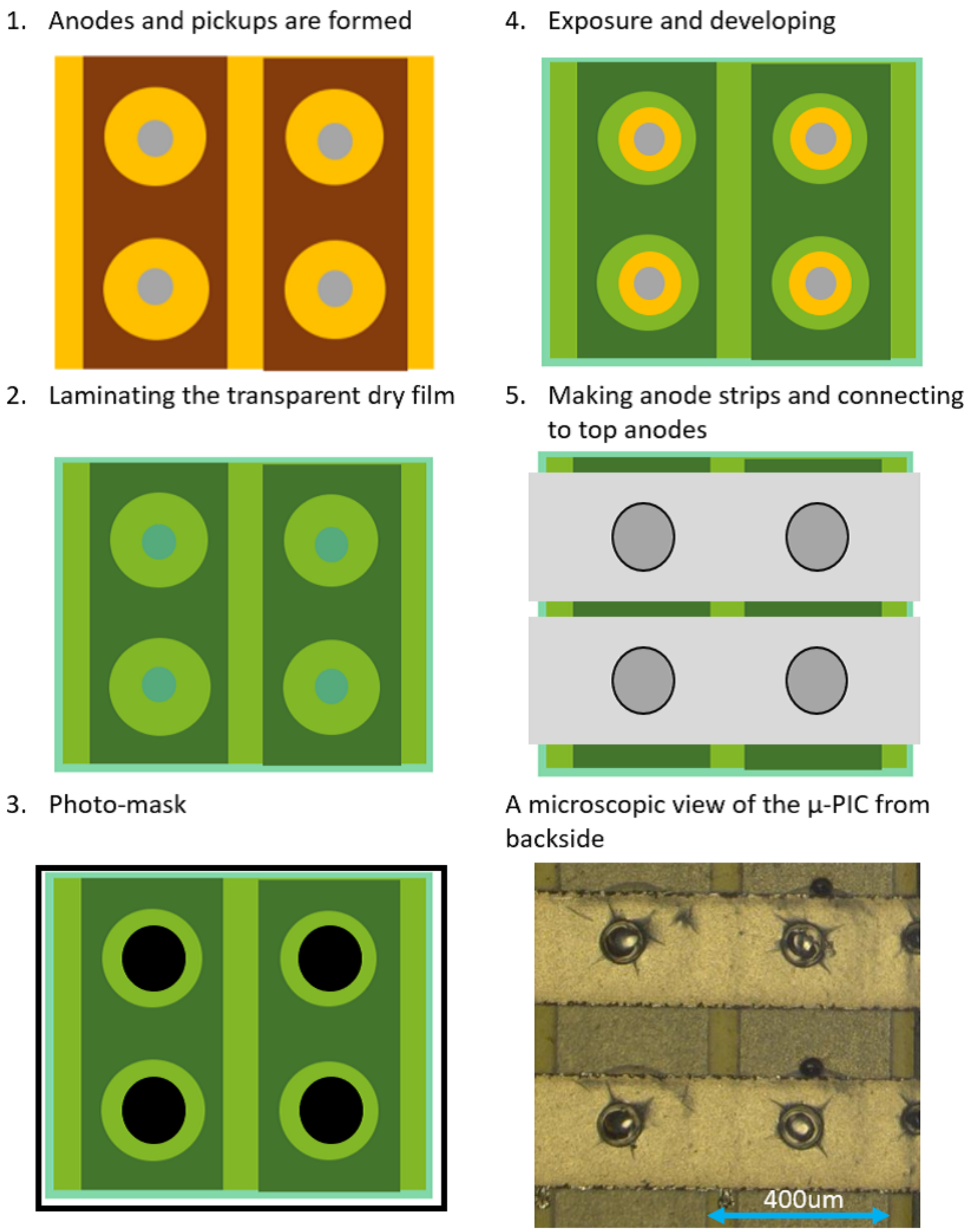

Figure 4.4: New process for making the anode. All anodes could be well placed by means of the transparent dry film and photolithography.

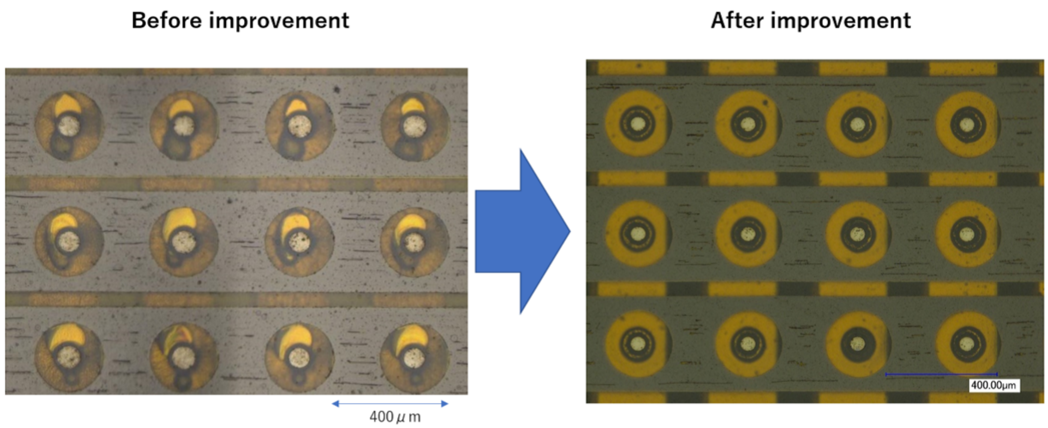

Figure 4.5: Microscopic images of the former μ-PIC (left) and the new μ-PIC (right). For the former μ-PIC, top anodes (white patterns) and bottom anodes (yellow patterns) are mis-aligned, whereas they are well aligned for the new μ-PIC.

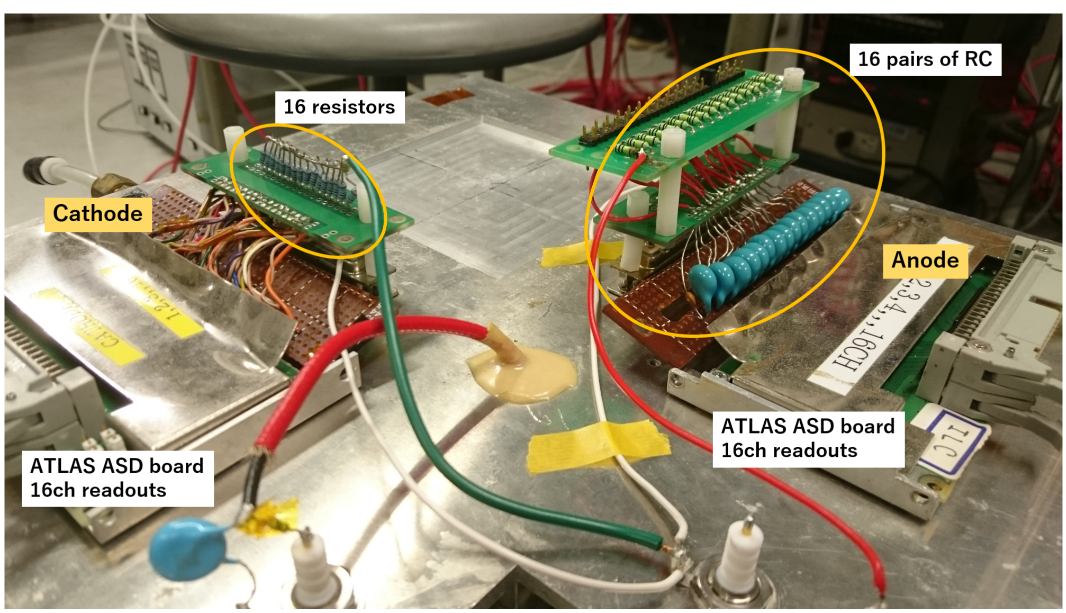

Figure 4.6: RC circuits and readout boards mounted on the former design. 16 pairs of RC circuits were mounted for the anode. Capacitors were not needed for the cathode because it obtains induced charges.

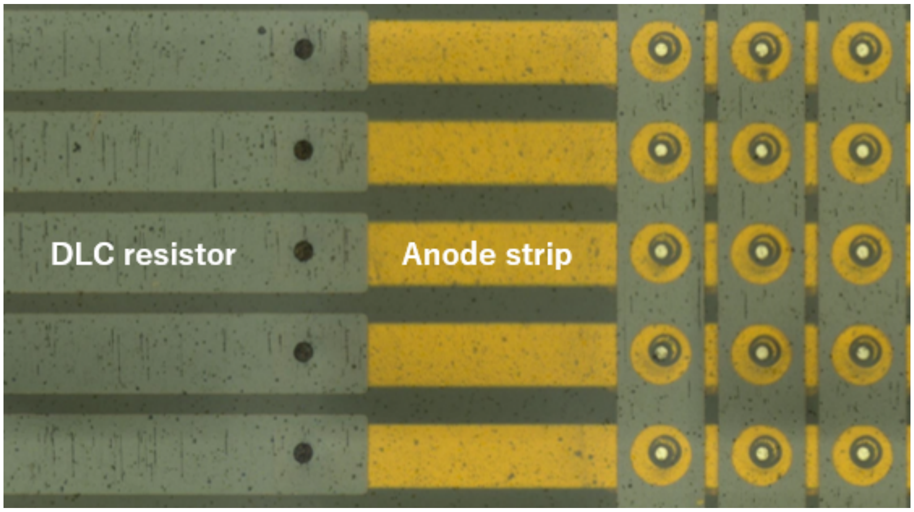

Figure 4.7: Microscopic image of the μ-PIC and DLC resistors. Yellow lines are anode strips which are connected to each resistor.

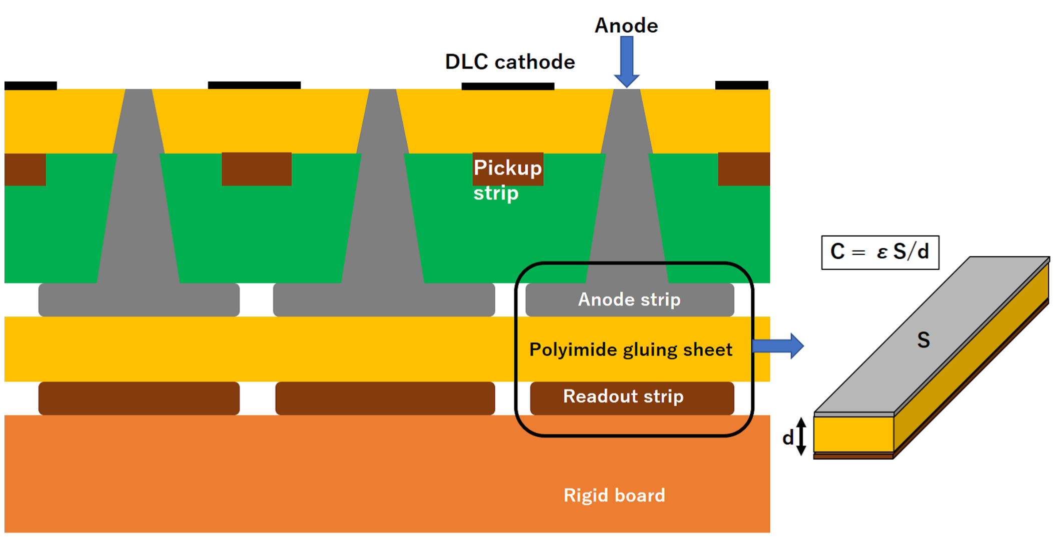

Figure 4.8: Schematic cross section of the new prototype on the rigid board. Polyimide gluing sheet and an anode strip and an readout strip form a capacitor. Thanks to this structure, all capacitors for the anode readout have been removed from our μ-PIC.

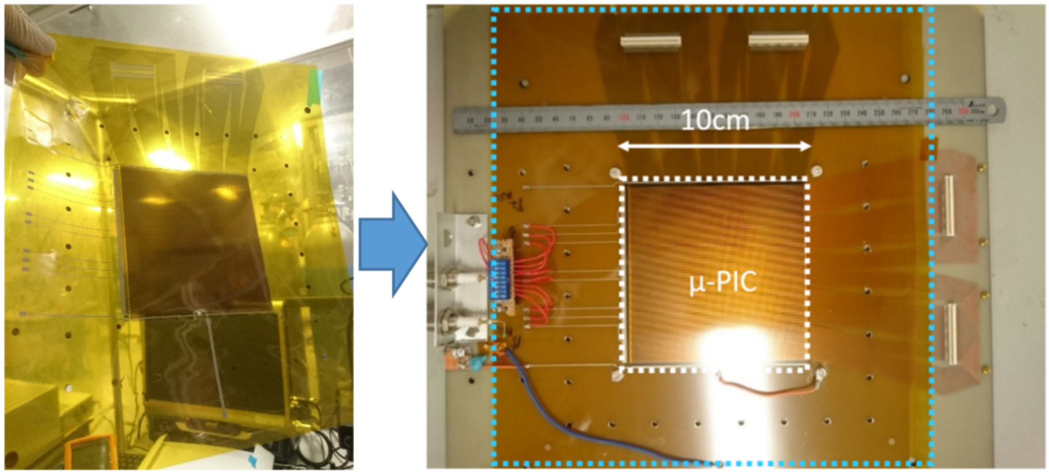

Figure 4.9: Left: μ-PIC substrate before gluing on the rigid PCB board. Right: μ-PIC on the rigid board. Equivalent circuits for the readout are all in this board. Signals can be obtained from on-board connectors directly.

4.2 Fabrication-process

The resistive μ-PIC was fabricated by Raytech Inc. Figure 4.10 shows the fabrication process of the new resistive μ-PIC. Mask patterns for cathode strips and pickup strips for them are formed on top and bottom, respectively, on surface of 25μ thick FPC (Flexible Print Circuit) (1-5). Mask patterns for DLC resistors for HV bias are also formed in this process (not described in this figure). The substrate at the center of circles on the cathode are etched and anodes are formed by plating Nickel in the etched hole (6-10). The dry film is laminated on the bottom surface (11). Holes corresponding to the position of each anode are made by photolithography (12). Anode strips are formed perpendicular to cathode strips and connected to the top anodes (13). Resistive cathodes are made by carbon sputtering (14-17). Finally, the detector is glued on the rigid PCB which has readout strips for anodes (18).

4.3 Properties of the detector

Figure 4.11 shows a schematic view of the cross-section of the new μ-PIC. The connection between a DLC resistor and an anode strip is also described. Figure 4.12 shows the detector in the gas package. APV25 frontend chips [34] are attached to the detector via connectors. Table4.1 shows the parameters of the new μ-PIC. There are four chambers classified into two types. For RC37 and RC38, the anode diameter is 70-75μm, the thickness of the dry film is 50 μm, and the surface cathode resistivity is $\sim$180kΩ/sq. For RC41 and RC42, the anode diameter is 55-60μm, the thickness of the dry film is 64μm, and the surface cathode resistivity is $\sim$600kΩ/sq.

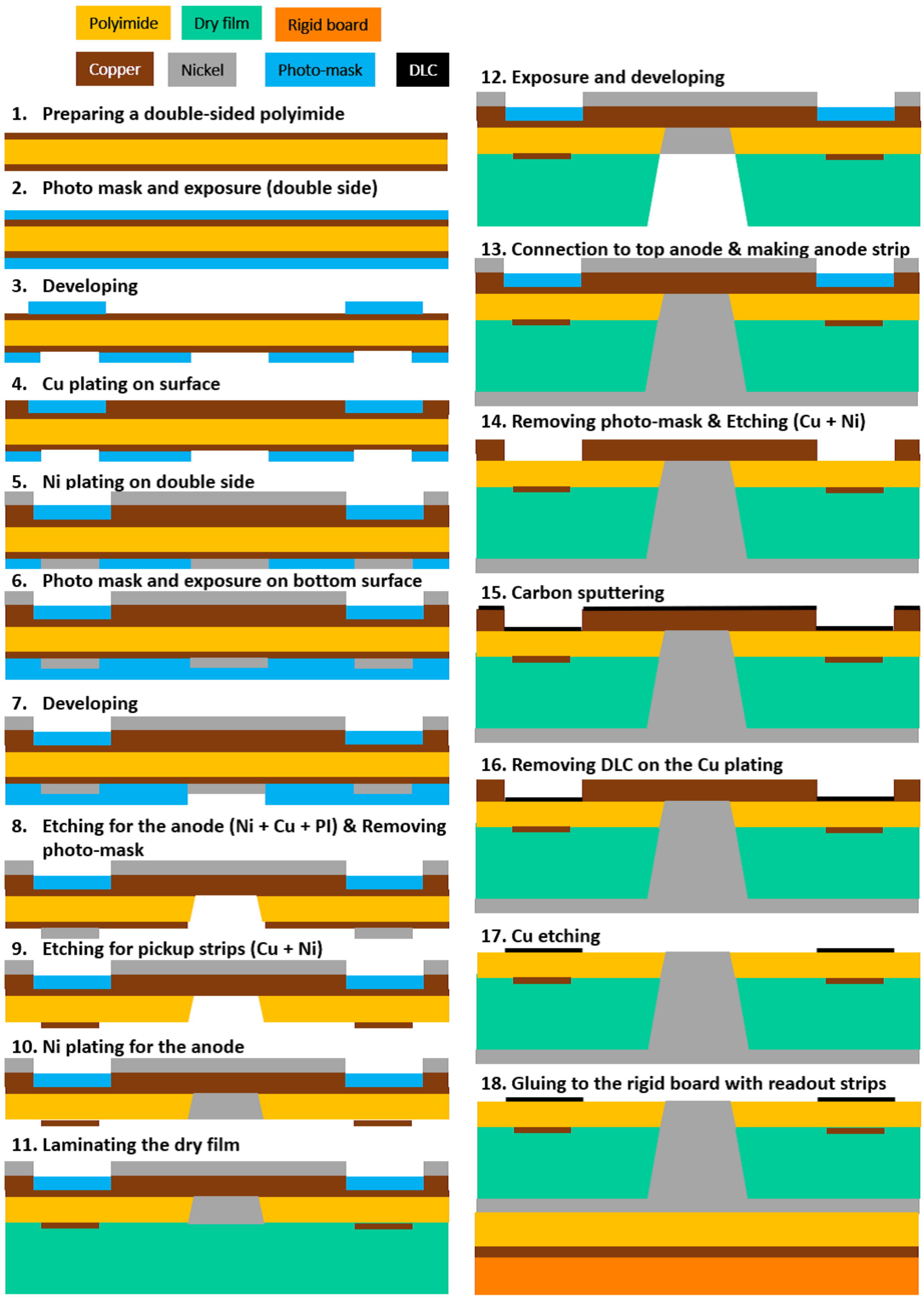

Figure 4.10: Fabrication process of the new μ-PIC.

Chamber name	Diameter size		Thickness of	Resistivity
	Anode[μm]	Cathode[μm]	dry film[μm]	[kΩ/sq.]
RC37, RC38	70-75	240-250	50	180
RC41, RC42	55-60	240-250	64	600

Table 4.1: The parameters of produced detectors.

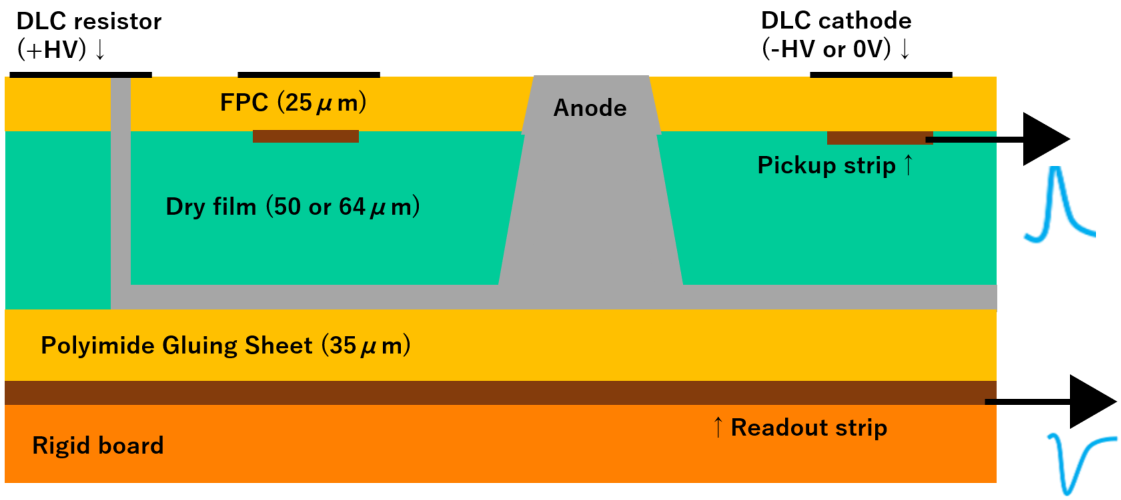

Figure 4.11: Cross section of the new μ-PIC.

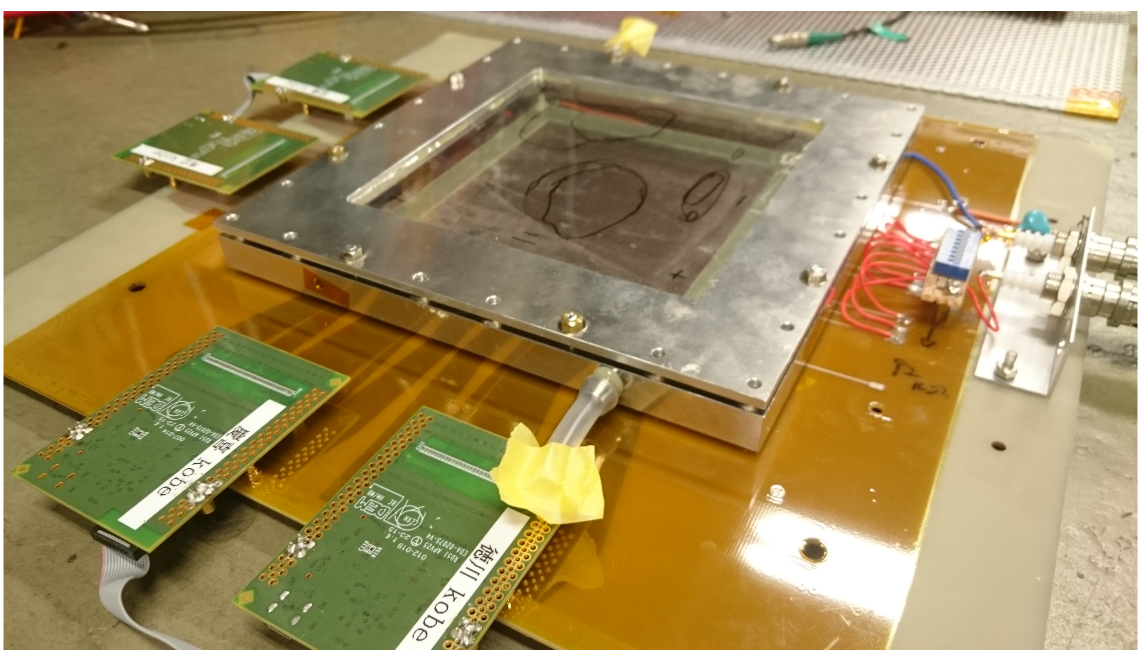

Figure 4.12: New μ-PIC in the gas package. APV25 frontend chips are attached to connectors on the μ-PIC board.

4.4 Basic performances of the new μ-PIC

4.4.1 Gas gains

Gas gains were measured using ^{55}Fe 5.9keV X-ray source with Ar/C_2H_6 (9:1, 8:2, 7:3) and Ar/CO_2 (93:7) gas mixtures. The drift field was set to 3kV/cm for the a drift gap of 3mm. The cathode voltage was set to 0V. Gain curves were obtained by varying anode voltage. ATLAS ASDs with analogue output (charge gain: 0.8V/pC) [35]) were used for the preamplifier. The spectrum of signals was measured by Multi Channel Analyzer (MCA8000D). As for the Ar/C_2H_6 (9:1) and Ar/CO_2 (93:7) gas mixtures, signals from cathodes were also measured. Figure 4.13 shows the measured gas gains as a function of the amplification voltage. The gas gain of more than 6000 were achieved with all gas mixtures. The maximum achievable gain of more than 10^4 was obtained with the Ar/C_2H_6 (9:1) and Ar/CO_2 (93:7) gas mixtures. Signal charge of cathodes was found to be larger than those of anodes. The reason of this result is suspected that charges are decreased due to the low capacitance for the anode. Figure 4.14 shows the charge spectrum obtained from anodes (left) and cathodes (right), where 32 $\times$ 32 pixels were irradiated by collimated X-rays. The main peak corresponding to the photoelectric peak of 5.9keV and the escape peak (2.7keV) are clearly seen and the resolution is $\sim$20% (FWHM) for both readouts.

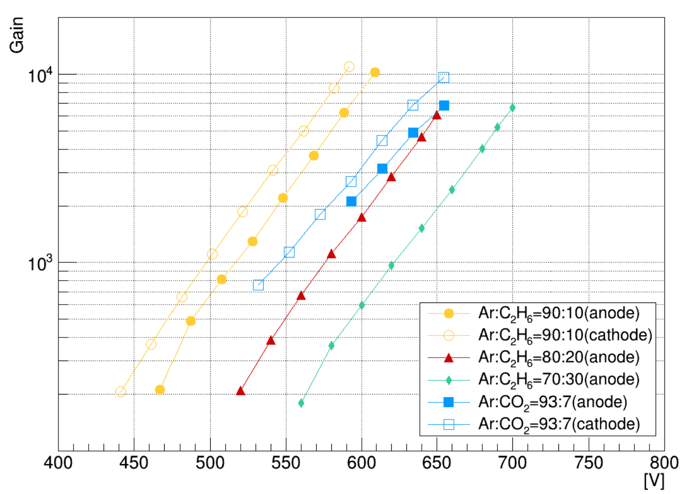

Figure 4.13: Gas gains for various gas mixtures as a function of the amplification voltage.

4.4.2 Uniformity of gas gains

The uniformity of gas gains over the whole detection area has been tested. The detection area was divided into 8 $\times$ 8 areas, in each of which there are 32 $\times$ 32 pixels. The map and distribution of gains obtained from anodes and cathodes are shown in Figure 4.15 and Figure 4.16, respectively. Gas gains are normalized by

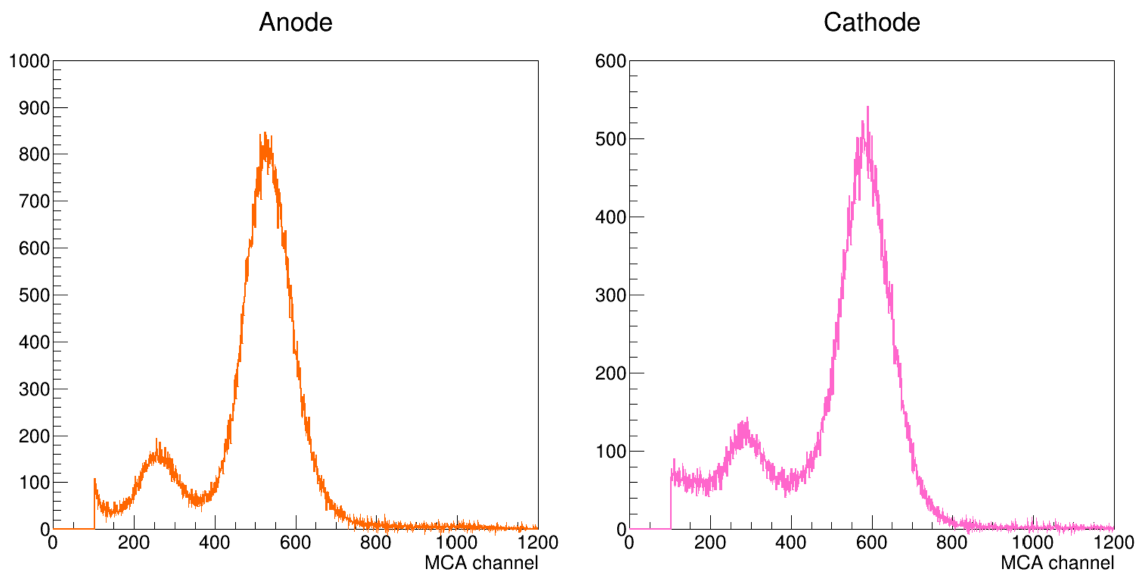

Figure 4.14: Charge spectrum of ^{55}Fe X-rays obtained from anodes (left) and cathodes (right) at the same irradiation area of 32 $\times$ 32 pixels. The gas gain is $\sim$1000.

the medium value of 1080 for the anode and 1090 for the cathode. Except for a few points, variations of gas gain does not exceed $\pm$30%.

4.4.3 High-rate capability

The high-rate capability of the new μ-PIC has been tested by irradiating 8keV X-rays from a Cu target at RD51 laboratory in CERN. In this test, collimated X-rays were irradiated at $\sim$6mm$\times$20mm detection area. The rate of X-rays was controlled by changing the current of cathode of the source. The maximum rate is $\sim 1.3 \times 10^7$cps/cm^2, determined by the specification of the X-rays source. Figure 4.17 shows the anode current of the μ-PIC as a function of the intensity of X-rays. The μ-PIC could be operated under the irradiation up to $\sim 1.3 \times 10^7$cps/cm^2.

4.4.4 X-ray imaging

The imaging test has been performed using 8keV X-rays source of RD51 laboratory. This is the same source mentioned in section 4.4.3. The SRS/APV25 readout system was used for the data aquisition. When there is only one cluster on both readouts, the two-dimensional position was filled. Figure 4.18 shows a test pattern and its X-ray image. It can be seen that 1mm slits are well separated. Figure 4.19 shows a key and its X-ray image. The shape of the blade and a hole of 5mm diameter are clearly seen. Figure 4.20 shows a bat and its X-ray image. The skeleton, the contour of the body, and the left thumb claw is clearly seen. Also, left toe claws are slightly seen. Thus, it was found that the fine X-ray images can be obtained using the new resistive μ-PIC.

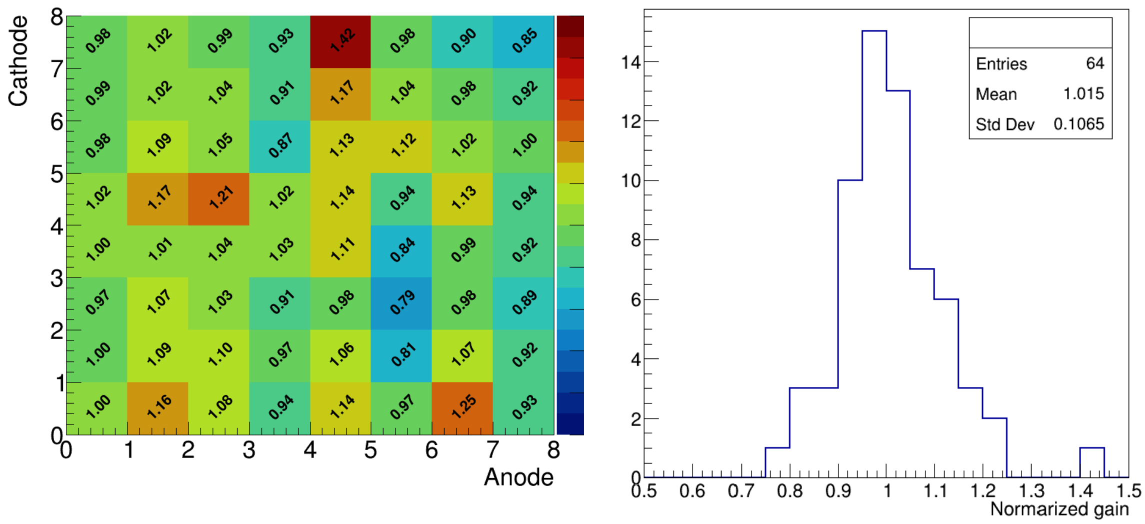

Figure 4.15: Gain map (left) and its distribution (right) obtained from anodes.

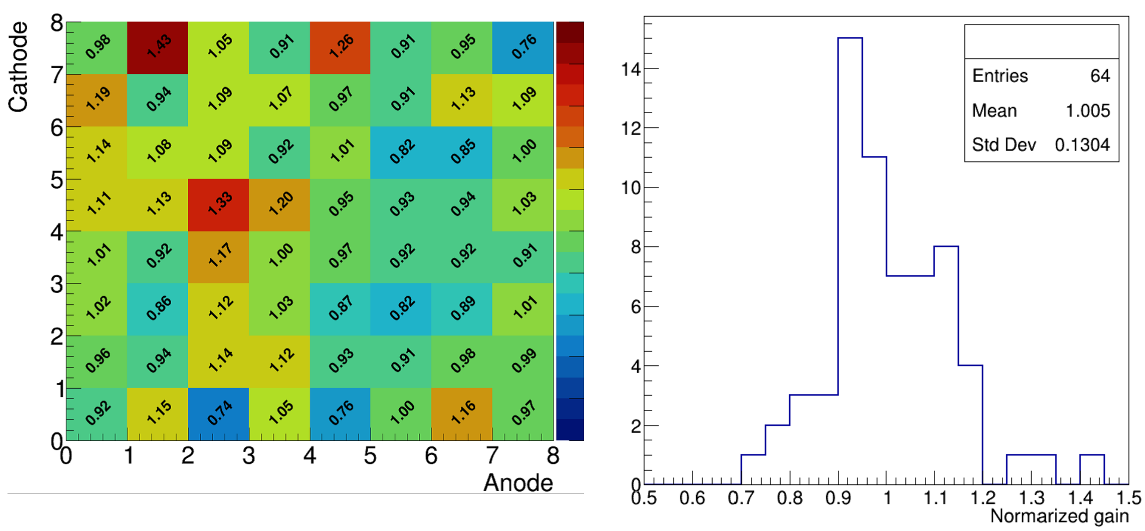

Figure 4.16: Gain map (left) and its distribution (right) obtained from cathodes.

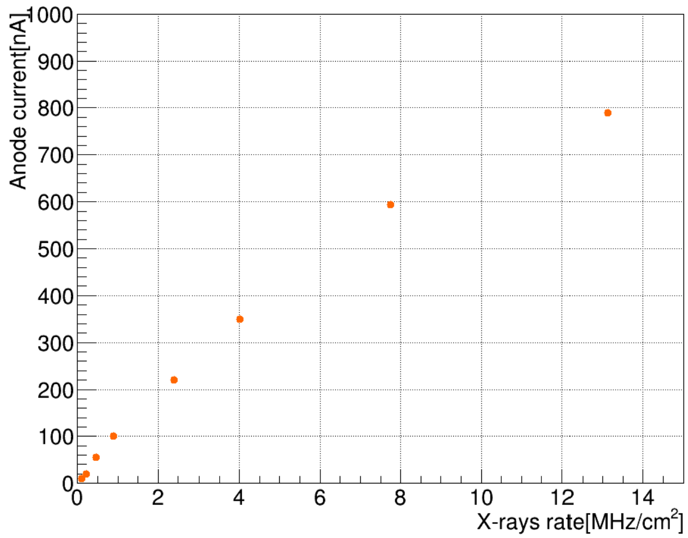

Figure 4.17: Anode current of the μ-PIC as a function of the intensity of X-rays.

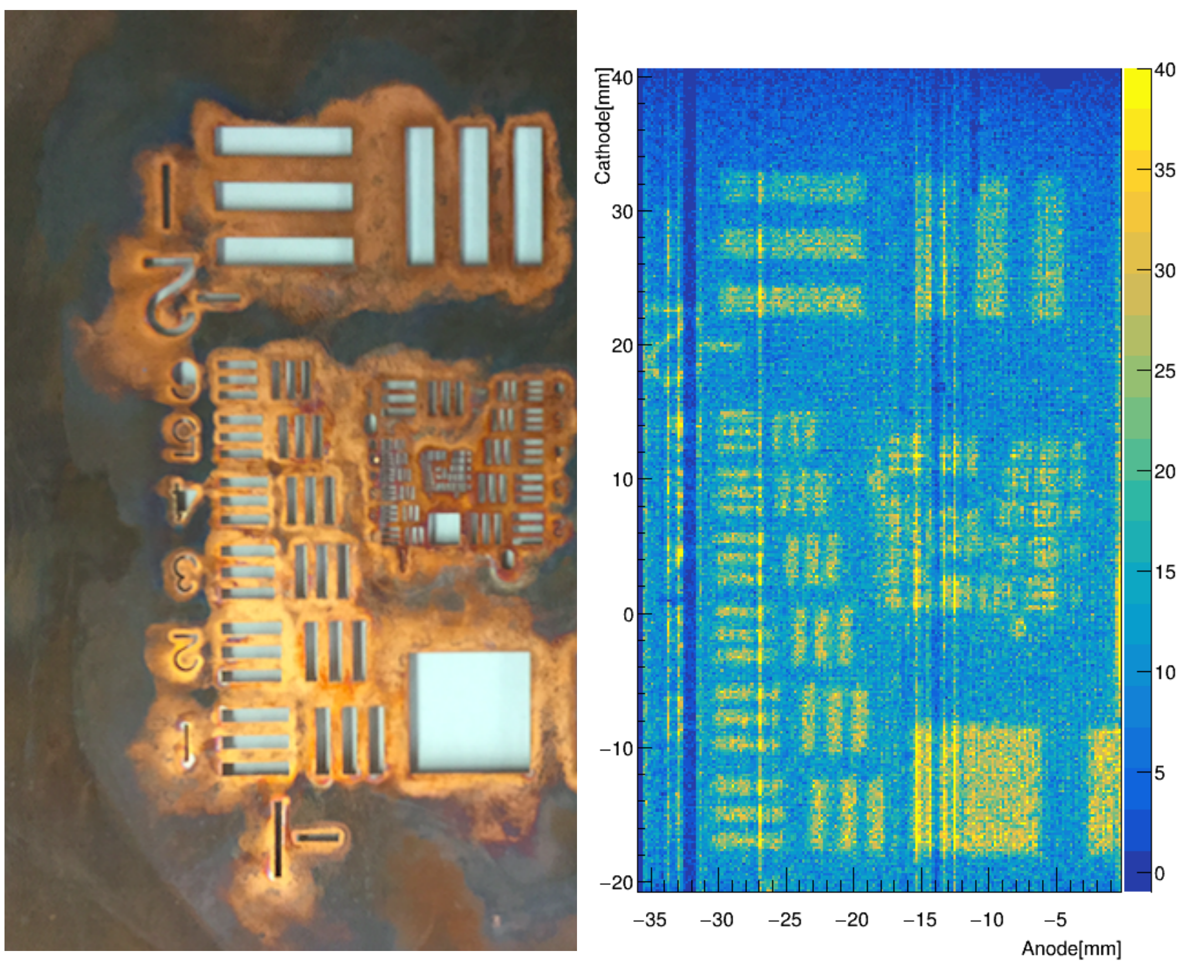

Figure 4.18: Test pattern and its X-ray image.

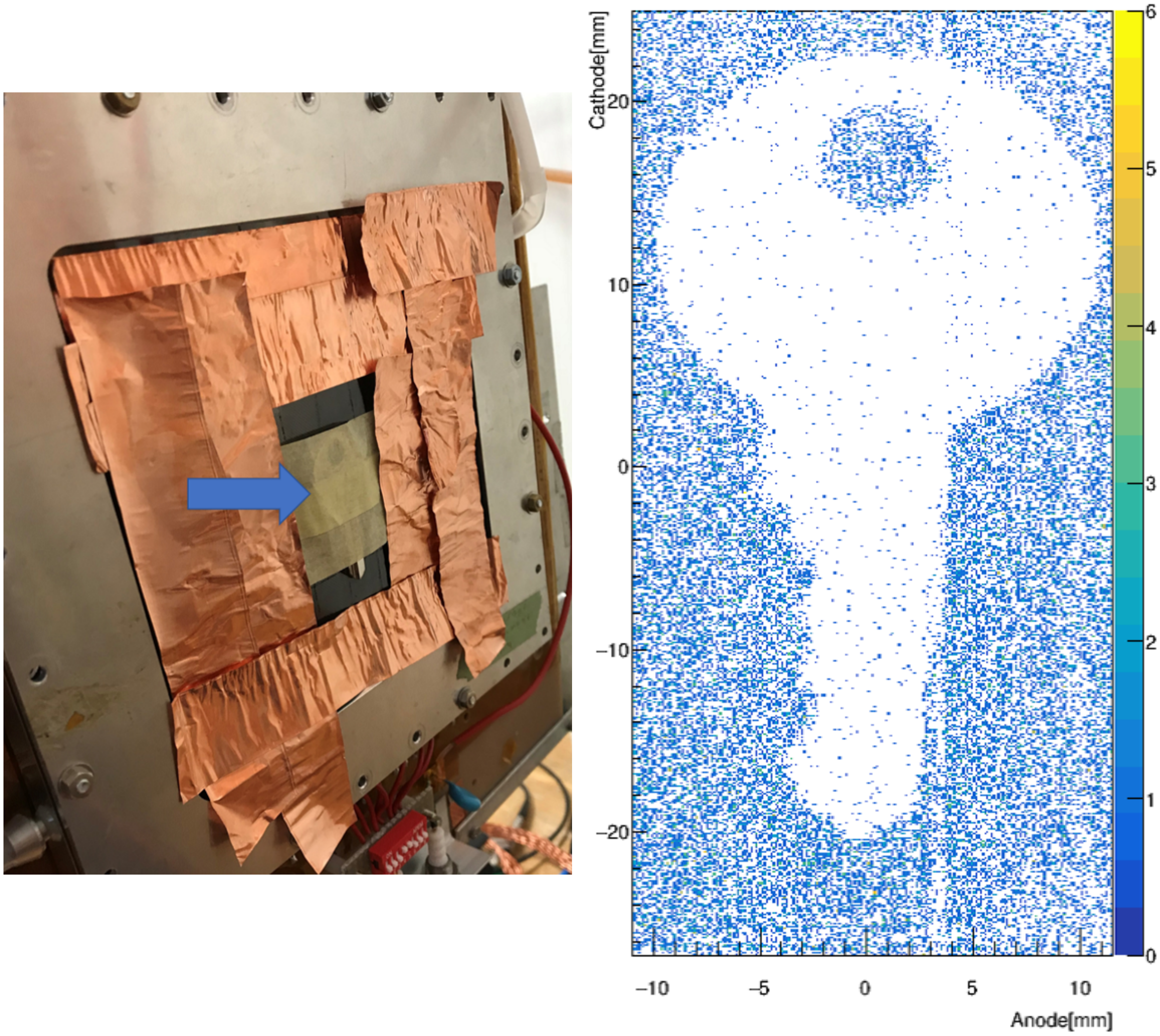

Figure 4.19: Key on the μ-PIC and its X-ray image.

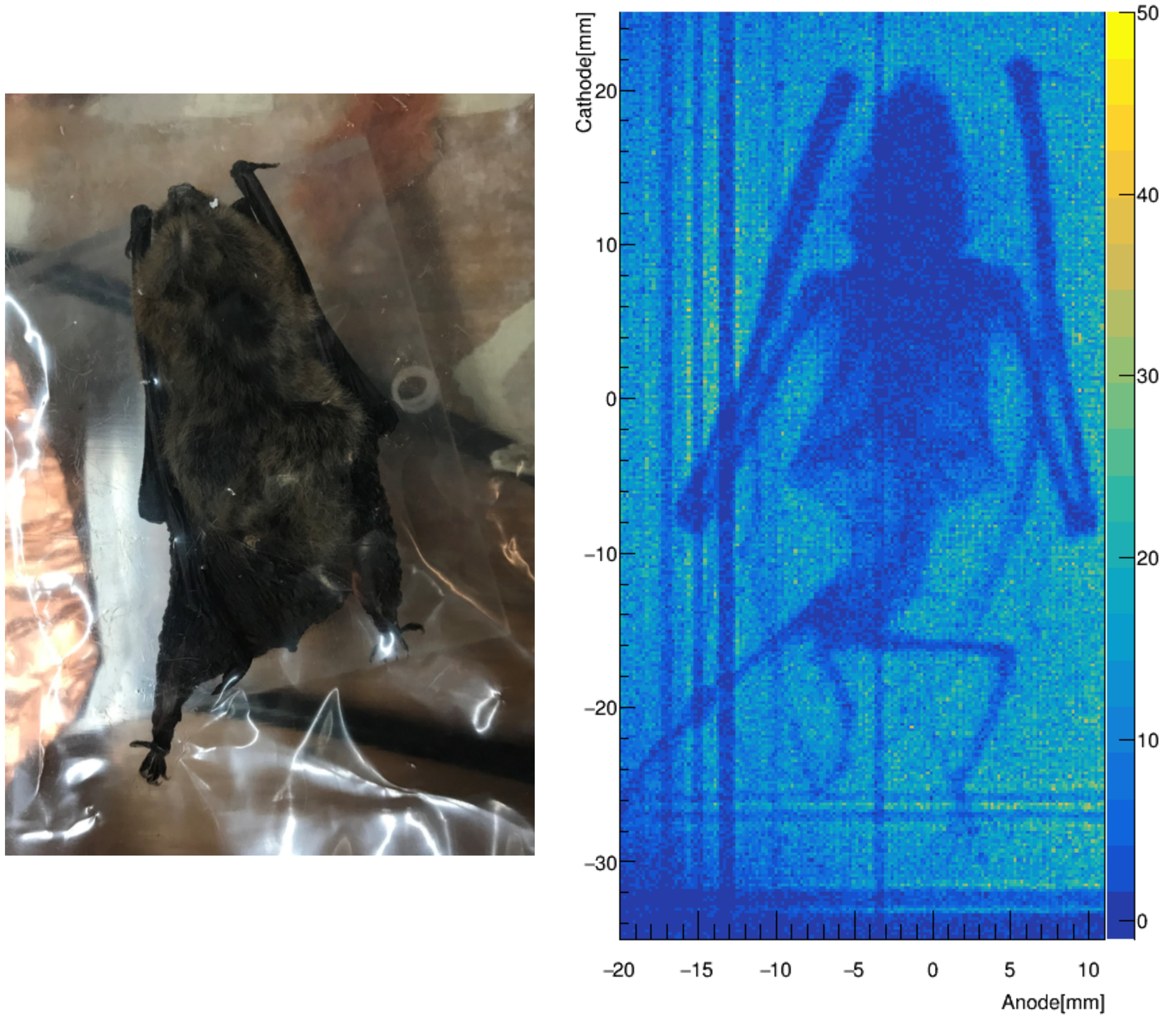

Figure 4.20: Bat and its X-ray image.

Chapter 5

Performance study for the charged particles at CERN SPS test beam

5.1 Experimental setup

Tracking performances of the μ-PIC were studied using charged particles beam. The main objective of this test was to evaluate the two-dimensional position resolution of the new μ-PIC. Also, the time resolution and the detection efficiency were measured. The test was performed in October 2017 at the SPS H4 beam line in CERN [36,37]. H4 is located at the North Areas of the SPS (Figure 5.1). The secondary beams (muons and pions) are delivered from the T2 target on which the 400 GeV/c primary proton beam is transported. The momentum of the secondary beams was set to 150GeV/c. Each beam spill lasts about 4 seconds. By closing the beam shutter, only the muons beam is derived. The intensity of the muon beam was $\sim 10^5$/spill.

Four μ-PICs (RC37, RC38, RC41, RC42) were tested. The drift field of RC37 and RC38 was set to 3kV/cm with a drift gap of 3mm. The drift field of RC41 and RC42 was set to 1kV/cm with a drift gap of 5mm. Figure 5.2 and Figure 5.3 show the experimental setup in this test. Two μ-PICs which have same properties were put in a back-to-back configuration as shown in Figure 5.2. Two Micromegas chambers with two-dimensional readouts (Tmm2, Tmm5) were used for beam telescopes [38]. Micromegas chambers have 360 strips with a pitch of 250μm for both readouts and an active area of $9 \times 9\text{cm}^2$. The drift field was set to 600V/cm with a drift gap of 5mm. Two plastic scintillators of $10 \times 10\text{cm}^2$ were used for the trigger. μ-PICs were operated with Ar/CO_2 (93:7) or Ar/C_2H_6 (7:3) gas mixtures. Micromegas chambers were operated with Ar/CO_2 (93:7) gas mixture.

5.2 Data acquisition

The data acquisition system was based on the SRS (Scalable Readout System) [39] with the APV25 front-end electronics [34] (Figure 5.4). The SRS has been developed by the CERN RD51 collaboration. It consists of ADC (Analogue Digital Converter), FEC (Front-End Concentrator) cards, front-end electronics (APV25 in this test), and other parts such as the power supply. The APV25 chip with 128 channel readouts was originally developed for the silicon strip detector of the CMS tracker

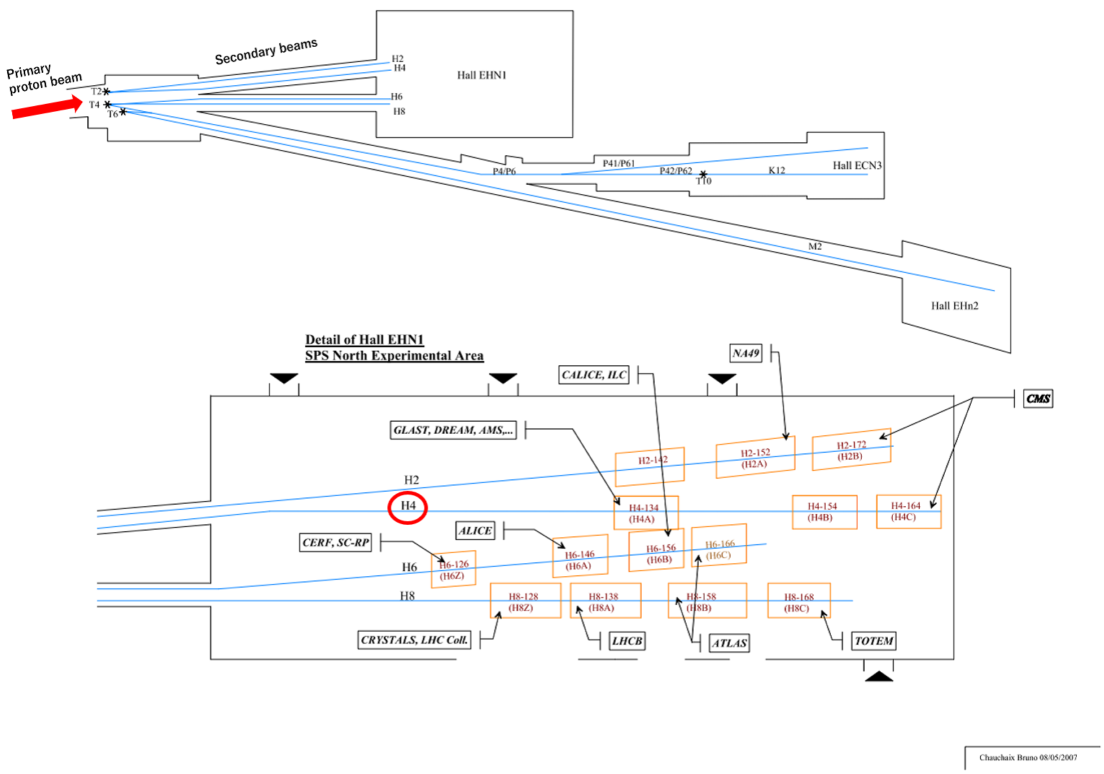

Figure 5.1: Layout of the SPS North Areas. Secondary beams (muons and pions) are derived by the primary proton beam and the T2 target [37]. By closing the beam shutter, only the muons beam is derived.

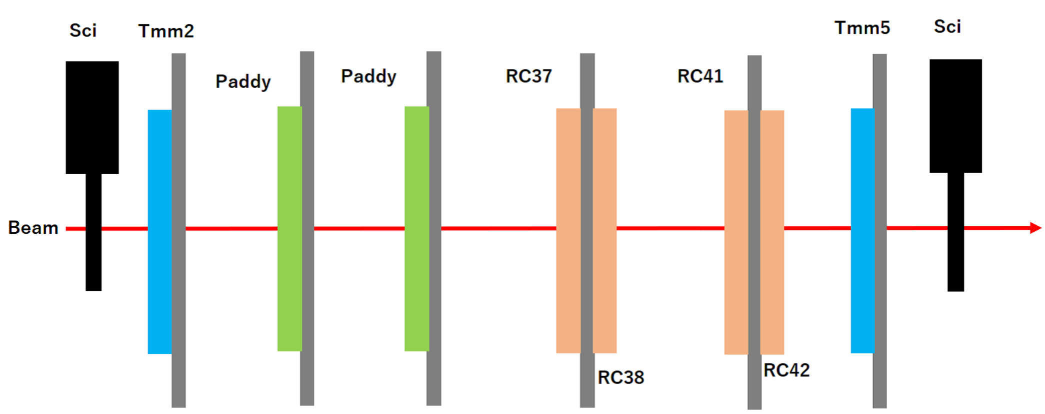

Figure 5.2: Experimental setup of the test. Four μ-PICs (RC37, RC38, RC41, RC42) are put between two Micromegas chambers (Tmm2, Tmm5) and trigger scintillators. Each two μ-PICs are set to back-to-back configuration. "Paddy" is another type of detectors and not related to my analysis.

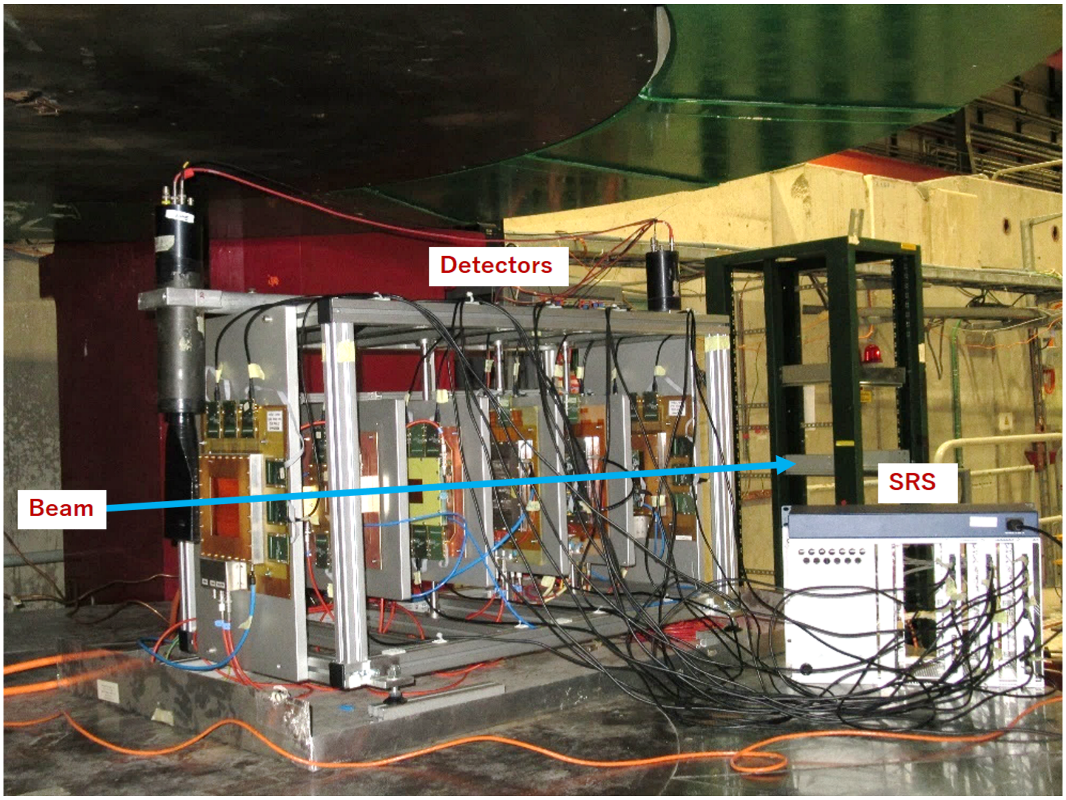

Figure 5.3: Photograph of the experimental setup.

[34]. Detector signals are fed to charge amplifiers with 50ns CR-RC shaper and then sampled by 40MHz clock. The analogue signal of 128ch are sampled in each 25nsec, and multiplexed signals from two APVs (total 256ch) are feed to the ADC card using standard HDMI cable. Once a trigger is invoked, 15 cycles of multiplexed signals (correspond to 375nsec) are read and recorded as one frame. Signals are digitized by the ADC card and sent to the DAQ PC via a Gbit Ethernet by the FEC. Since the ADC card has eight HDMI ports, 2048 channels can be processed by one combo of the ADC/FEC cards. Figure 5.5 shows the block diagram of the readout process in this setup. Two ADC/FEC combos were used for the readout of negative signals of μ-PIC anodes, and Micromegas chambers, and one ADC/FEC combo was used for that of positive signals of μ-PIC cathodes. A trigger signal from two scintillators was once sent to a CTGF (SRS Clock and Trigger Generator & Fun-out) card. Then a common trigger was distributed to three FEC cards by the CTGF. This scheme enabled the data acquisition without any time lag between multiple FEC cards. Signals from three FEC cards were merged by a network switch, and sent to the DAQ PC via one Ethernet cable. The "mmDAQ" software developed by MAMMA (Muon ATLAS MicroMegas Activity) was used for data taking. With mmDAQ, position, time and charge informations are recorded.

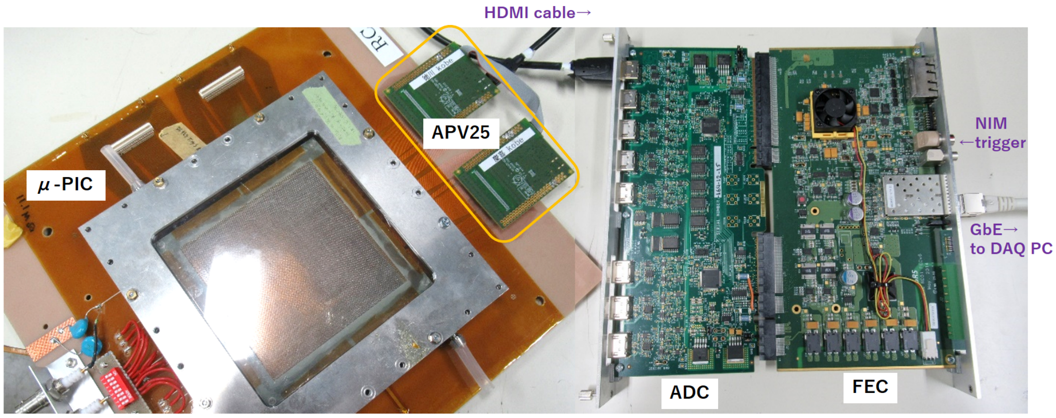

Figure 5.4: Photograph of the μ-PIC with the SRS.

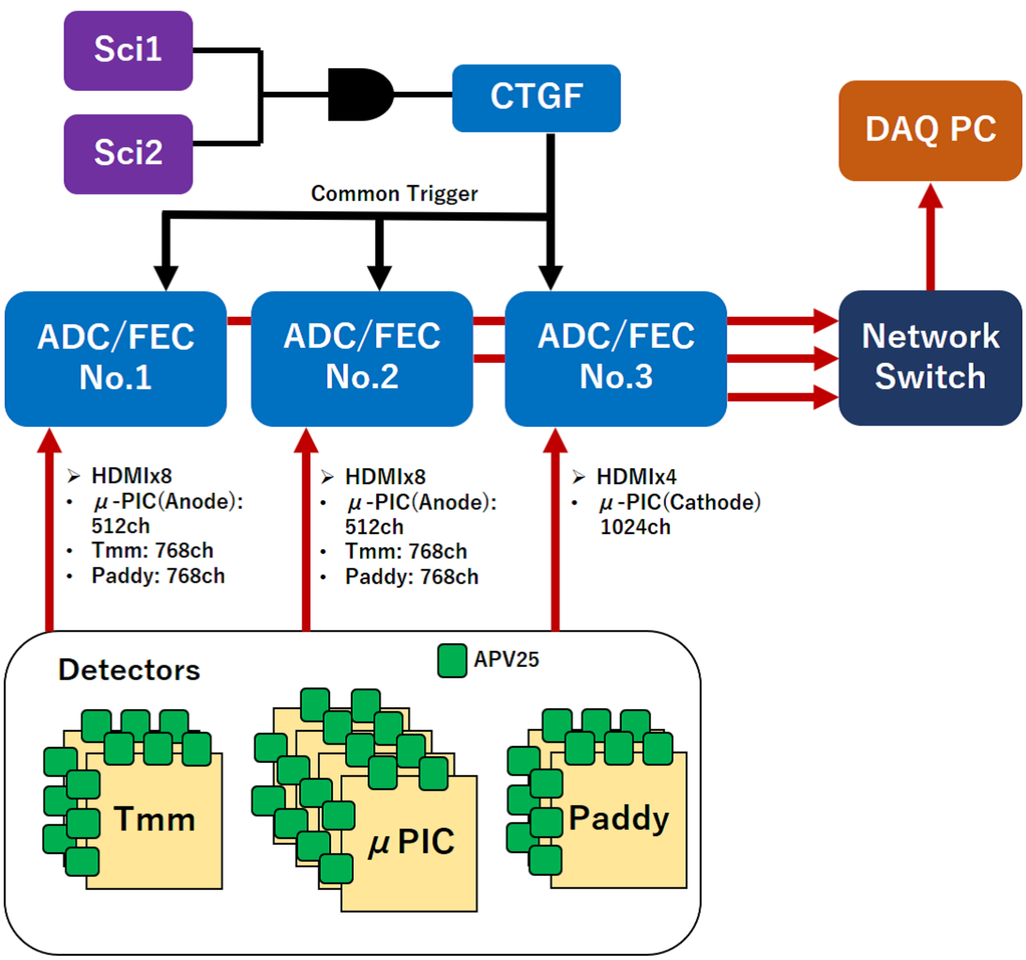

Figure 5.5: Block diagram of the readout process.

5.3 Signal processing

Figure 5.6 shows a three dimensional event display of a typical muon event on the μ-PIC. There are three axis, "Strip", "Time[ns]" and "ADC count". "Strip" means the number of the strip with a range of 1-256 for each readout. Shaper output signal is sampled every 25ns during 15 cycles for each strip in each event. Therefore, each event has these three informations. Following parameters are defined for the analysis.

- strip: Hit strip number (position).
- time: Bin number on the Time axis with a range of $1 \leq$time≤ 15 in one event frame. Each bin has a time window of 25ns.
- Q: ADC count per strip per time.
- Q_{max}: Maximum Q among 15 time samples in each strip. This is defined as the strip charge.

Figure 5.7 shows a two-dimensional event display for a muon track, where horizontal axis is "Strip" and the vertical axis is "ADC count". Signals can be seen clearly on consecutive 4 strips. When one particle passes the detector and generates primary electrons, these primary electrons fall on the multiple strips depending on the incident angle and the drift gap. For example, 2-5 strips will have hits by a normal incident track into a drift gap of 5mm. Therefore, adjacent hit strips are merged into one cluster. The number of clusters corresponds to the number of incident particles. The parameters of the cluster are following.

- cluster charge: Sum of Q_{max} in one cluster ($\sum Q_{max}$).
- cluster position: Defined as the charge-weighted centroid by the following formula;

$$\text{Cluster position} = \frac{\sum((strip) \times Q_{max})}{\sum Q_{max}} \tag{5.1}$$

  This matches the position of the particle if it enters perpendicular to the detector.

Figure 5.8 and Figure 5.9 show the two-dimensional distributions of cluster position for the muon beam with Ar/CO_2 and Ar/C_2H_6, respectively. The difference of hit distributions between two gases were due to the position of the chamber frame, which were moved when gases were changed. As for RC41, there is an empty area indicated as "no HV", where the voltage was not applied. Also, there are several empty lines along anode strips. They were caused by failures of the electrical connection between DLC resistors and anode strips. Since these areas affect the detection efficiency and position resolution, they were removed in the analysis.

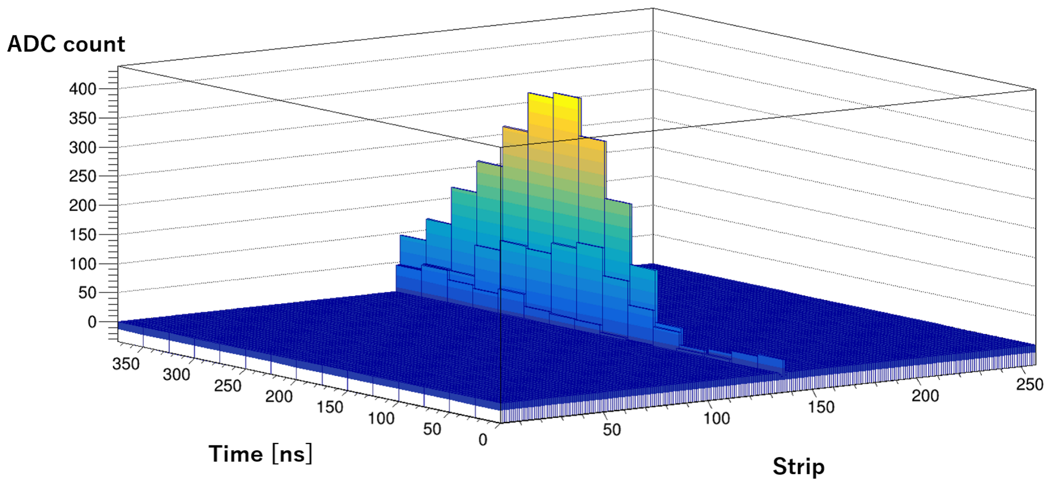

Figure 5.6: Three dimensional event display of a typical muon event on the μ-PIC.

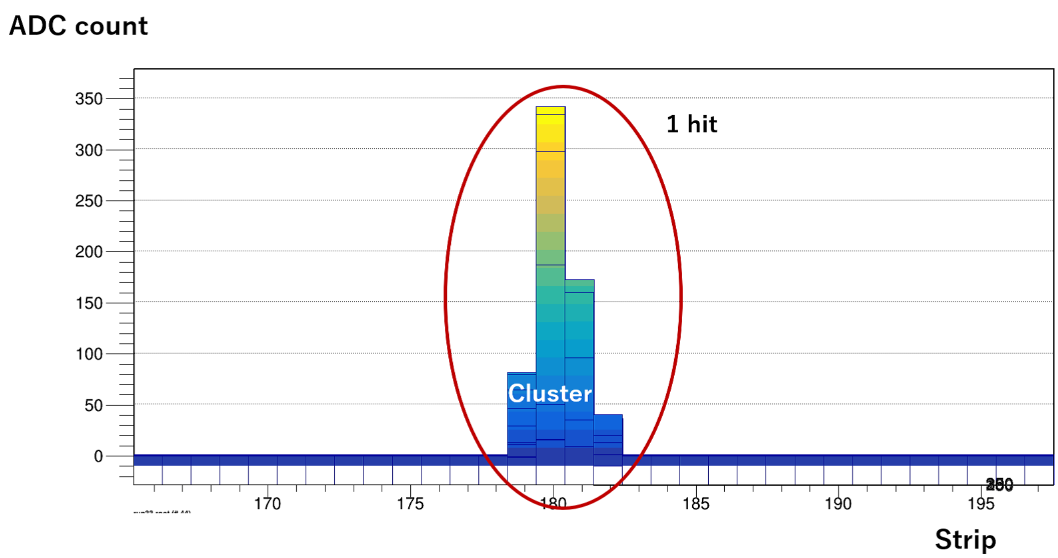

Figure 5.7: Two-dimensional event display. The horizontal axis is the "Strip" and the vertical axis is the "ADC count".

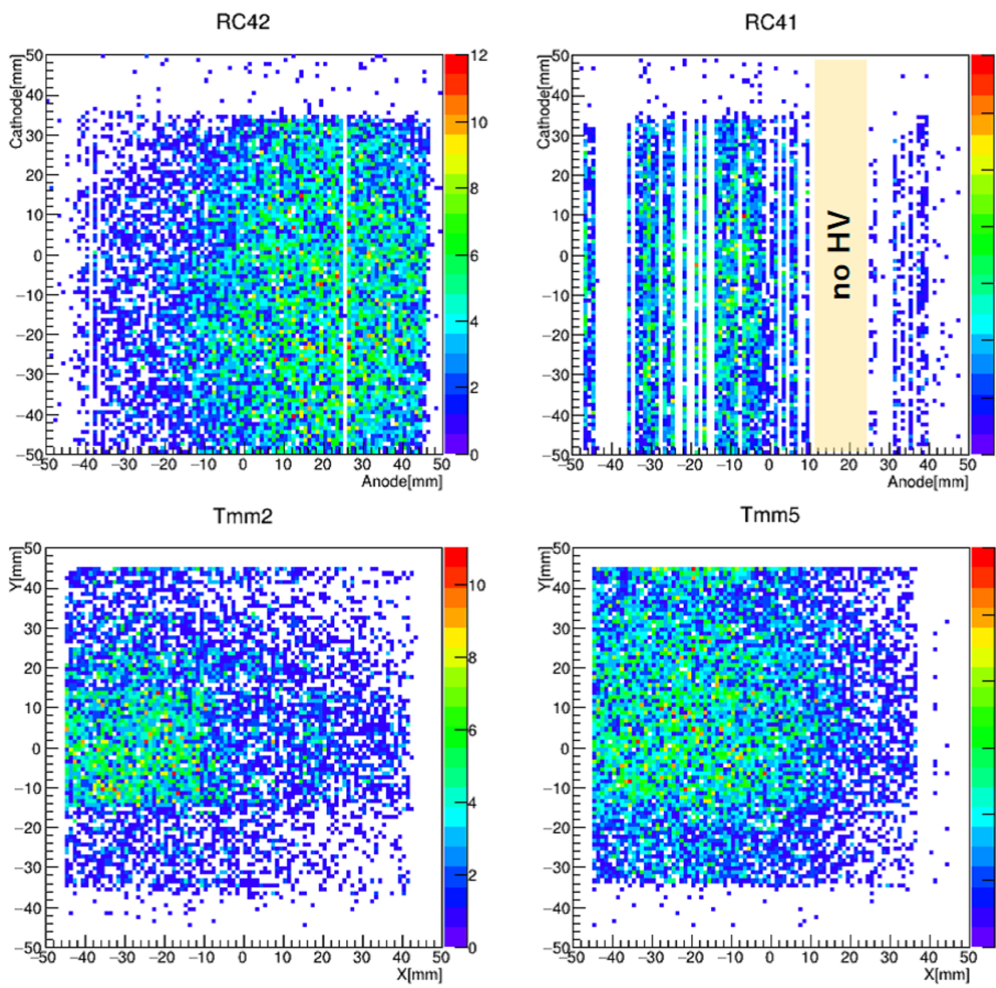

Figure 5.8: Two-dimensional hit distribution of the muon beam for Ar/CO_2.

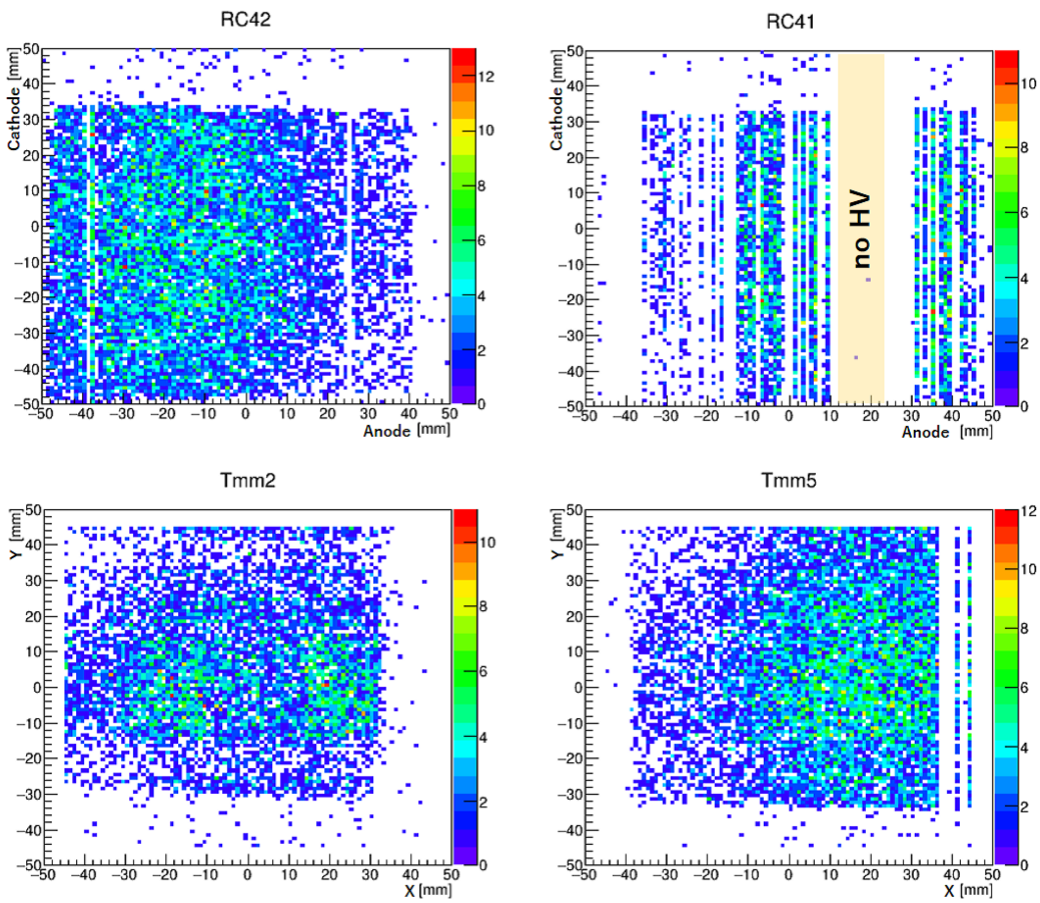

Figure 5.9: Two-dimensional hit distribution of the muon beam for Ar/C_2H_6.

5.4 Results of the test

5.4.1 Detection efficiency

The detection efficiencies of the μ-PIC has been measured for RC42. The detection efficiency was defined by the following equation.

$$\text{Detection efficiency} = \frac{N_{both}}{N_{Tmm}} \tag{5.2}$$

Here,

- N_{Tmm}: The number of events in which there are one cluster on each of two Tmm chambers
- N_{both}: The number of events in which there is at least one cluster within 5mm from the interpolated hit position by two Tmm chambers.

There were cases in which false tracks were included in N_{Tmm}, and those events were removed. Figure 5.10 shows the residual distributions of the hit position of two Tmm chambers. Here, X coordinate is parallel to resistive strips of the Tmm and Y coordinate is perpendicular to them. When the residual was within 5mm from the mean value obtained from the gaussian fit, that event was selected.

Figure 5.11 shows the detection efficiency of RC42 as a function of the amplification voltage for Ar/CO_2 (93:7) and Ar/C_2H_6 (7:3) gas mixtures. The detection area of about 8cm $\times$ 8cm, which is equal to the cross-section of the muons beam, was used for these results (see also Figure 5.85.9). At enough amplification voltages, the detection efficiencies of both coordinates were more than 98% for Ar/CO_2 (93:7) and more than 99% for Ar/C_2H_6 (7:3). These results showed that the μ-PIC can detect charged particles at a large detection area.

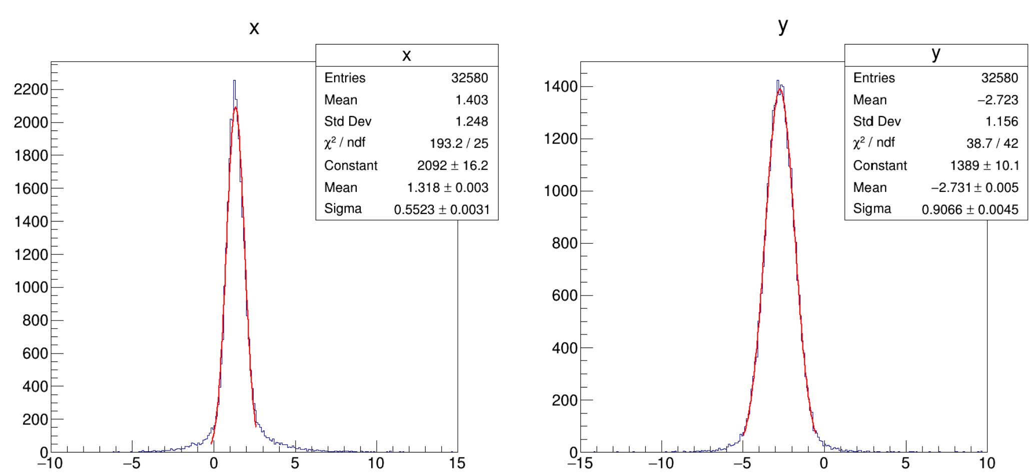

Figure 5.10: Residual distributions of the hit position of two Tmm chambers. X coordinate is parallel to resistive strips of the Tmm and Y coordinate is perpendicular to them.

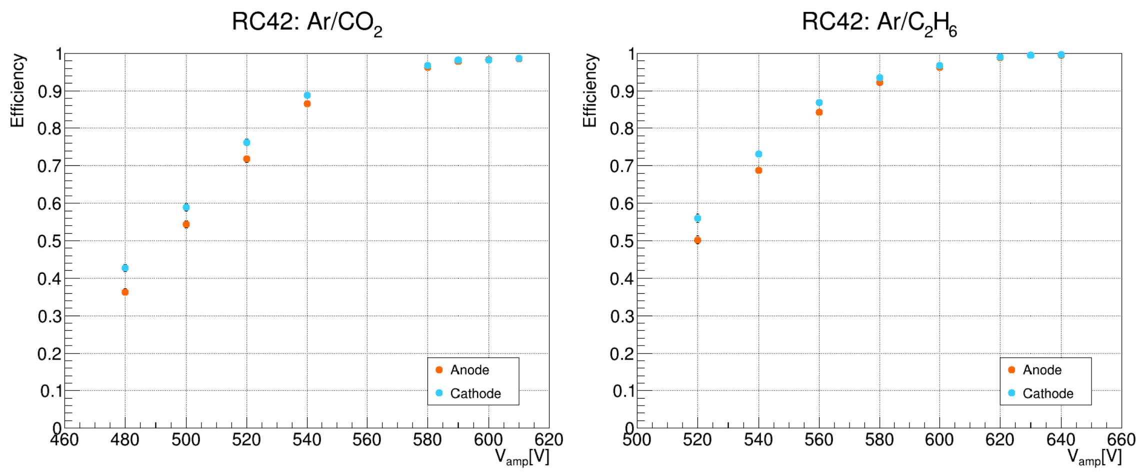

Figure 5.11: Detection efficiency of RC42 as a function of the amplification voltage for Ar/CO_2 and Ar/C_2H_6 (7:3) gas mixtures.

5.4.2 Time resolution

Since signals are sampled at a frequency of 40MHz, there is a time jitter of ±12.5ns. In order to remove the effect of the time jitter, the time resolution has been measured by using the difference of the hit time between two chambers, which were set back-to-back with each other. Figure 5.12 shows a two-dimensional event display of RC42 for a muon track, where the horizontal axis is "Time [ns]" and the vertical axis is "ADC count". In order to determine the hit time of the cluster, the hit time of each strip in the cluster was calculated by charge-centroid for time bins those exceeded 10% of Q_{max}. The equation is following.

$$\text{Hit time} = \frac{\sum((time) \times Q)}{\sum Q} \tag{5.3}$$

where, *time* is the time bin number and Q is "Q" for corresponding time bin. The hit time of the cluster was defined as the earliest hit time in the cluster. When the strip signal is too small, the signal shape is deformed, then the time resolution becomes worse. Therefore, when the Q_{max} is lower than a threshold, the strip was removed. The threshold was set to 200 when the amplification voltage is more than 580V for Ar/CO_2 and more than 600V for Ar/C_2H_6. The threshold was set to 100 for lower voltages.

Figure 5.13 shows a distribution for the time difference between two chambers with gausian fit. Assuming that the two chambers have the same resolution, the time resolution is given by dividing σ by $\sqrt{2}$. Figure 5.14 shows plots of the time resolution as a function of the amplification voltage. At enough amplification voltages, time resolutions were between 13.5-16ns. There is no significant difference between readout coordinates, and gases. It should be noted that the measured time resolution depends on the configuration of the electronics and the method to determining the hit-time. The expected time resolution in this setup is 10-15ns, and it is consistent with results.

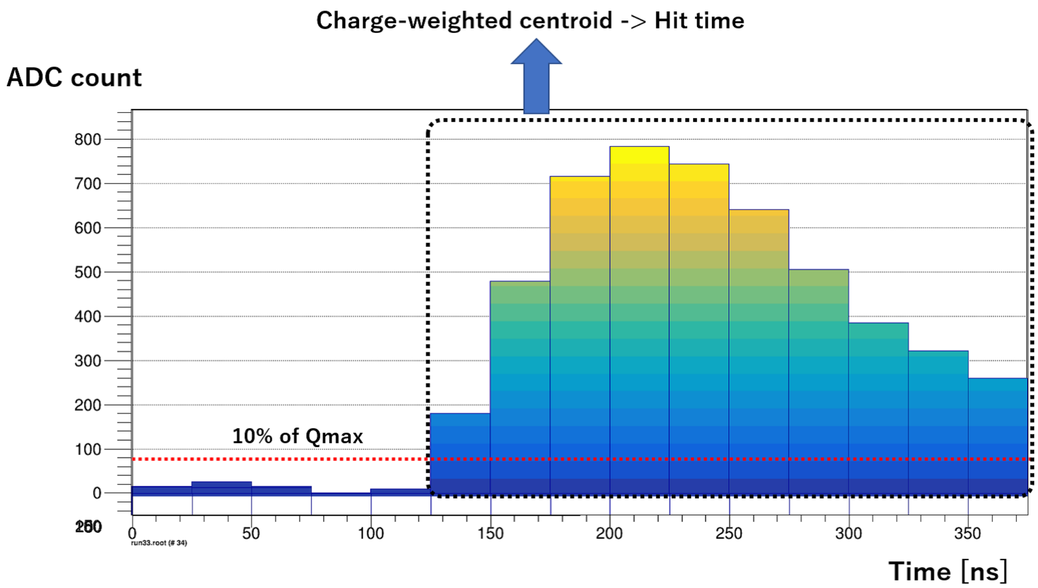

Figure 5.12: Two-dimensional event display for a muon track, where the horizontal axis is "Time [ns]" and the vertical axis is "ADC count".

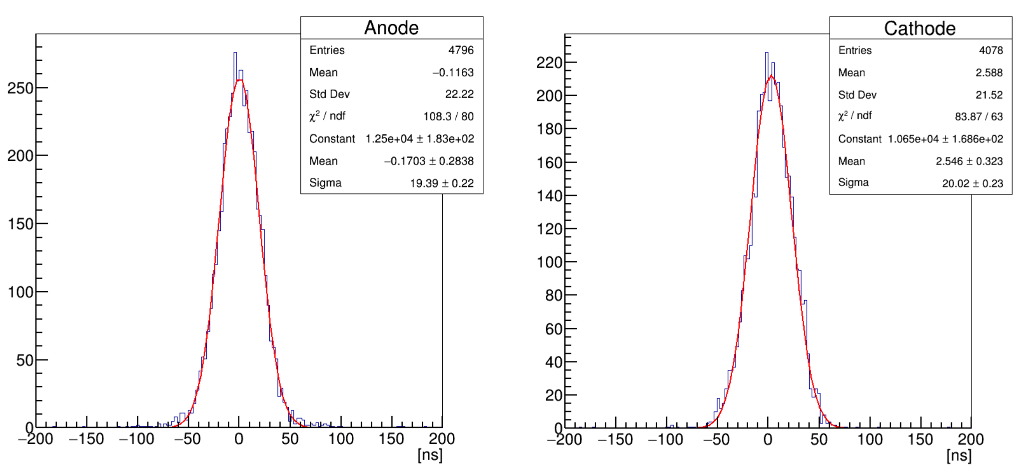

Figure 5.13: Distribution for the time difference between RC41 and RC42.

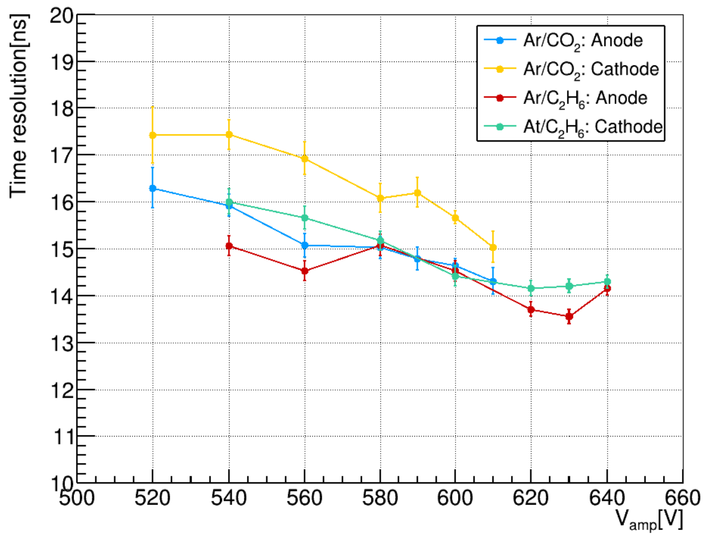

Figure 5.14: Plots of the time resolution as a function of the amplification voltage.

5.4.3 Position resolution

The position resolution of RC41 and RC42 has been measured by using the difference of the hit position between two chambers, which were set back-to-back with each other. Figure 5.15 shows a distribution of that with gaussian fit. In order to remove the contribution from dead strips on RC41, resolutions were measured at limited areas for the anode. As for the cathode, resolutions were measured at almost whole area. As in the case of the time resolution measurements, the position resolution is given by dividing σ by $\sqrt{2}$. Figure 5.16 shows the plots of the obtained position resolutions as a function of the amplification voltage. Almost all of plots are between 80-100μm for both coordinates and both gases.

Also, the position resolution of RC37 and RC42 has been measured by using two Tmm chambers as the reference. It was measured from the residual between hit position on the μ-PIC and the interpolated position by using two Tmm chambers. The residual are defined by the following equation.

$$\Delta X = X_{\mu PIC} - \frac{bX_{Tmm2} + aX_{Tmm5}}{a+b} \tag{5.4}$$

Here,

- $\mathrm{X_{\mu PIC}, X_{Tmm2}, X_{Tmm5}}$: Hit position of each chamber (see Figure 5.17).
- a: Distance between Tmm2 and μ-PIC.
- b: Distance between Tmm5 and μ-PIC.
- ΔX: Residual.

The direction of the anode and cathode coordinates of the μ-PIC are parallel to X and Y of the Tmm, respectively. However, directions of three chambers (two Tmms and one μ-PIC) were not aligned perfectly. Therefore, alignments were corrected. Figure 5.18 shows the residual distribution obtained from the anode coordinate against the hit position for cathode coordinate of RC42. Left shows that before alignment correction. Residual distributions differ depending on cathode positions. Right shows that after alignment correction. Precise resolution could be measured by this correction.

Figure 5.19 shows a distribution of the residual with gaussian fit. Assuming that two Tmm chambers have the same resolution (σ_{Tmm}), the position resolution of the μ-PIC ($\sigma_{\mu\mathrm{PIC}}$) is given by the following equation.

$$\sigma^2_{\mu PIC} = \sigma^2_{residual} - \frac{a^2+b^2}{(a+b)^2}\sigma^2_{Tmm} \tag{5.5}$$

From the previous study of the two-dimensional Micromegas, it is known that the position resolutions of the Tmm are 56μm for the X coordinate and 55μm for the Y coordinate [41].

Figure 5.20 shows the position resolution of RC37 and RC42 as a function of the amplification voltage. As for RC37, position resolutions have large variation due to less statistics. Also, resolutions are a little worse than those of RC42. However, all plots were better than 100μm. As for RC42, resolutions were better than those shown in Figure 5.16. In the former method, the position resolution is affected by small angular variation of the particle track. It is assumed that this effect were reduced by using the interpolated position from two reference chambers.

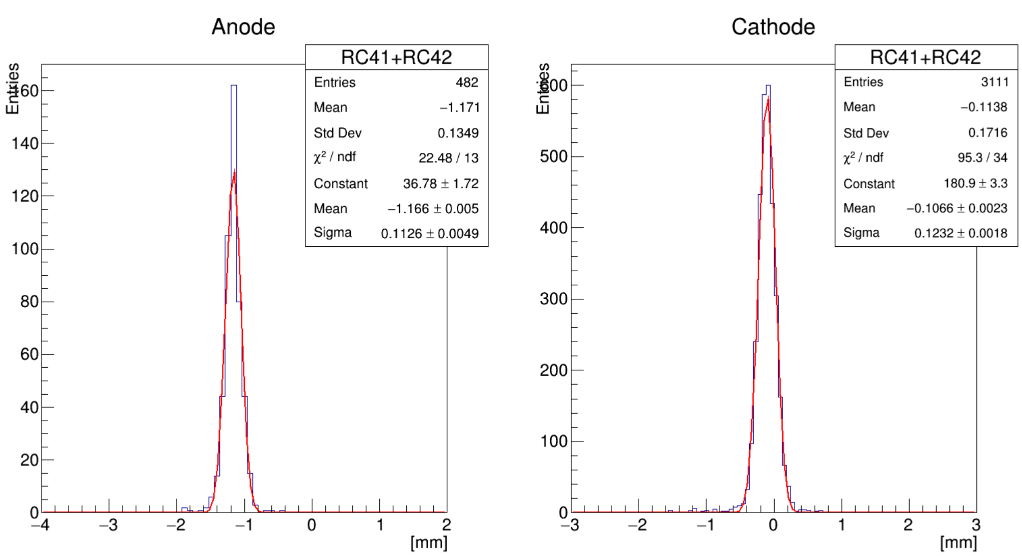

Figure 5.15: Distribution of the difference of the hit position between two chambers with gaussian fit.

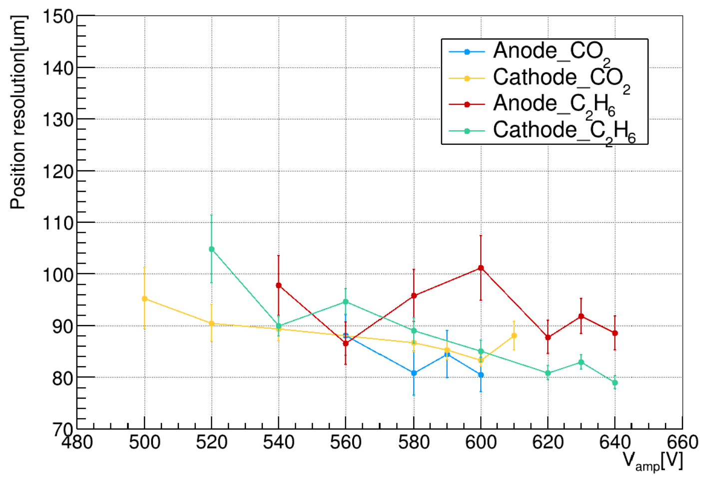

Figure 5.16: Plots of the position resolution as a function of the amplification voltage.

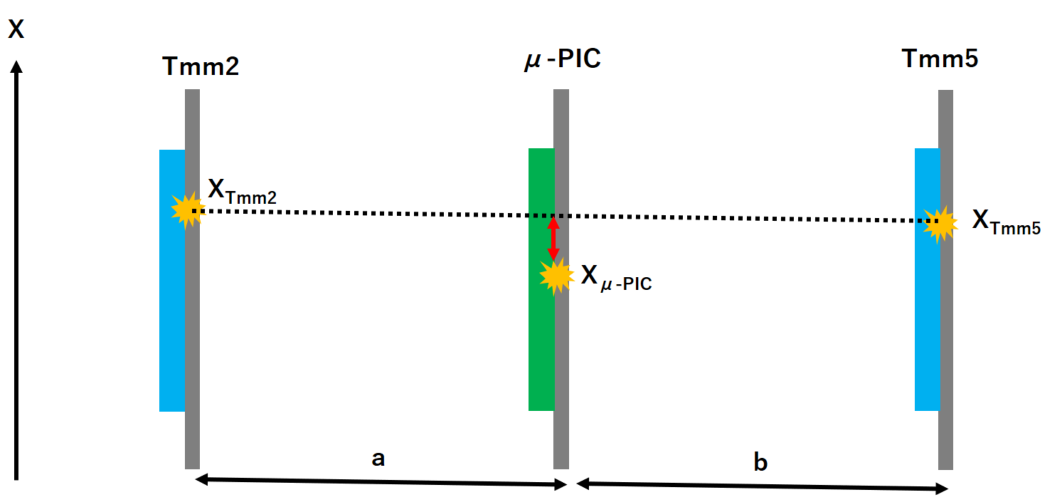

Figure 5.17: Schematic view of one μ-PIC and two Tmm chambers.

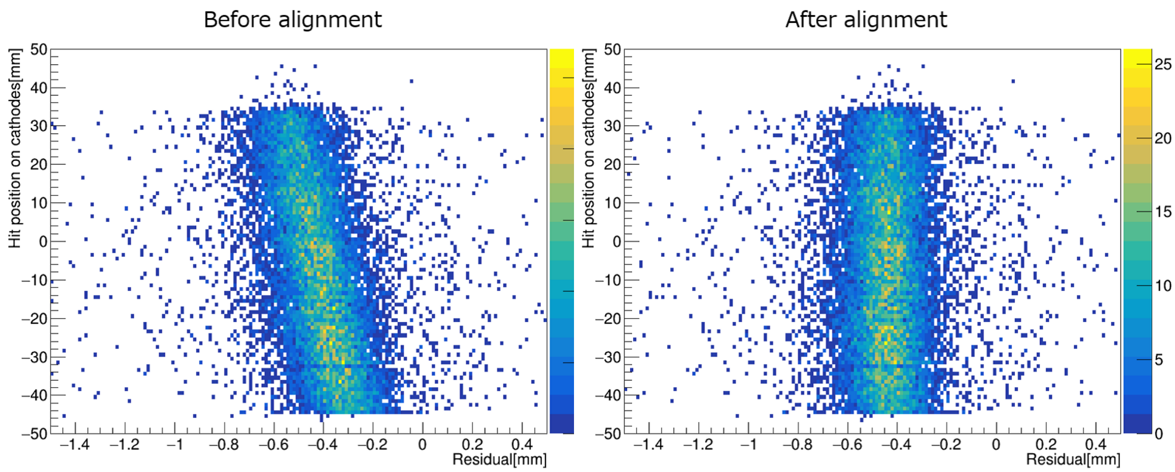

Figure 5.18: Residual distribution obtained from the anode coordinate against the hit position for cathode coordinate of RC42. Left: before alignment correction. Right: after alignment correction.

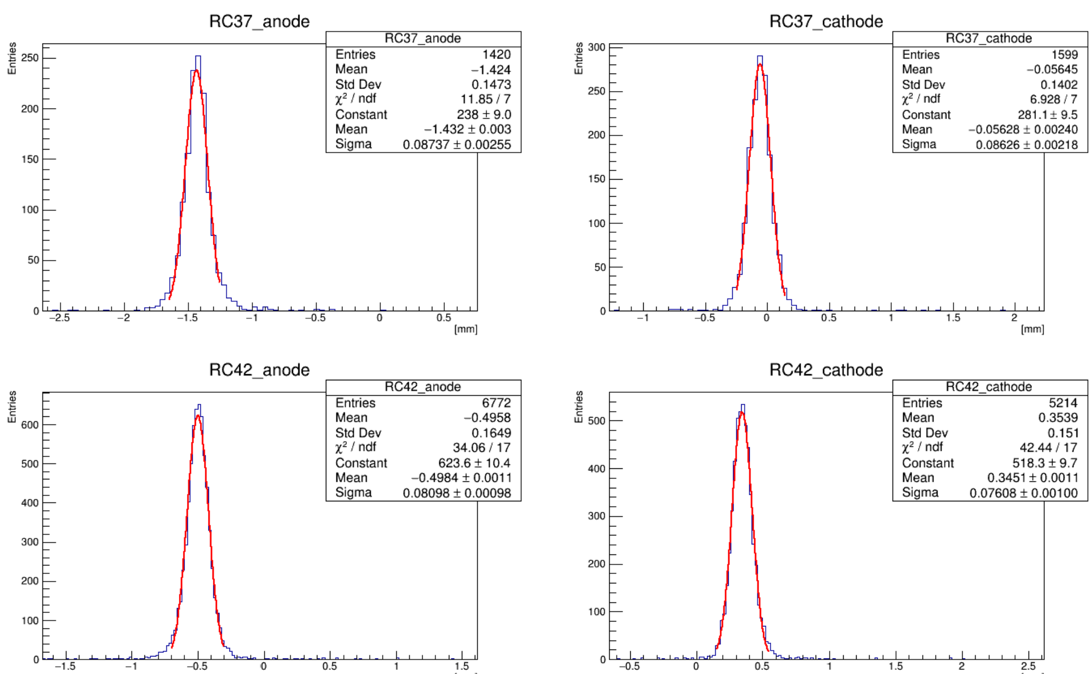

Figure 5.19: Residual distribution of RC37 and RC42 for both coordinates.

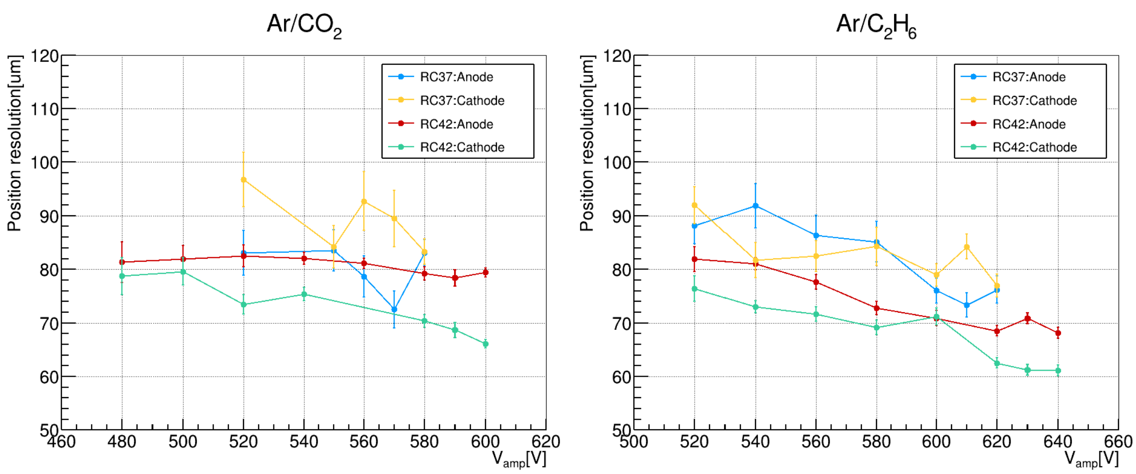

Figure 5.20: Position resolution measured by using interpolated position from two Tmms. Left is of Ar/CO_2 and right is of Ar/C_2H_6.

Chapter 6

Performance study under the fast neutrons irradiation

6.1 Experimental setup

The resistive μ-PIC was designed for a charged particle detector in the harsh background of heavily ionizing particles. As described in section 2.4, in the hadron collision experiment, atomic nuclei of the chamber materials and gas atoms are recoiled by fast neutrons. Those nuclei ionize gas atoms heavily, and huge charges of $\sim 10^{4-5}$ electrons are deposited in the gas volume. When the detector is operated with a gas gain of several thousands, the electrons density exceeds the Raether limit ($\sim 10^{6-7}$), and large sparks are easily occurred. In order to evaluate the detector performance, the μ-PIC was operated in the intense fast neutrons environment.

The test was performed in July 2017 at the tandem electrostatic accelerator facility in Faculty of Maritime Science, Kobe University (Figure 6.1). In this facility, fast neutrons with a few MeV can be produced by $^{9}\mathrm{Be}(\mathrm{d},\mathrm{n})^{10}\mathrm{B}$ reaction. Figure 6.2 shows the schematic drawing of the accelerating system. The negative ions of deuteron are generated from the cesium sputtering negative ion source and carried to the accelerator, where the terminal HV is set to +1.5MV. They are accelerated toward the terminal, and converted into positive ions by a electron stripping reaction in N_2 gases. They are re-accelerated to 3MeV toward the end of the accelerator, where the potential is set to the ground. An 1 mm thick Be target (see Figure 6.3) is set at the end of the deuteron beam. The Be target is isolated from ground, and connected to a current monitor to measure the beam current. A bias voltage of several tens volts is applied on the Be target for suppressing secondary electrons emitted from the target in order to measure the beam current accurately (see Figure 6.4). Taking the beam current and the irradiation time, the total amount of accumulated charges are calculated. This value determines the neutron yield, and it is estimated to be $2 \times 10^{9}\mathrm{n}/\mu\mathrm{C}$ with the deuteron energy of 3MeV [42]. This is an experimental value, and the condition of this test is not as same as previous studies. Therefore, it was assumed that the neutron yield had a range of $\pm 50\%$.

The μ-PIC was placed in front of the Be target. The distance between the detector surface and the target was set to 4, 10, 30, 60cm depending on the required neutron flux. The flux of neutrons was also controlled by varying the deuteron beam intensity from 20nA to 1000nA. The total amount of irradiated neutrons was calculated as following.

$$N = 2 \times 10^9[\mathrm{n}/\mu\mathrm{C}] \times I[\mu\mathrm{A}] \times T[\mathrm{s}] \times \frac{S}{4\pi d^2} \tag{6.1}$$

Here, I is the beam current on the Be target, T is the irradiation time, S is the operated area on the chamber, and d is the distance between the Be target and the chamber. Since the detection area of the μ-PIC is 10 $\times$10cm^2, d differs depending on the position in the chamber. Especially, when the chamber is put at short distances from the Be target, the difference of d becomes large. Therefore, it was treated as a systematic error in this test.

RC37 and RC38 (see Table4.1) were operated in this condition. The drift field was set to 3kV with a drift gap of 3mm. Ar/C_2H_6 (9:1) gas mixture was used. The anode current was recorded using an USB digital oscilloscope (UDS-1G02S-HR) in order to observe and record sparks. Figure 6.6 shows a recorded current monitor on the anode. A base current is constantly yielded on the electrode during the fast neutrons irradiation (blue line in Figure 6.6). When a spark is occurred, a large current more than 1μA flows momentarily. When the anode current exceeded a threshold, it was counted as a spark. The current threshold was set to 1μA and 2μA against the base current.

Figure 6.1: Tandem electrostatic accelerator in Faculty of Maritime Science, Kobe University.

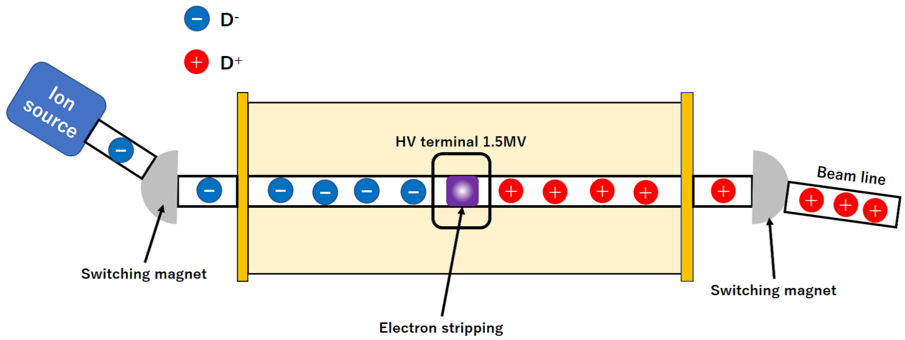

Figure 6.2: Schematic drawing of the accelerating system.

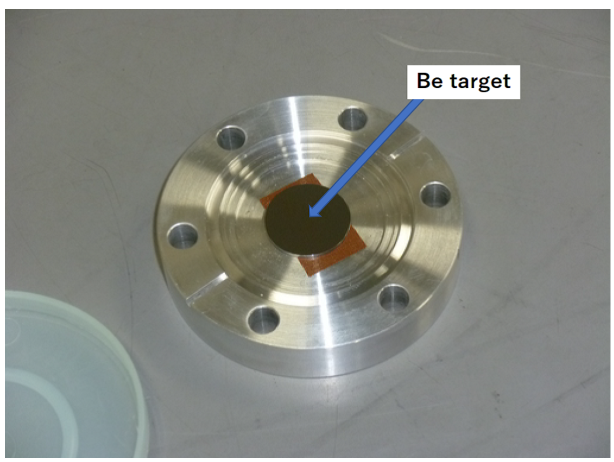

Figure 6.3: Photograph of the Be target.

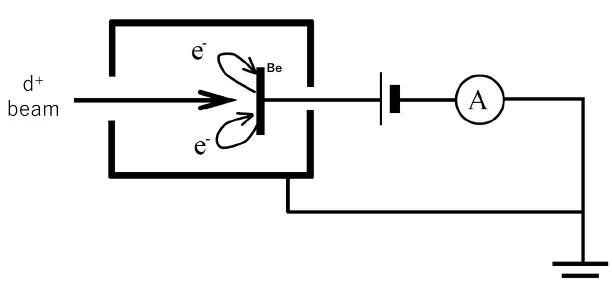

Figure 6.4: Schematic view of the target assembly.

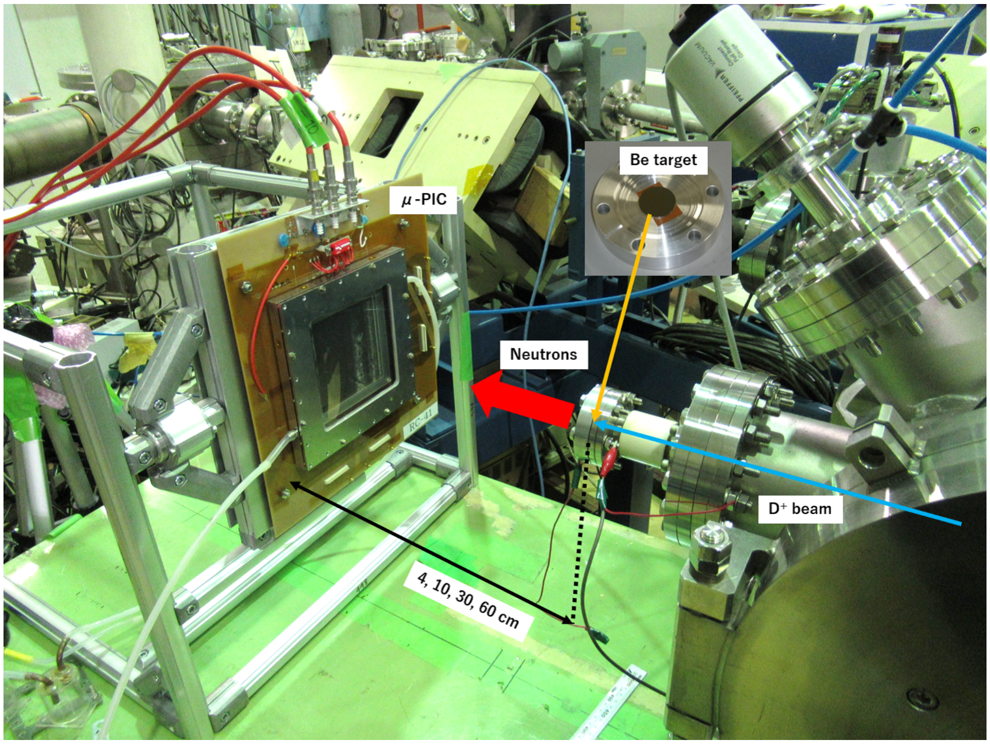

Figure 6.5: Experimental setup.

6.2 Results of neutron tests

6.2.1 Spark rate

The spark rate was defined as the ratio of sparks counts to the total amount of irradiated neutrons on the chamber. The spark rate of μ-PICs are plotted in Figure 6.7 with the current threshold of 2μA. Here, RC37 and RC38 are the new μ-PICs. RC27 and RC28 are the former resistive μ-PICs, in which carbon polyimide paste was used for resistive cathodes (see section 3.2). "Normal" means the original μ-PIC without resistive cathodes. The spark rate of RC37 is consistent with that of the previous result above the gas gain of 8000, and 10^{3-5} times lower than that of the conventional μ-PIC. The spark rate of RC38 is 10^{1-2} times higher than that of RC37 above the gas gain of 8000. Various reasons can be considered for differences of results. One is the operated area of chambers. In the previous study, the it was only 0.64×10.24 cm^2. The operated area of RC37 was 4-6 times larger and that of RC38 was 6-8 times larger than that of the previous study. The others are individual differences of chambers and conditions in the operation. In this test, these effects could not been evaluated. Figure 6.8 shows the spark rate of the new chambers using different current thresholds of 1μA and 2μA. The spark rate with a threshold of 1μA is about ten times higher than that of 2μA. This means that almost all of sparks are suppressed below 1μA, and this result is consistent with the previous one (see section 3.2). These result show that large sparks are strongly suppressed by the μ-PIC with the new structure and the DLC electrode.

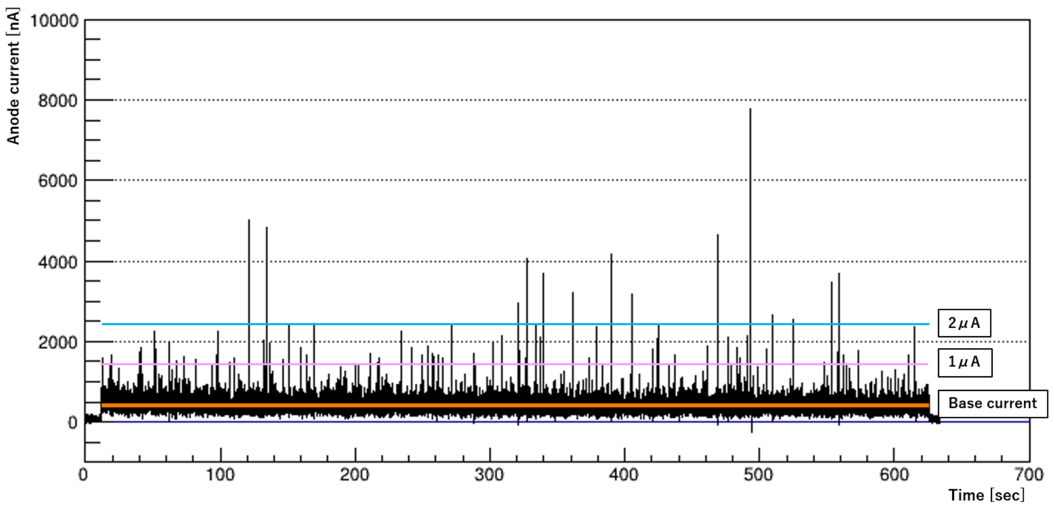

Figure 6.6: Current monitor on the anode of RC37 under the neutrons irradiation recorded for 10 minutes. The gas gain is ∼2000.

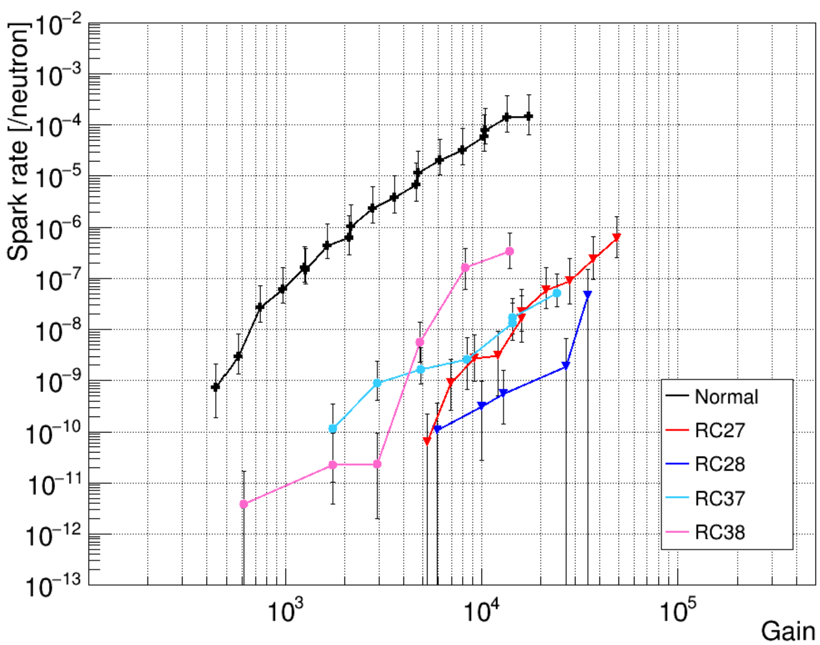

Figure 6.7: Spark rate of μ-PICs. RC37 and RC38 are the new μ-PICs. RC27 and RC28 are the former resistive μ-PICs. "Normal" means the original μ-PIC without resistive cathodes.

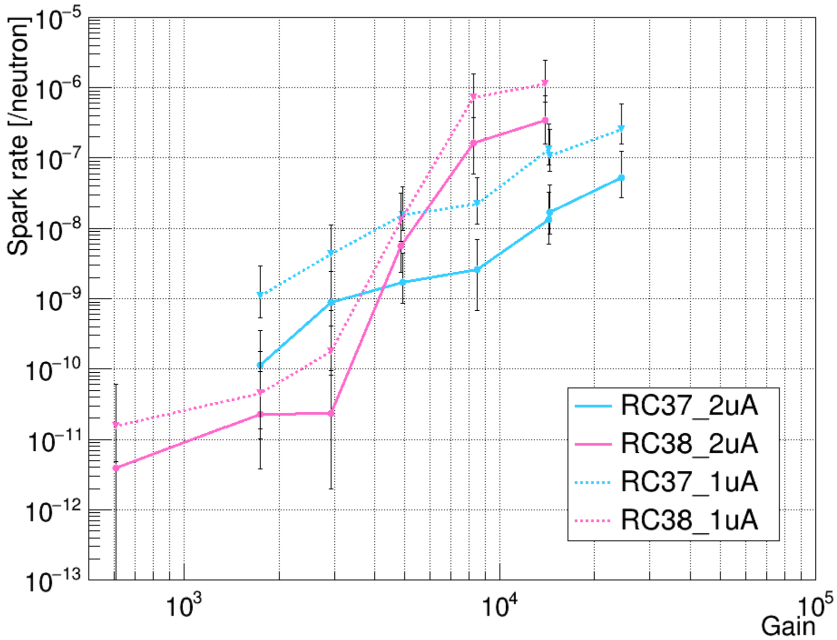

Figure 6.8: Spark rate of new μ-PICs with current thresholds of 1μA and 2μA.

6.2.2 Base current on the electrode

The important thing to consider other than the spark rate is that how much the voltage drop is on the resistive electrodes under the high radiation condition. The voltage drop means the gain drop which may make the detection efficiency worse. This has been evaluated using the base current on the electrodes under the neutrons irradiation (see Figure 6.6). The surface resistivity of the cathodes is $\sim$180kΩ/sq. The operated area was 2.56×10.24 cm^2. Figure 6.9 shows plots of the base current [nA/cm^2] as a function of the amplification voltage under the neutrons flux of $60 - 250$kHz/cm^2. The current of the Be target was normalized with 1μA. The base current increases linearly up to the gas gain of $\sim$20000. This means that the gain was not dropped, and the μ-PIC can be operated under the fast neutrons flux of around 100kHz/cm^2. Figure 6.10 shows results in which the neutrons flux is $1 - 4$MHz/cm^2. In this case, the base current decreases at 580V. However, it increases linearly up to 560V in which the gas gain is around 5000. It is enough value to detect minimum ionizing particles with high detection efficiency. If the fast neutrons flux becomes higher, it might be difficult to keep enough gains. In that case, the cathode surface resistivity should be reduced less than 180kΩ/sq.

6.2.3 Duration and occupied region of the spark

The duration time of the spark has been measured using the recorded current data of high voltage on anodes. The current data was recorded with a sampling rate of 5ms. The time during which the current exceeded the threshold (1μA or 2μA) was

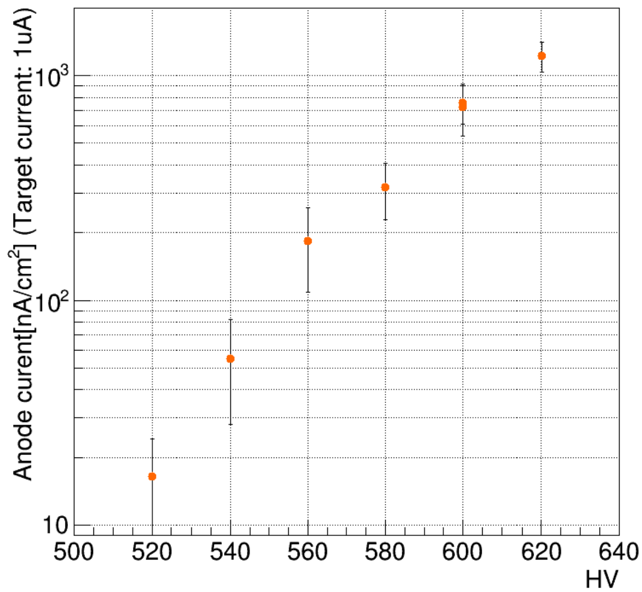

Figure 6.9: Plots of the base current [nA/cm^2] as a function of the amplification voltage. The current of the Be target was normalized with 1μA. The neutrons flux was estimated to be $60 - 250$kHz/cm^2. Any gain drops have been observed.

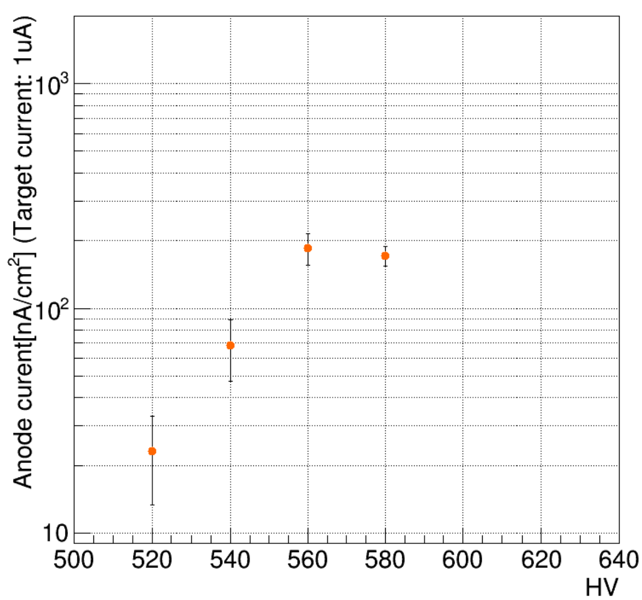

Figure 6.10: Plots of the base current [nA/cm^2] as a function of the amplification voltage. The current of the Be target was normalized with 1μA. The neutrons flux was estimated to be $1 - 4$MHz/cm^2. The base current increases linearly up to 560V in which the gas gain is around 5000.

measured for each spark. Figure 6.11 shows the histogram of duration time of the spark. For both thresholds, almost sparks have the duration time less than 50ms, and no sparks have that of more than 100ms. This duration time is correspond to the dead time of the detector.

Figure 6.12 shows an event display on the anode obtained by the SRS (see section 5.2). The horizontal axis is the strip number and the vertical axis is time which has a window of 675ns. Two front-end readout cards (APV25) were set for covering 256 readout strips. There are two types of the signal found, one is a typical neutron event between 220-230 strips and the other is a spark which covers 1-128ch. It can be seen that when a spark is occurred, it affects all strips belonging to the same readout card.

From those results, it can be estimated that when a spark is occurred, a dead time below 100ms is caused at 128 strips, in which it is assumed that 128ch readout card are used for the same front-end.

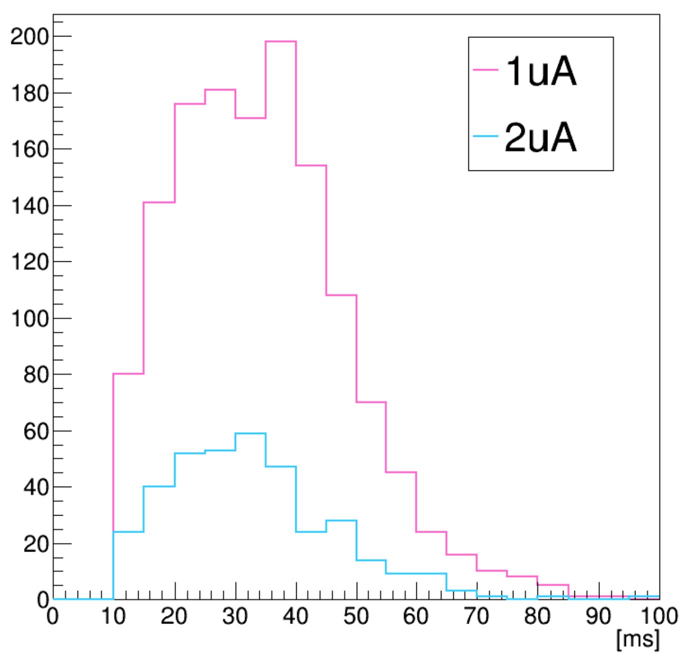

Figure 6.11: Duration time of the spark with current thresholds of 1μA and 2μA.

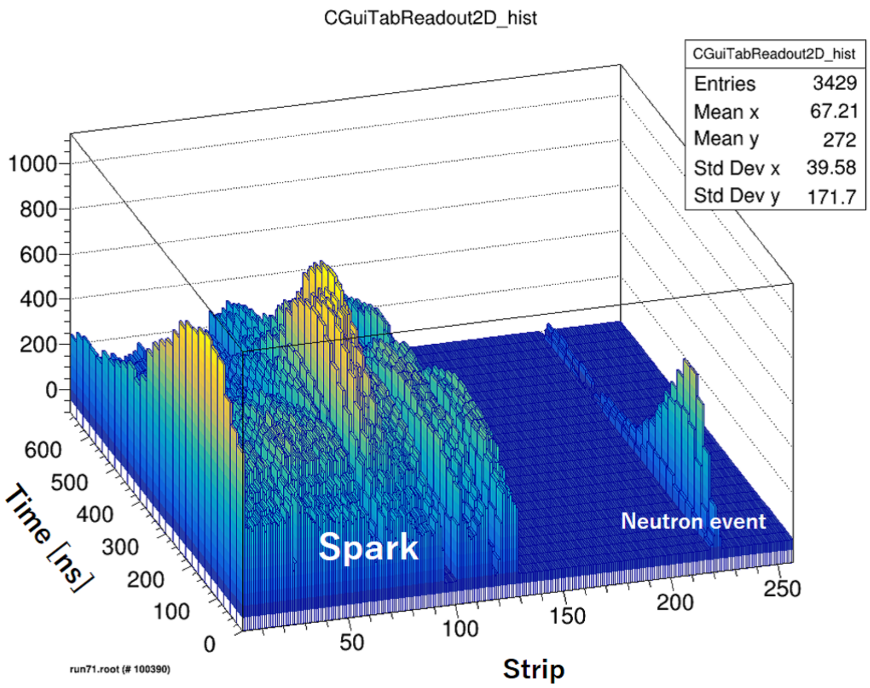

Figure 6.12: Event display of one event.

Chapter 7

Sammary and conclusion

The μ-PIC with resistive electrodes have been developed for high-rate applications. The μ-PIC is one of the Micro Pattern Gaseous Detector (MPGD), and fabricated based on the PCB (Print Circuit Board) technique. By adding the resistive layer, the μ-PIC has great tolerance to sparks. However, there remained problems in the detector design and resistive electrodes.

A novel design of the resistive μ-PIC has been proposed. By using photolithography instead of laser drilling, anode and cathode electrodes were well aligned at whole detection area of 10×10 cm^2. DLC thin film made by carbon sputtering technique was used for resistive electrodes instead of carbon-loaded paste. This novel technique enabled flexible configuration of the resistivity at high uniformity. The resistivity can be controlled flexibly and high uniformity is realized. Resistors for HV bias and capacitors for AC coupling were completely removed by applying PCB and carbon sputtering techniques. Those ideas made the μ-PIC a robust and very compact detector in which fine two-dimensional position measurement can be performed.

The performances of the new resistive μ-PIC has been measured by various ways. With ^{55}Fe 5.9keV X-rays source, the gas gain of more than 10^4 was attained. The uniformity of the gain was within 30% in whole detection area. It is expected that the μ-PIC has capability to detect minimum ionizing particles with high detection efficiency in the entire detection area of 10×10cm^2. The high-rate capability has been evaluated using intense X-rays. The μ-PIC could be operated stably under the intense X-rays up to 13MHz/cm^2. Two-dimensional X-ray images were taken, and fine structures of 1mm size were clearly seen. Performances for charged particles have been measured using 150GeV/c muons beam at SPS/H4 beam line in CERN. The detection efficiency was more than 98%. The time resolution was 13-16ns. The position resolution was 60-90μm. In order to evaluate tolerance to sparks, the fast neutrons irradiation test has been performed at the tandem electrostatic accelerator in Kobe University Faculty of Maritime Science. The spark rate was almost similar to the previous result of our former resistive μ-PICs. It is $\sim 10^{-8}$/neutron for the gas gain of 5000. Also, it has been found that when the surface resistivity of the cathode is $\sim$180kΩ/sq., the μ-PIC can be operated with the gas gain of 5000 under the fast neutrons flux of up to $1 - 4$MHz/cm^2 without no gain reduction.

Thus the novel design of the resistive μ-PIC has been established, and performance studies have showed that it is a promising detector for future high-rate applications.

Acknowledgements

I would like to express my great gratitude to Prof. Atsuhiko Ochi. Development of the resistive μ-PIC was started from his magnificent idea. A lot of efforts made by him and his past students have made enormous contributions to this thesis. I would also like to express my great gratitude to Prof. Hisaya Kurashige who gave me great numbers of advices for this thesis. This thesis would not be completed without his kind guidance. I specially thank Hideo Uehara at Raytech Inc. Production of our μ-PIC is realized by his great support. I also thank Itaru Nakawatase and Raytech-'s staffs who concerned our μ-PIC. I would thank Prof. Yuichi Furuyama, Prof. Akira Taniike, Mr. Yokose and Ms. Komiyama. I could obtain many data of good quality with their cooperation at the Tandem accelerator facility. I've received a lot of supports by RD51 collaboration when I stayed at CERN. I am particularly grateful to Eraldo Oliveri and Givi Sekhniaidze. Thanks to them, I could conduct my research comfortably at the lab. I would also like to thank Mauro Iodice and his students for the fruitful beam time at SPS/H4.

I would like to thank MPGD researchers in Japan for their useful feedbacks and good time in conferences. I deeply thank Prof. Toru Tamagawa. I would like to thank members of the detector development group: Kohei Matayoshi, Keisuke Ogawa, Yusuke Ishitobi, Hiroaki Hasegawa, Noriko Nagasaka and Satoru Yamauchi. The CERN life with them were very nice. I would like to express my gratitude to those who concerned the QA/QC of resistive foils for the ATLAS Micromegas. Prof. Tatsuya Masubuchi always supported me for whole things about the ATLAS Micromegas. I am deeply grateful to him. Prof. Tatsuo Kawamoto provided me many informations. Dr. Yosuke Kataoka taught me various things about software. Dr. Tomoyuki Saito helped me in various situations. Masahiro Yamatani have made great efforts for the QA/QC. I am glad that I worked with him for four years. Paolo Iengo and Rui De Oliveira came to Kobe three times, and we could make good discussions about production of resistive foils. Paolo also helped me at the RD51 lab. Rui also provided me useful feedbacks for the resistive μ-PIC. Kim Heidegger and Jona Bortfeldt supported me for the management of resistive foils. I would like to thank many students who worked hard for the QA/QC: Tomohiro Yamazaki, Kotaro Kimura, Koki Maekawa, Akihiro Higashida and Takafumi Kodama from ICEPP: Kotaro Wakamiya, Kosuke Takeda, Kusuhi Horiguchi, Takayoshi Sakai, Toshiki Yoshida and Daiki Saito from Kobe. I would like to thank the NEWAGE group. Prof. Kentaro Miuchi gave me many instructions in physics experiments. I could have good discussions about experiments with Takashi Hashimoto, Tomonori Ikeda, Miki Nakazawa, Hirohisa Ishiura, Dr. Hiroshi Ito, Dr. Kiseki Nakamura, and Ryosuke Taisyaku. My appreciation goes to Yumi Yokoyama and Kazumi Yoshida for kind support on office procedures. Yumi Yokoyama supported me for five years, and I am deeply grateful to her. I would like to thank all staffs and students of Kobe Particle Physics group. Prof. Yuji Yamazaki gave me many knowledge about ATLAS experiments. Prof. Yasuo Takeuchi gave me a lecture on Geant4. Prof. Junpei Maeda told me interesting things about researches. Talks with Prof. Atsumu Suzuki was fun. I have studied physics for five years with Ryota Yakabe, Ye Chen and Makoto Hasegawa. I wish them the best of luck in their future endeavors. Takeshi Okada is one of the best friends made through "LoveLive!". Joining many events and traveling to Numazu with him and his friends were very nice. I had the enjoyable lab life with Shogo Kido, Keigo Abe, Yuki Miyabe, Yuta Isobe, Taro Sugimoto, Keita Mizukoshi, Ryo Tanioka, Rei Fujita and other staffs and students. I would like to extend my thanks to Freebeat where I could make many friends and great memories with them through music. I would like to express my special thanks in Figure 7.1. Finally, I would like to thank my family for supporting my life.

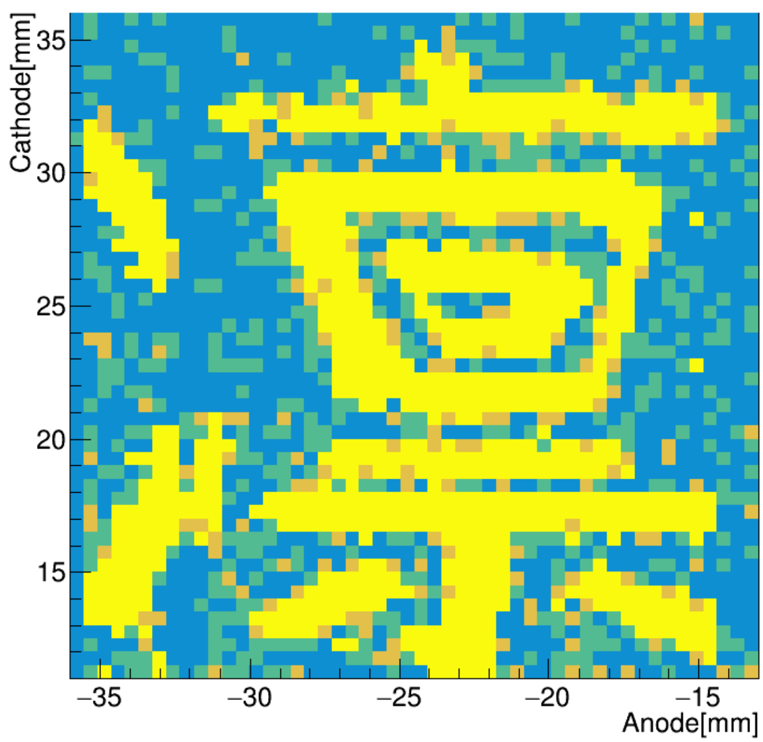

Figure 7.1: X-ray image of a Japanese School Idol's name indicated in yellow chinese character. I would like to express my great gratitude to her for the spiritual support.

Appendix A

Principle of the operation of the gas detector

A.1 Interaction between particles and materials

When a charged particle passes through the material, it losses a part of its energy by the Coulomb interaction with atoms/molecules of the material. The mean energy loss of the incident particles is expressed by the Bethe-Bloch formula as following.

$$-\frac{dE}{dx} = 4\pi r_e^2 m_e c^2 N_A z^2 \rho \frac{Z}{A}\frac{1}{\beta^2}[\ln \frac{2m_e c^2\beta^2\gamma^2}{I} - \beta^2] \tag{A.1}$$

Here,

- E: Energy loss of the incident particle
- x: Distance traveled in the material
- $\mathrm{r_e}$: Classical electron radius
- $\mathrm{m_e}$: Electron mass
- c: Speed of light
- $\mathrm{N_A}$: Avogadro's number
- z: Charge of the incident particle
- ρ: Density of the material
- Z: Atomic number of the material
- A: Atomic mass of the material
- β: Velocity in terms of the speed of light c
- γ: Lorenz factor
- I: Mean excitation energy

Figure A.1 shows the energy loss of the muon on copper as a function of the muon momentum. The Bethe-Bloch formula appears at $0.1 \leq \beta\gamma \leq 1000$. When the momentum is low ($0.1 \leq \beta\gamma \leq 1.0$), the stopping power decreases in proportional to $1/\beta^2$. When the momentum is between $1.0 \leq \beta\gamma \leq 1000$, the energy loss becomes very low, and the minimum value is obtained at $\beta\gamma \approx 4$. Such a particle is called the minimum ionizing particle (MIP).

$$-\frac{1}{\rho}(\frac{dE}{dx})_{min} \approx 3.5\frac{Z}{A}\text{MeVcm}^2/\text{g} \tag{A.2}$$

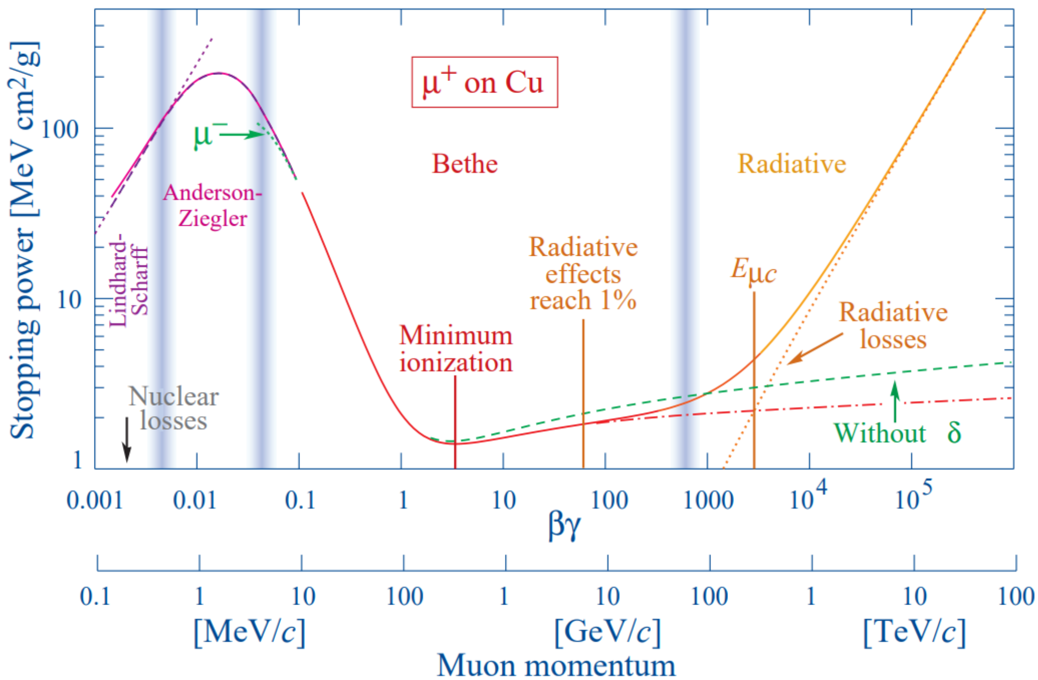

Figure A.1: Stopping power for positive muons in copper as a function of muons momentum [43].

When a charged particle passes through the gas, electron-ion pairs are released along the track of the incident particle. The total number of electron-ion pairs n_T becomes

$$n_T = \frac{\Delta E}{W_i} \tag{A.3}$$

where ΔE is the total energy loss of the incident particle in the gas volume, and W_i is a necessary energy to produce one electron-ion pair. W_i differs depending on the gas. For example, W_i of Ar is 26eV.

In the case of a photon, it interacts with gas molecules by the photoelectric absorption, the Compton scattering, or the pair production depending on its energy, and primary electrons are emitted.Those particles also generate electron-ion pairs according to above equation (A.3).

Neutrons interact with atomic nuclei of gases or materials of the detector. Fast neutrons recoil those nuclei by the elastic scattering. Thermal neutrons are absorbed by atomic nuclei.

A.2 Drift of electron-ion pairs

In order to prevent the recombination of electron-ion pairs, an electric field is applied in the gas volume. Thus, electrons and ions drift toward opposite direction, while repeating collisions with gas molecules. The drift velocity of ions (v_D^+) is experimentally known as following.

$$v_D^+ = \mu^+ E \frac{p_0}{p} \tag{A.4}$$

Here, μ^+ is the mobility of ions, E is the strength of the electric field, P_0 is the atmospheric pressure, and p is the gas pressure. The mobility of ions differs depending on the kind of gases. TableA.1 shows examples of the mobility of ions.

Gas	Ion	μ [$cm^2V^{-1}s^{-1}$]
He	He^+	10.4
Ne	Ne^+	4.7
Ar	Ar^+	1.54
Ar	CH_4^+	1.87
Ar	CO_2^+	1.72
CH_4	CH_4^+	2.26
CO_2	CO_2^+	1.09

Table A.1: Mobility of ions for some kinds of gases [44].

Since the mean free path of electrons is much longer than that of ions, electrons obtain a large energy between each collision with gas molecules. Especially, the wave length of electrons around 1eV is correspond to two times the orbital diameter of the bound electrons of the noble gas. By a quantum effect, the gas atom becomes almost transparent for electrons. FigureA.2 shows the scattering cross section of electrons on Ar gas atoms as a function of electrons energy. The cross section has a minimum value, and this effect is called the Ramsauer effect. Therefore, the drift velocity of electrons cannot be explained simply like that of ions, and that can be obtained from experimental results or simulations. FigureA.3 shows the drift velocity of electrons in some kinds of gases as a function of the drift field at standard conditions. The drift velocity of electrons is an order of 1cm/μs, and this is ~1000 times larger than that of ions.

A.3 Gas multiplication

When the strength of the electric field is more than ~10kV/cm, electrons obtain an enough energy to ionize gas molecules, and secondary electrons are emitted.

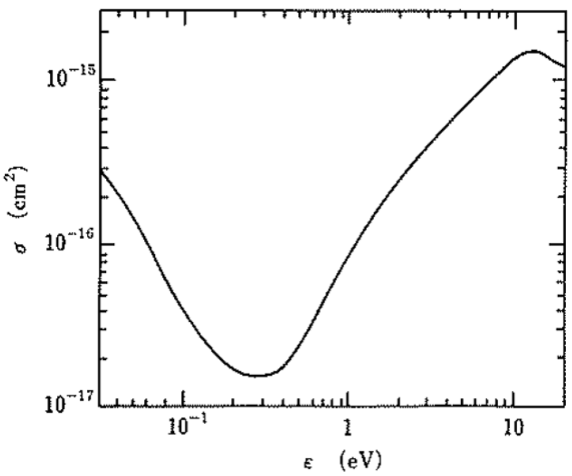

Figure A.2: Scattering cross section of electrons on Ar gas atoms as a function of electrons energy [45].

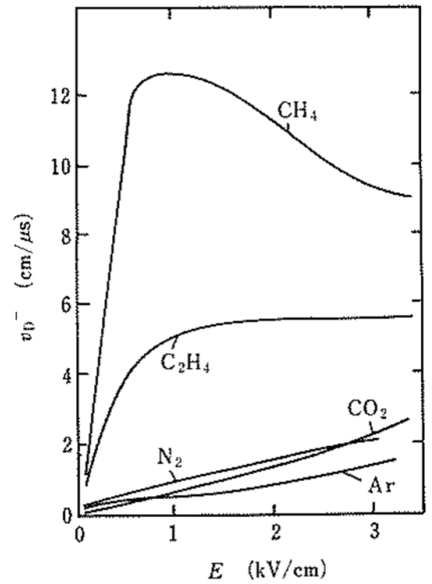

Figure A.3: Drift velocity of electrons in some kinds of gases as a function of the drift field at standard conditions [45].

These secondary electrons also ionize gas molecules, and the number of electrons increases exponentially. This process is called the electron avalanche multiplication. The number of generated electron-ion pairs per unit length is expressed by the first Townsend coefficient α, which is correspond to the inverse of the mean free path of electrons. The total number of electrons is

$$n = n_0 \exp \alpha x \tag{A.5}$$

where, n_0 is the number of primary electrons, and x is the path length of electrons. The value of α depends on the strength of the electric field, and the electric field depends on the position of electrons. Therefore, α also depends on the position of electrons. Hence, the multiplication factor M becomes

$$M = \frac{n}{n_0} = \exp \int \alpha dx \tag{A.6}$$

When the total charge generated by the avalanche process reaches some value, the avalanche turns into sparks. Sparks cause a critical breakdown and a dead time. In order to prevent sparks, it is important to know this limit. This limit is known as the Raether limit [8] and that is

$$M \sim 10^8 \tag{A.7}$$

Appendix B

Performance estimation for the ATLAS Muon Tagger

B.1 ATLAS Muon Tagger

The performance of the μ-PIC in the high-rate environment has been estimated from spark measurements with fast neutrons. As a model of the high-rate environment, we choose the large eta muon tagger for ATLAS, which is proposed to be installed during the phase-2 luminosity upgrade of the LHC in 2023 [46,47]. Figure B.1 (left) shows the layout of the cross section of the ATLAS detector. It shows only the inner region of 1st and 4th quadrants. The muon tagger is placed at 7m away from the interaction point and 25-90cm away from the beam axis. Figure B.1 (right) shows the schematic drawing of the hit rate on the muon tagger. It is estimated to be 9MHz/cm^2 at the innermost region and 600kHz/cm^2 at the outermost region. For the precise track identification with a good rejection of fake tags, 500μm granularity and few mm^{2}m position resolution with 5 detector planes are required.

B.1.1 Radiation environment at the Muon Tagger

The radiation environment was estimated by the FLUGG simulation [48]. The simulated data has 10000 proton-proton (p-p) interactions events with taking account of 200 p-p interactions in each 25ns, that is expected in the HL-LHC at ATLAS. Figure B.2 shows the rate of particles per cm^2 per p-p interaction as a function of the radial position. Neutrons are the most dominant particles at the radial position more than $\sim$30cm. Photons become most dominant at the radial position less than $\sim$30cm. In this thesis, the performance of the μ-PIC is estimated only with respect to fast neutrons. Figure B.3 shows the simulated histogram of the neutron energy in the Muon Tagger region. Assuming that the energy of fast neutrons is more than 1MeV, the rate of fast neutrons is $\sim$7.2% in the whole neutrons event. Figure B.4 shows the flux of fast neutrons as a function of the radial position and it is between $0.4 - 20$MHz/cm^2.

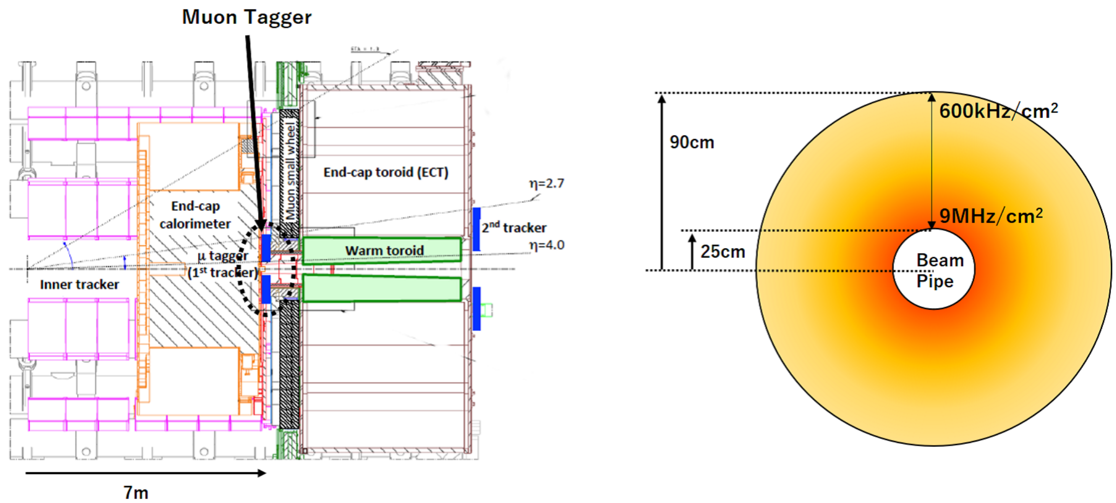

Figure B.1: Left: Layout of the cross section of the ATLAS detector. It shows only the inner region of 1st and 4th quadrants. The muon tagger is placed at 7m away from the interaction point and 25-90cm away from the center of the beam pipe [46]. Right: Schematic drawing of the hit rate. It is estimated to be 9MHz/cm^2 at the innermost region and 600kHz/cm^2 at the outermost region.

B.1.2 Performance estimation

Assuming that the gain is 5000 and the cathode resistivity is 180kΩ/sq., the performance of the μ-PIC in the Muon Tagger region has been estimated. First, we discuss about the gain reduction on the resistive electrodes. From the result of section 6.2.2, it can be seen that there is no sign of the gain drop under the fast neutron flux of $60 - 250$kHz/cm^2. However, under $1 - 4$MHz/cm^2 irradiation, the gain decreased at that of more than 5000. Compared to FigB.4, the μ-PIC is expected to be operated without any gain drop at the radial position of more than 70cm. However, it is expected that the gain will be dropped at the radial position of at least less than 45cm. In order to operate the μ-PIC at inner position, the cathode resistivity should be reduced to several tens of kΩ/sq.

Next, we discuss about the spark rate. Assuming that an event where a HV current of more than 1μA flows is defined as a spark, the spark rate at the gain of $\sim$5000 is almost 10^{-8} per one neutron. From the result of section 6.2.3, it can be seen that the effect of the spark depends on the size of the μ-PIC. Figure B.5 shows the difference of the response to a spark depending on the detector size assuming that a front-end chip has 128 readouts. When 10cm $\times$ 10cm region is covered by one detector, at least 3/4 areas become unavailable by a spark. When the same region is covered by four detectors of 5cm $\times$ 5cm, only 1/4 area becomes unavailable by a spark. Therefore, the spark rate is estimated assuming that the detector size is 5cm $\times$ 5cm. Figure B.6 shows the spark rate per 5cm $\times$ 5cm detection area in the muon tagger region. A spark is occurred per several seconds at the radial position of more than 45cm, and per below 1 second at the radial position of less than 45cm. For a good reduction of fake signals, at least 5 detector planes are required for the

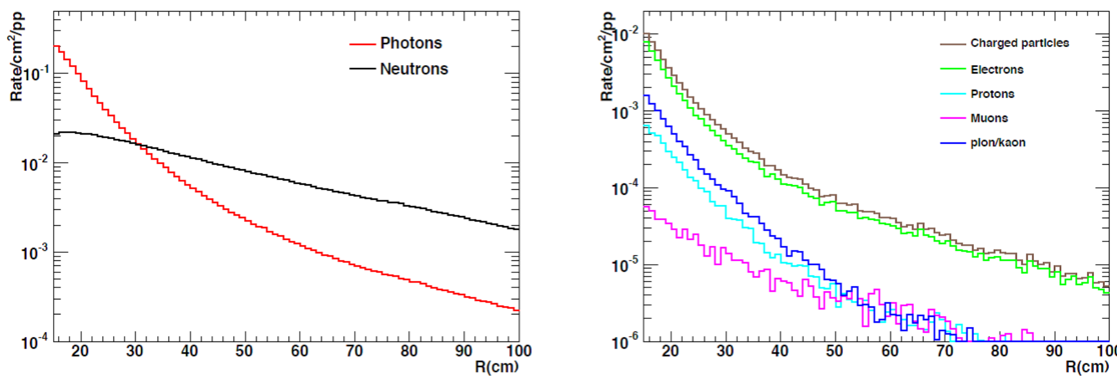

Figure B.2: Rate of particles per cm^2 per p-p interaction as a function of the radial position. Left: Photons and neutrons. Right: Charged particles [46].

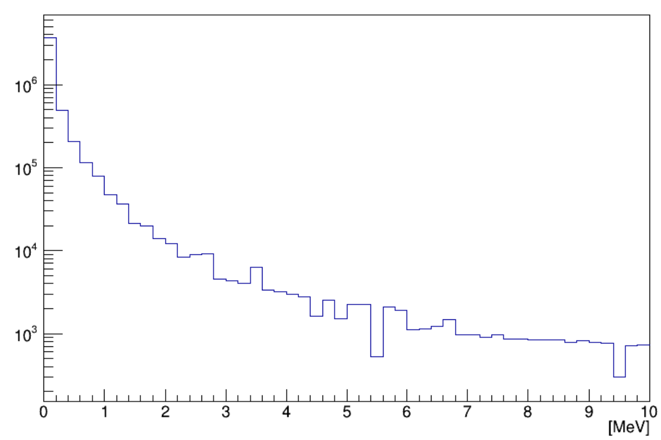

Figure B.3: Histogram of the neutron energy. Assuming that the energy of fast neutrons is more than 1MeV, the rate of fast neutrons is ~7.2%.

Muon Tagger. Using the result of the duration time of a spark (see section 6.2.3), the detection efficiency of the μ-PIC with 5 planes has been estimated. Figure B.7 shows the detection efficiency as a function of the radial position for single plane (red) and 5 planes (blue) assuming that the duration time of a spark is 30ms. Efficiency of more than 90% can be achieved in most areas if only single plane. However, it becomes below 80% at the radial position of less than 50cm if 5 planes are required. In the most inner region, a good efficiency cannot be expected.

From the result of the gain drop, the cathode resistivity should be reduced for operating in the inner region. On the other hand, from the result of the spark rate, the spark rate should be reduced for operating in the inner region. This is expected to be realized by letting the resistive cathode have higher resistivity. These requirements conflict with each other. Hence, it seems reasonable to operate the μ-PIC at the outer region of 50-90cm or 60-90cm, where 75% or 60% of the Muon Tagger can be covered by the μ-PIC. In this condition, the μ-PIC is expected to

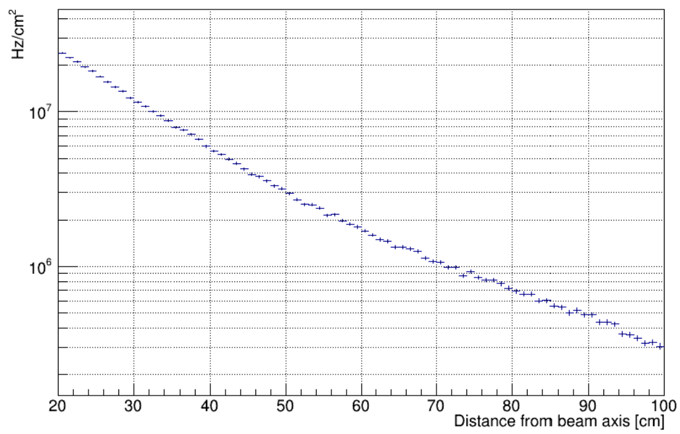

Figure B.4: Flux of fast neutrons as a function of the radial position, in which their energy is assumed to be more than 1MeV.

realize the particle identification with a good resolution and with a good efficiency.

This result has been estimated assuming only fast neutrons. Most neutron backgrounds are thermal and slow neutrons, therefore it is also important to evaluate the performance about them. Also, it is worth testing the μ-PIC with low resistivity of several tens of kΩ/sq. If the μ-PIC can withstand in the harsh radiation background with lower resistivity, there is a possibility to extend the operational area to the inner region.

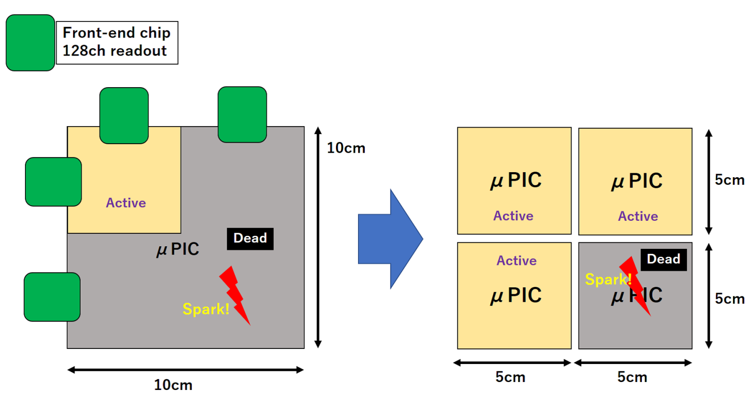

Figure B.5: Difference of the response to a spark depending on the detector size. When 10cm $\times$ 10cm region is covered by one detector, at least 3/4 areas become unavailable by a spark. When the same region is covered by four detectors of 5cm $\times$ 5cm, only 1/4 area becomes unavailable by a spark.

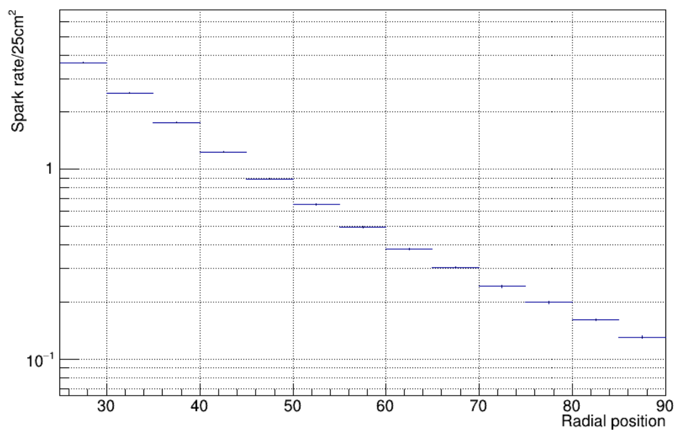

Figure B.6: Flux of fast neutrons as a function of the radial position, in which their energy is assumed to be more than 1MeV.

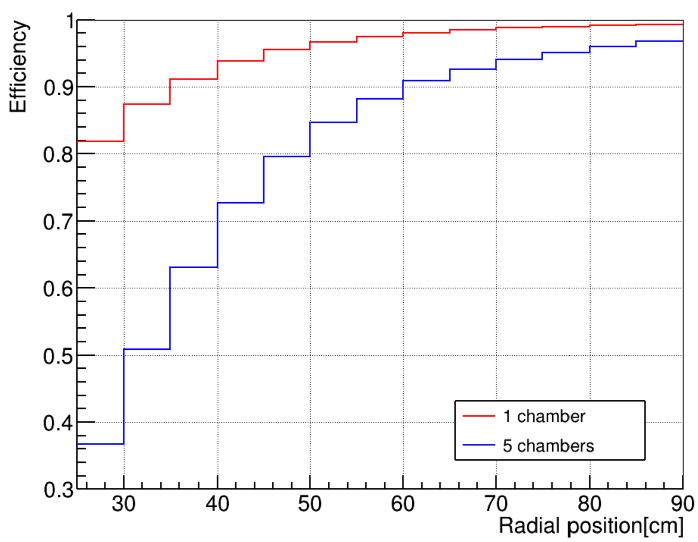

Figure B.7: Detection efficiency as a function of the radial position for single plane (red) and 5 planes (blue) assuming that the duration time of a spark is 30ms.

References

[1] Rossi, L. and Br 端 ning, O., High Luminosity Large Hadron Collider A description for the European Strategy Preparatory Group, Tech. Rep. CERN-ATS-2012-236, CERN, Geneva, Aug, 2012.

[2] M. Titov, Perspectives of Micro-Pattern Gaseous Detector Technologies for Future Physics Projects. arXiv:1308.3047 (2013).

[3] Y. Giomataris et al., MICROMEGAS: a high-granularity position-sensitive gaseous detector for high particle-flux environments. Nucl. Instr. Meth. A376 (1996) 29.

[4] ATLAS Collaboration: ATLAS New Small Wheel Technical Design Report

[5] F. Sauli, GEM: A new concept for electron amplification in gas detectors. Nucl. Instr. Meth. A386 (1997) 531.

[6] F. Sauli, The gas electron multiplier (GEM): Operating principles and applications. Nucl. Instrum. Meth. A805 (2016) 2.

[7] A. Colaleo, A. Safonov, A. Sharma and M. Tytgat, 2015 CMS technical design report for the muon endcap GEM upgrade, CERN-LHCC-2015-012

[8] H.Raether,"Electron avalanches and breakdown in gases,"Butterworths (1964)

[9] V. Peskov, P. Fonte, Research on discharges in micropattern and small gap gaseous detectors. arXiv:0911.0463 (2009)

[10] R. Oliveira, et al., Further developments and tests of microstrip gas counters with resistive electrodes. arXiv:1101.3727 (2011)

[11] T. Alexopoulos et al., A spark-resistant bulk-micromegas chamber for high-rate applications, Nucl. Instrum. Meth. A 640 (2011) 110.

[12] A. Ochi, et al., A new design of gaseous imaging detector Micro Pixel Chamber. Nucl. Instr. Meth. A 471 (2001) 264.

[13] A. Ochi, et al., Development of micro pixel chamber. Nucl. Instr. Meth. A 478 (2002) 196.

[14] A. Ochi et al., Micro Pixel Chamber with resistive electrodes for spark reduction. JINST 9 C01039, 1 (2014)

[15] A. Ochi et al., Carbon Sputtering Technology for MPGD detectors. PoS(TIPP2014)351

[16] G. Charpak et al., THE USE OF MULTIWIRE PROPORTIONAL COUNTERS TO SELECT AND LOCALIZE CHARGED PARTICLES. Nucl. Instr. Meth. 62 (1968) 262.

[17] Nobelprize.org https://www.nobelprize.org/nobel_prizes/physics/laureates/1992/press.html

[18] A. Oed, Position-sensitive detector with microstrip anode for electron multiplication with gases, Nucl. Instr. Meth. A 263 (1988) 351.

[19] A. Ochi, Ph.D thesis, Tokyo Institute of technology, 1998.

[20] F.Sauli, A.Sharma, MICROPATTERN GASEOUS DETECTORS, Annual Review of Nuclear and Particle Science 49 (1999) 341.

[21] B. Ketzer, S. Bachmann, M. Cape 呷 ns, M. Deutel, J. Friedrich, S. Kappler, I. Konorov, S. Paul, A. Placci, K. Reisinger, L. Ropelewski, L. Shekhtman, F. Sauli, "GEM detectors for COMPASS", IEEE Trans. Nucl. Sci., vol.48 (2001) 1065.

[22] D. Thers et al., Micromegas as a large microstrip detector for the COMPASS experiment. Nucl. Instr. Meth. A 469 (2001) 133

[23] A. Rubin et al., First studies with the Resistive-Plate WELL gaseous multiplier. JINST 8 P11004 (2013)

[24] M. Alviggi et al., Small-pads resistive micromegas. JINST 12 C03077 (2017)

[25] M. Bianco et al., Micromegas detectors for the muon spectrometer upgrade of the ATLAS experiment. Nucl. Instr. Meth. A 824 (2016) 496

[26] S. Yamauchi, Master thesis. Kobe university. 2016

[27] F. Yamane et al., Development of μ-PIC with resistive electrodes using sputtered carbon. EPJ Web of Conferences 174, 04001 (2018) MPGD2015

[28] F. Yamane et al., A new design of the Micro Pixel Chamber using DLC electrodes. 5th International Conference on Micro Pattern Gaseous Detectors

[29] T. Tanimori et al., AN ELECTRON-TRACKING COMPTON TELESCOPE FOR A SURVEY OF THE DEEP UNIVERSE BY MeV GAMMA-RAYS. The Astrophysical Journal 810 (2015) 28

[30] K. Nakamura et al., Direction-sensitive dark matter search with gaseous tracking detector NEWAGE. PTEP 043F01, (2015)

[31] J. D. Parker et al., Neutron imaging detector based on the μPIC micro-pixel chamber. NIM A 497 (2013) 23

[32] Y. Kishimoto et al., Basic performance of a position-sensitive tissue-equivalent proportional chamber (PS-TEPC). NIM A 732 (2013) 591

[33] A. Ochi et al., Development of Micro Pixel Chamber for ATLAS upgrade. Physics Procedia 37 (2012) 554

[34] M. Raymond and G. Hall CMS microstrip tracker readout at the SLHC, paper presented at Topical Workshop on Electronics for Particle Physics (TWEPP 2008), Naxos Greece, 15 September 2008.

[35] ATLAS TGC collaboration, Amplifier-Shaper- Discriminator ICs and ASD Boards (Production Readiness Review Report, 1999)

[36] https://espace.cern.ch/hiradmat-sps

[37] http://sba.web.cern.ch/sba/BeamsAndAreas/h4/H4manual.htm

[38] M. Byszewski and J. Wotschack, Resistive-strips micromegas detectors with two-dimensional readout. JINST 7 C02060 (2012)

[39] Hans Muller, "SRS Readout architectures", https://indico.cern.ch/event/236266/contributions/507853/attachments/395969/550721/ Summary on SRS readout systems of RD51draft.pdf

[40] M.Iodice et al., JINST 9 C01017

[41] https://twiki.cern.ch/twiki/bin/view/AtlasPublic/NSWPublicResults

[42] Y.Zuo et al., Neutron yields of thick Be target bombarded with low energy deuterons. Physics Procedia 60 (2014) 220

[43] Particle Data Group Collaboration, K. A. Olive et al. , "Review of Particle Physics," Chin. Phys.C38 (2014) 090001.

[44] E. McDaniel and E. Mason,"The Mobility and Diffusion of Ions in Gases"(Wiley, 1973)

[45] S.C.Brown,"Basic Data of Plasma Physics,"MIT Press, Cambridge,MA(1959)

[46] M.Aleksa et all,"ATLAS NOTE : Large Eta Task Force Report,"ATL-UPGRADE-INT-2015-001

[47] ATLAS Collaboration: Muon Spectrometer Phase-II Upgrade Technical Design Report (to be published)

[48] http://www.fluka.org/content/tools/flugg/index.html